Contrast Patterns for Optimizing Brilliance in Colored Gemstone Faceting

Fluorescence Produced by Common Optical Defects in Diamond

Quick Reference Chart for Optical Defects in Diamond

Nephrite Jade from the Italian Alps

About the Cover

The lead article in this issue examines the visual contrast patterns that optimize brightness in faceted gemstones. Brightness is superbly demonstrated by the gemstones shown on the cover, part of a collection of more than 100 trilliant-cut stones on display at GIA Carlsbad. Clockwise from the top: 61.98 ct kunzite, 48.31 ct sphalerite, 9.67 ct grossular garnet, 7.71 ct zircon, 12.27 ct sphalerite, and 29.59 ct spessartine. Center: 25.15 ct fluorite. Collection courtesy of Roz and Gene Meieran; photo by Robert Weldon.

FSC
www.fsc.org
MIX
Paper from responsible sources
FSC® C006300

INTEGRATING *G&G* with
GIA's Gemology Education

One of the things I've always wanted to do is create synergy between GIA's gemology courses and *Gems & Gemology*. Many of the student assignments incorporate research from the journal, and adding *G&G* articles as references would provide support and validation for the information in our coursework.

As we added video media to our eLearning courses, we featured interviews with many of GIA's research scientists, some of whom were also *G&G* authors. Providing their articles to our students was a natural next step.

In the past, I had discussed this idea with Alice Keller when she was editor-in-chief of *G&G*. Although everyone was willing, we had no practical way to achieve it at the time. Now that every issue is available free of charge on the redesigned GIA website at www.gia.edu, we can realize this ambition.

Beginning with our *Diamonds & Diamond Grading* eLearning course, we'll provide links at the end of every assignment to specially chosen *G&G* feature articles.

Besides illuminating some of the source material for our coursework, links to supporting articles will provide a truly meaningful pathway into the resources on our new website. Students with inquiring minds will find many avenues of interest.

Besides illuminating some of the source material for our coursework, links to supporting G&G *articles will provide a truly meaningful pathway into the resources on our new website.*

For example, I believe a good number of students would choose to explore the important *G&G* articles on colored diamond, diamond treatment, or diamond synthesis. Others might also download articles focused on mining, production, and the diamond supply chain, or read about the many famous gems examined or graded by GIA's laboratory.

This tie-in exposes the tremendous amount of important work that *G&G* authors—both internal and external to GIA—have done to enrich our collective knowledge on the many aspects of diamond, and makes it available to a wider, and younger, audience.

We'll also provide a short student study guide that explains the structure of a typical feature article and explains how to navigate one.

In time, we'll add similar links to relevant *G&G* articles in our other gemology courses.

Let me take this opportunity to thank all our current *G&G* print subscribers and online users. I hope to welcome many more of you in the near future.

Duncan Pay | Editor-in-Chief | dpay@gia.edu

Optimizing Face-Up Appearance in Colored Gemstone Faceting

Al Gilbertson

The human visual system interprets visual cues to perceive different intensities of brightness. Patterns of light and dark contrast create impressions of brightness in faceted gemstones. These patterns generally remain coherent in the viewer's eye when the gemstone is tilted or rotated. Using computer-generated color-coded contrast maps in facet planning can improve apparent brightness, optimizing a gemstone's appearance.

There are many challenges in choosing a facet arrangement that optimizes a colored stone's face-up appearance. What contributes to an attractive appearance? In the field of cognitive science, experts have identified rules that govern our perception of visual cues such as line, color, form, brightness, contrast, and motion. The subconscious processing of these cues is the work of each person's "visual intelligence system," wherein every aspect of our visual experience is framed. In gemstones, brightness depends on how we process visual cues, so some patterns appear brighter than others even when the measurable light return is identical. Studying these rules can help formulate design strategies to make gemstones brighter and more interesting. Tools exist for exploring these aspects of appearance. Using these, cutters can choose elements that will optimize the design. Effective design requires an exploration of the best angle combinations and placement of facets for a given material. Nevertheless, *choices about appearance are personal*. And while preferences vary, this study assumes the goal of improving scintillation while maintaining as much brightness as possible. Most colored stone cutters understand their own preferences regarding visual contrast, depth of color, spread (shallow or deep), brightness, and scintillation. By understanding certain aspects of optimization, they can modify designs to suit their own preferences. Ultimately, this will lead to a faceted gemstone with maximum appeal given the constraints of the material at hand. This paper focuses on gems with colors that are not easily weakened by pronounced brightness or darkness, similar to the medium range of tone and strong saturation found in peridot (figure 1).

UNDERSTANDING BRIGHTNESS AND CONTRAST

Understanding what creates the impression of brightness can help us map and plan areas in a gemstone to enhance observed brightness.

Cognitive scientists understand much of the complexity of the stimuli processed by our visual system. For example, even though variations in lighting result in varying wavelengths of light reflected from a colored surface, our visual intelligence system actually works as a subconscious processor, assigning a constant hue, saturation, and tone (which scientists refer to as "lightness"). This collaboration between the visual system and the brain is constantly extracting information from a flood of sensations to construct a visual world. In the words of leading cognitive scientist Donald Hoffman (1998), "You are a creative genius. Your creative genius is so accomplished that it appears, to you and others, as effortless. Yet, it far outstrips the most valiant efforts of today's fastest supercomputers. To invoke it, you need only open your eyes."

These scientists work primarily with two-dimensional printed (opaque) images or flat images on a computer monitor, and they consider brightness a subjective attribute or property of an object being

Figure 1. The concepts dealing with brightness, scintillation, and overall appearance are best evaluated in a gem whose color is not easily weakened by making it bright or overly dark, such as peridot. Photo by Robert Weldon, © GIA.

observed. Gemstones are three-dimensional and transparent, and the light reflected from within them has a greater impact on their face-up appearance than the light reflected from the surface. Our visual intelligence processes visual cues so we see a gem that seems to generate light from within itself, in a pattern that changes as the gem moves. This pattern is generated by the interaction of light with the faceting design.

Jose Sasián, a professor of optical sciences at the University of Arizona, explains that while looking at a gem, the observer appears to see more facets than actually exist. Sasián (2007) calls these "virtual" facets. These perceived facets are a result of different levels of contrast, caused by light striking all the facets and then splitting, creating the appearance of many more facets.

How we interpret visual cues is critical to understanding what creates a gemstone's beauty, and by studying these cues we can identify the elements to include in gem design.

The following is a general overview of the visual cues relevant to faceted, transparent gems.

Invisible Surfaces. Termed by some vision scientists as "the invisible surface that glows," the illustration created by G. Kanizsa (1955) shows two different triangles that are more luminous (i.e., brighter) than the background, and whose borders are easily observed even though there are no lines defining them (figure 2). Using a photometer, one cannot detect any edges of the triangle. The borders and luminosity are purely the construction of the observer's visual intelligence system. The brain uses a variety of cues to construct these images, which we will refer to as "invisible surface maps." In figure 3, the invisible surface map on the left has a more luminous square area than the map on the right. How the brain perceives the lines that resemble small "check marks" causes this duller effect.

In the three "plus-symbol" outlines in figure 4, the first contains a square luminous area in the center. In the second image, the sides of the square bow inward

Figure 2. Observers see a bright, luminous triangle in the center of both figures, even though there are no defining lines. Cognitive scientists attribute this "invisible surface map" to how our brain interprets visual cues provided by the contrast of light and dark. From Kanizsa (1955).

Figure 3. The visual contrast cues in this pair of invisible surface maps are different, causing our brain to interpret the left square as brighter than the right square. From Albert (1955).
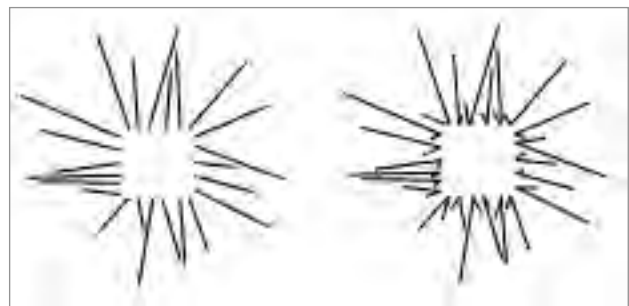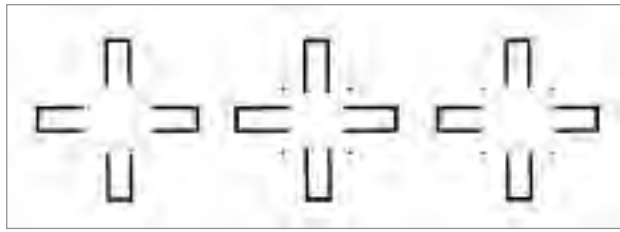
Figure 4. These "plus-symbol" outlines have slightly different visual cues. The first contains a square bright middle area. In the second, the square appears to have concave sides due to the four dots. With the third, the bowing has been removed by shifting the four sets of lines. From Petry (1987).

due to the addition of visual cues (the four black dots). In the third image, the bowing disappears because the four sets of lines have been shortened to square up with the black dots. (Note: The brain can interpret visual cues in more than one way. For example, some see a circular rather than a square luminous area in the leftmost image.)

Varying combinations of bright and dark can cause the observer to perceive different intensities of brightness. This does not address personal preferences for different combinations. For example, the invisible surface maps in figures 5A–5G demonstrate various visual cues that create a bright circular area in the center. In each of these examples, the different cues and their arrangements result in varying degrees of perceived brightness, leading to the impression of an edge that is not really there—the invisible surface. Different types of pattern elements (such as blunt lines, dots, or wedges) can produce similar appearances, depending on how they are arranged. Elements of varying brightness can also be embedded or stacked within each other (figures 5H–5J), creating multiple bright areas. Shifting the center of these embedded areas (figure 5I) does not disturb the impressions of brightness; the center has moved along with the areas of contrast. Although these areas show strong contrast, they are still coherent and bright, much like when a faceted gemstone is rocked. They are also present in non-round shapes such as the marquise or oval, as shown in figure 5J.

The ability to see these illusory bright areas in an invisible surface map is enhanced by movement. When the image in figure 6 was "flickered" rapidly on a computer monitor, the illusory center became brighter. When the flickering image was also rotated, the apparent brightness increased significantly. The flashing of light and dark patterns caused by rotating and flickering the image equates to the scintillation seen when we move a gemstone back and forth. Stronger contrast (black or gray areas against white backgrounds) also equates to stronger scintillation. Vision scientists have found that in certain cases an image stays organized or coherent in a viewer's mind when the direction of observation is changed, as through movement.

Figure 5. These invisible surface maps have slightly different contrast cues, resulting in the impression of bright or luminous circles (A–G). Contrast cues can also be stacked or embedded within each other (H–J) to give the impression of multiple areas of brightness.
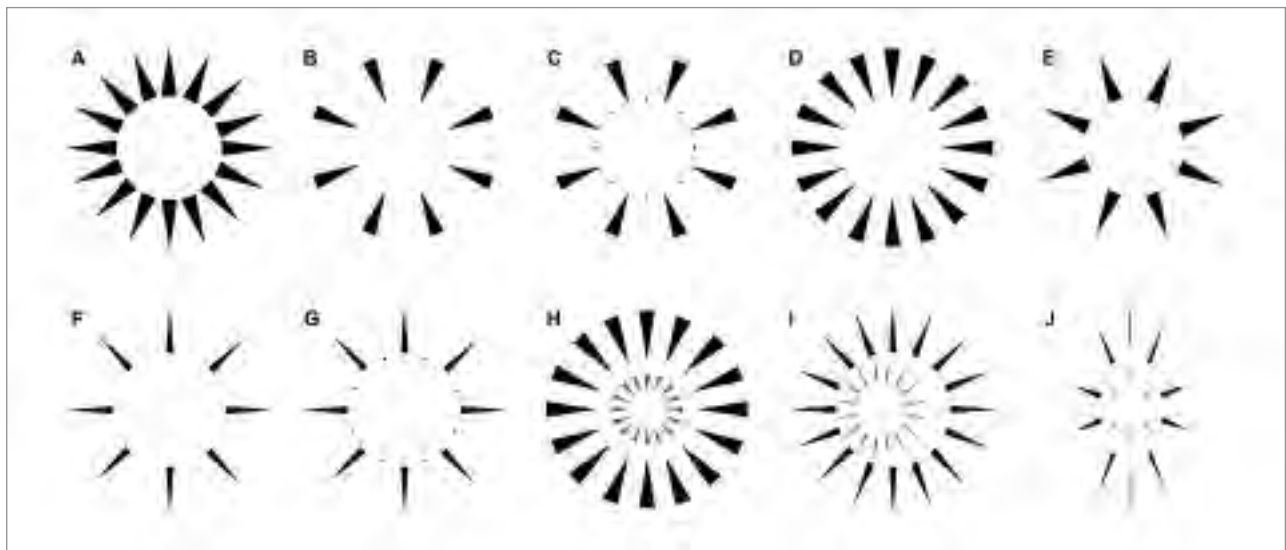
Brightness Contrast. Appraiser Michael Cowing, FGA, has published several articles on evaluating diamond cut quality, coining the term "brilliance contrast" to describe how contrast causes the brightness observed in diamonds (2009). Each of the circles in figure 7 is 50% dark and 50% light by surface area. A light meter confirms that each one is equally bright when printed on paper (even the gray ones). The checkered pattern of the bottom left circle makes it perhaps the most visually interesting. If a gem were able to return 100% of the light (all white), and no dark areas were visible, it would measure

Figure 7. Each of these circles is 50% dark and 50% light by surface area. Yet the circles on the right are dull due to weak contrast. A gemstone's visual interest depends on good contrast. If it returned all light and had no contrast, the gemstone would be uninteresting.

In Brief

- A gem's brightness and attractiveness depends not only on how much light is returned but also on the contrast pattern or contrast distribution created by virtual facets.
- An idealized contrast plot shows the types of contrast distribution that contribute to effective gem designs to be used by faceters.
- Following rules for optimization, such as creating a design with the right contrast distribution, improves a gem's appearance and increases its fire.

brighter than a stone with dark areas of contrast—but its appearance would be far less appealing. For instance, the right column in figure 7 seems duller than the left due to weaker contrast. These images show that while good light return is an important aspect of "brilliance," contrast is a critical factor in face-up brightness. Obviously, there comes a point when too much darkness or a poor distribution of darkness is less pleasing.

Figure 6. Observers see a markedly increased brightness in the center circle when this invisible surface map is flickered on a computer monitor. When the image is rotated and flickered simultaneously, the brightness further increases. From Petry (1987).

Figure 8 shows a common optical illusion known as "White's Illusion." Although the rectangles in B seem darker than those in A, they are actually of equal luminance. In fact, they have the same gray color. The gray areas embedded in dark stripes (A) appear brighter than the gray areas embedded in white stripes (B). This illustrates the concept of "lateral inhibition," in which the perceived brightness of an area depends upon its surroundings (White, 1979).

Figure 8. The rectangles on the right appear darker than those on the left, but they are actually the same shade of gray. This demonstrates that the perceived brightness of an area depends on the surroundings and the contrast. From White (1979).
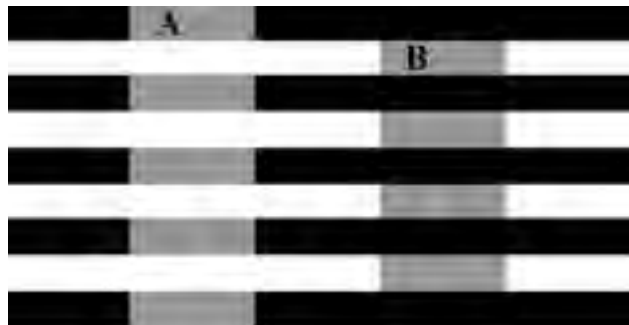
In figure 9, the horizontal stripe and all six boxes have the same brightness and color, but the squares' apparent brightness depends on the contrast of the surrounding area. In this illusion demonstrating "simultaneous lightness contrast" (an example of lateral inhibition), apparent lightness is different from quantitative lightness, the real measurement of the total lightness reflected from an object. The phenomenon also occurs when a colored area is placed on a dark background, making it appear clearer, brighter, or more luminous. In figure 10, for example, the navette shapes at the bottom are identical, but they appear to be different colors when placed on alternating light and dark backgrounds (C). The difference is accentuated with the addition of an interwoven background (A and B).

Summary of Vision Science. Combining the ideas of invisible surfaces and brightness contrast, we can derive that darker contrast, placed in the right locations, can give faceted gems a brighter appearance. The areas of contrast need to be evenly distributed and not grouped together; this is particularly true for areas under the table. Our eye tends to gravitate toward the center to gather an overall impression of brightness. The diagrams in figure 11 illustrate how the placement of dark areas affects brightness. The patterns are identical but contain varying levels of contrast. The image of highest contrast (bottom right, for most observers) also has the brightest-looking center. This is a common goal in facet design, as dark centers, or "nail heads," are undesirable in the jewelry trade.

From cognitive science we know that the apparent brightness of an invisible surface of definable

Figure 10. The navette shapes throughout this image have the same tone but appear darker or lighter depending on the adjacent areas. From Sarcone and Waeber (undated).

shape results from certain visual cues relating to differences of light and dark. The effect is further enhanced by movement, and invisible surfaces can be stacked or embedded within each other. Strong contrast makes a gemstone appear brighter and more appealing, and the position of the contrast is also

Figure 11. Varying the levels of contrast affects the appearance of brightness. Each circle has the same pattern, but the areas of contrast vary in strength. The circle with the highest contrast (bottom right) has the brightest-looking center.

Figure 9. The stripe and the small squares are all the same shade of gray, again illustrating that perceived brightness relies upon its surroundings and the contrast, which changes as the environment changes. From Purves (2011).
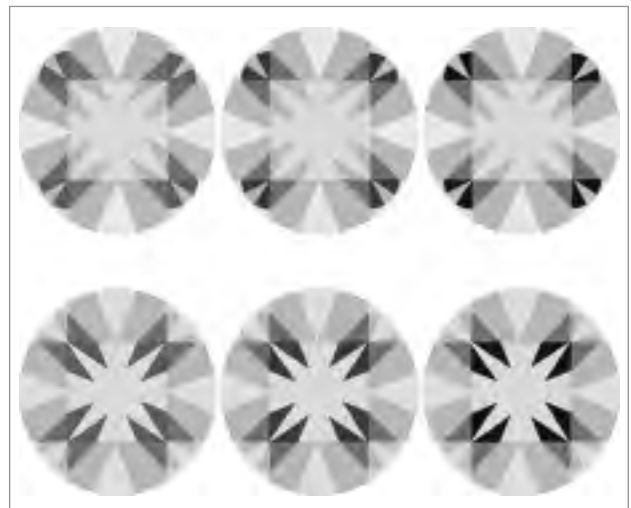
important. Scintillation is more dynamic when there is strong contrast between adjacent virtual facets.

If we understand what causes the cues for brightness in any shape, we can use this information to design effective facet patterns by using strong contrast and ending the lines of contrast to produce a bright center. A gem's brightness and attractiveness depends not only on how much light is returned—angles are still important—but also on the contrast pattern created by virtual facets. Once an effective pattern is established, the major elements of that pattern must remain in effect when the gem is tilted to maintain the appearance of brightness. This means that the pavilion angles cannot be cut near an angle that allows the gem to "window," letting light leak through. If the slightest tilt interrupts the pattern due to a window, the pattern is not effective because the contrast pattern has been eliminated. The impact of these effects may vary according to the level of brightness, as dictated by refractive index and color saturation.

TOOLS FOR ASSESSING CONTRAST

If contrast is an important part of faceting various gem materials, there needs to be a reliable method to determine elements of contrast. Most critical is the contrast caused by the reflection of the observer's head and torso. Harding (1975) first identified this critical element: the effect of an observer's head blocking rays of overhead illumination. He calculated the rays returned from the gem to the viewer's eyes, as well as the illumination blocked by the viewer's head.

Regarding head obstruction, Harding writes, "For ultimate liveliness it should be possible to see reflections in the table from both sides of the pavilion with both eyes at once. At a viewing distance of one foot, as shown in [figure 12], the angle between reflections to both eyes (two different rays) is about 12°. To see reflections from both sides with both eyes, therefore, the minimum external table reflection angle must be at least 6°." While not directly discussing the need for contrast, Harding alluded to its importance. Of course, liveliness stems from scintillation, the result of strong contrast between neighboring facets when the gem, the light source, or the observer moves.

This concept was also part of Kazumi Okuda's groundbreaking work in about 1980. His experiments with reflectors—"hearts and arrows" viewers have evolved from these devices—led to the FireScope™ introduced by JDM in Japan. JDM used the black reflection of the lens as a dark contrast against a red reflecting field (figure 13). Studying the black reflection, they determined the importance of certain reflection
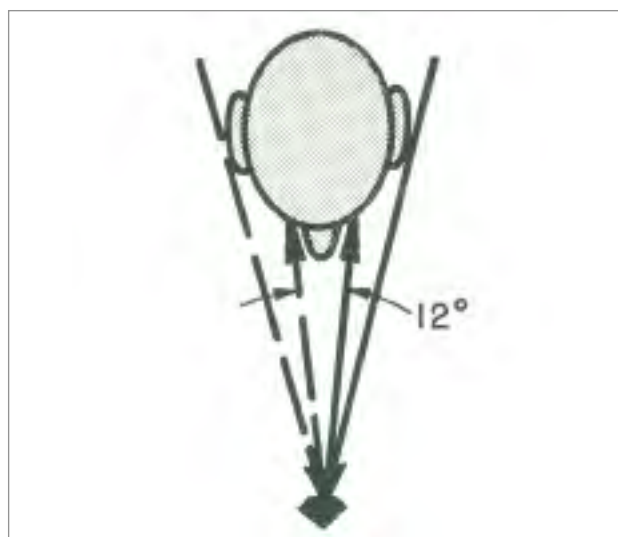
Figure 12. A gemstone's liveliness is the result of scintillation: the strong contrast between neighboring facets when the gem, the light source, or the observer moves. An observer's head (shown from above) obstructs overhead light, causing a sharp change in the light streaming into the gem. Note that at a viewing distance of one foot (approximately 30 cm), the angle between the two reflected rays that return to both eyes is about 12°. From Harding (1975, figure 8).

patterns in diamond appearance, as shown in an undated FireScope brochure, circa 1987.

It should be noted that an observer both blocks light from the rear and reflects light from the front or side. In most environments, however, far less light

Figure 13. The FireScope by JDM uses the black reflection of the viewing lens as a dark contrast against a red reflecting field. Studying the patterns of different diamonds, JDM concluded that the most attractive diamonds have a certain contrast pattern. From an undated FireScope brochure, circa 1987.
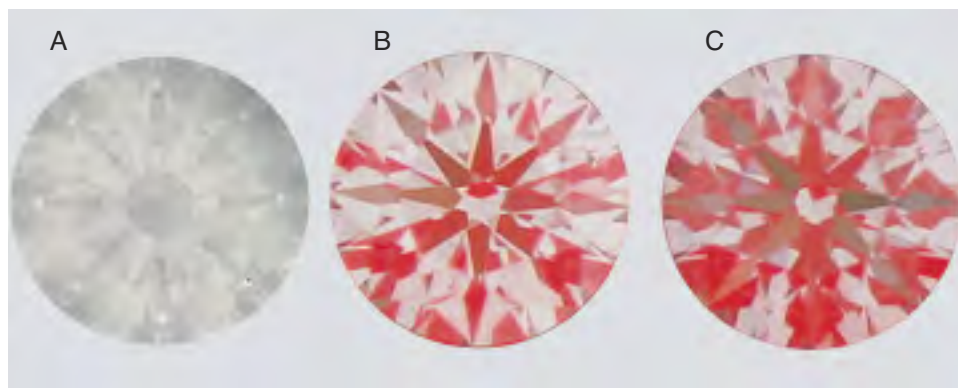
Figure 14. These photos show the same gemstone under different viewing conditions: (A) under totally diffused white light; (B) under the same environment, with the observer wearing a red mask and garment; and (C) with the observer standing closer. From these, it is apparent that the observer sees much of their own reflection, as dark contrast in the gemstone.

is reflected into the gem from the observer's head and shoulders than from around and above the observer. The observer's reflection therefore serves as the major source of contrast in the lighting environment.

To better understand this, consider what a faceted gem might look like in a totally diffuse white-lit environment (figure 14). If the gem reflected nothing but white light, it would have no contrast (A). If you were to cover your face and shoulders with a fluorescent red mask and view the gem in the same environment, you would see red contrast (B). If you moved closer to the gem, there would be even more red reflected throughout it (C).

In 1997, this author started experimenting with color coding of light (and contrast) entering a stone from various angles ("Reflector technologies," undated). By constructing a hemisphere or dome with concentric rings of color (figure 15) and viewing the stone through an aperture at the top of the dome, one can see that the gem gathers its light from the colored rings. DiamCalc, a 3D modeling program introduced in Russia in March 1999, uses ray tracing to alter the proportions and angles of a diamond image viewed on a computer monitor. By 2000, color-coded lighting environments were added, allowing the modification of angle of arc as well as color. DiamCalc can model virtual polished gemstones in a variety of realistic lighting environments, including GemCad's ISO and COS, Fire Scope™, Ideal-Scope, ASET (Angular Spectrum Evaluation Tool), and AG,

the author's own environment. GemCad is a popular computer-aided design (CAD) program used to create accurate 3D models of a faceted gemstone. DiamCalc accepts GemCad and other designs and allows changes in table size and girdle thickness, as well as facet angles and azimuths, for a variety of standard shapes. DiamCalc can also create motion pictures of a gem being rocked or otherwise moved from side to side in these lighting environments. The software is widely used in the diamond cutting industry to plan rough and design new cuts. It can accept files from GemCad (.asc format), Sarin (.srn), Helium (.mmd), and Autodesk (.dxf or .stl), as well as certain .txt files. It can generate the following file formats: Autodesk DXF (.dxf), GemCad (.asc), and binary and ASCII STL (both in .stl format). For colored stone cutters, it allows variations in refractive index for modeling various gem materials.

DiamCalc does not model double refraction, so the effects of a closed or dark c-axis cannot be predicted. Many stones are dichroic, which means one sees different colors in different directions through the gem. Some gems with this property will show nearly identical colors in all directions, while some will show only differences in color density (darker or lighter tone). For example, tourmaline often has extreme dichroism, and this characteristic is referred to by many gem cutters as a "closed c-axis" or "dark c-axis." In other words, light does not pass through one axis (direction) of the stone, or only passes in a limited amount.

Figure 15. Gemstones gather light from the surrounding viewing environment. When placed under a hemisphere lined with concentric rings of various colors (left and center), a gemstone (right) returns the colors of the dome.

Comparison of Two Important Models. While Diam-Calc supports a variety of lighting environments, this paper deals with two of particular value in design optimization: AG and ASET (figure 16). These are variations of the color coding of light entering a diamond from specific surrounding arcs, patented in 2000 (Gilbertson, 2003) and 2004 (Caudill et al. 2008), respectively. While either can be used as a primary environment for planning or as a secondary double check, the AG environment offers certain advantages as the primary. Comparing the three-color ASET and the five-color AG patterns for the same stone, observe how their angles of light orientation differ. Key information about both the observer (black, 83°–90°) and the lower angles of light entry likely producing a strong contrast (dark violet, 40°–55°) are not represented well in the ASET image. Three color-coded zones do not provide enough information, as certain patterns with strong contrast (black) can produce some of the visual cues leading to different preferences.

If a design is planned with AG and then checked with ASET, however, nuances and slight weaknesses in design can be captured and modified later. These examples represent diamond's RI and the sets of angles considered optimum for diamond appearance. Since individuals may prefer different patterns, which can vary depending on RI, it is advisable to determine personal preference before analyzing patterns with AG and ASET lighting.

DiamCalc also allows the background to be color-coded. A black background is the default setting for both the AG and ASET environments, but white is also available. Areas where light passes through the gem from the background ("windows"), are indicated as white in the contrast plot when using the white background.

PRACTICAL APPLICATION

Past work can be useful for further understanding the AG lighting environment. For example, both GIA and the American Gem Society have determined that the most appealing round brilliant-cut diamonds have a balance of contrast and brightness (GIA, 2006; Sasián, 2007). The contrast maps of a typical well-cut diamond are shown in figures 16 and 17 to illustrate the relative balance of the various color-coded light entry angle ranges. Much like the invisible surface map examples in figure 5, these color-coded contrast maps can explain the pattern seen in the cut gem with AG lighting (figure 17).

With the AG environment, note that there is very little black (83°–90°). The black areas representing the retro-reflection of the observer should be minimized

ASET (+ white)

Green = 0° (horizon) to 45°
Red = 45° to 75°
Blue = 75° to 90°

AG (+ white)

Light Blue = 0° (horizon) to 40°
Dark Violet = 40° to 55°
Green = 55° to 70°
Red = 70° to 83°
Black = 83° to 90°

| Blue 75°–90° | Red 45°–75° | Green 0° (horizon) to 45° |

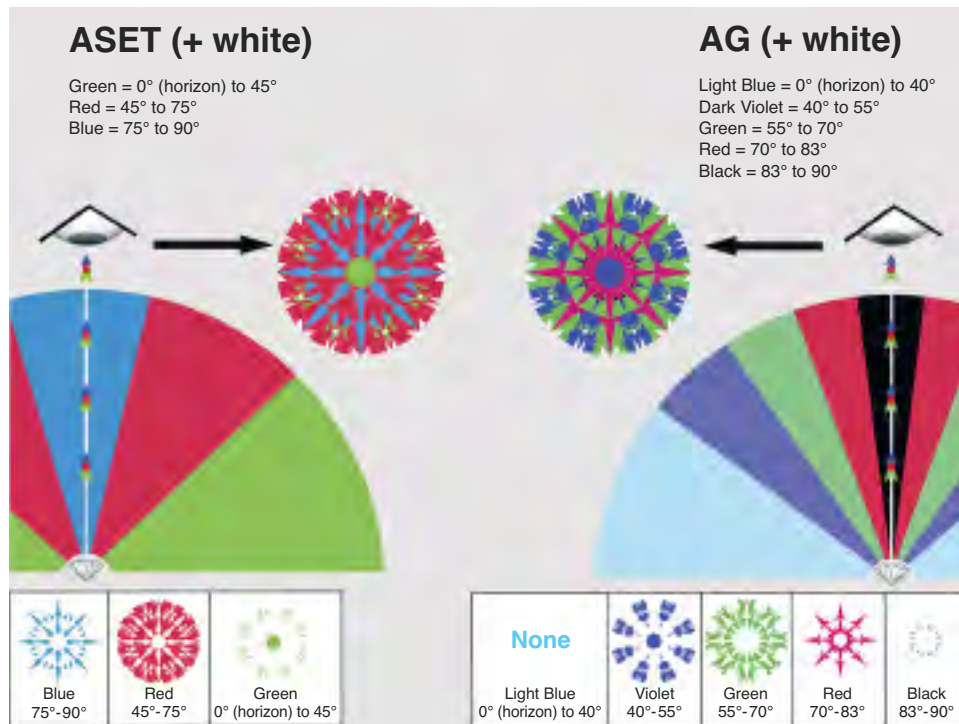| None | Light Blue 0° (horizon) to 40° | Violet 40°–55° | Green 55°–70° | Red 70°–83° | Black 83°–90° |

Figure 16. Two of the light color-coding models supported by Diamcalc—AG and ASET—can be used for mapping contrast in gemstone designs. Different aspects of contrast in the same gemstone can be seen using the three-color ASET environment and the five-color AG environment.

or removed in planning colored stones. The lowest angles of light entry represented by violet (40°–55°) will appear darker, along with any areas of windowing, which produces a very nice balance of varying contrasts within the gem. These examples are comparable to the dark areas in the invisible surface maps.

The contrast maps display a substantial amount of green, which is represented by light coming from around the observer's head (55°–70°). The red (70°–83°) is arranged in a narrow, wagon-wheel pattern from the girdle edge to the near-center. Red areas can appear dark or bright, depending on the observer's proximity to the gem or how much it is tilted. Both of these colors indicate the primary areas of brightness in a gem, comparable to the white area in the invisible surface maps. An effective design requires these areas of brightness to be prominent and well distributed, with the dark areas creating a balanced, contrasting pattern in the gem.

Contrast maps are similar to a much more complex stacked invisible surface set (such as figure 5H–J). As the invisible surface maps are moved and rotated, the apparent brightness increases dramatically and remains organized in a viewer's mind even when the direction of observation is changed. This means that movement (rotating and flickering) of the invisible surface maps is comparable to the scintillation seen when a gemstone moves back and forth. With the proper types of contrast in adjacent virtual facets of the red areas, the gem will be more interesting and attractive, and in many cases appear brighter. Note that while brightness may be the goal, too many areas of brightness can lighten the saturation of the color in large portions of the gem, lowering its market value.

EXAMPLES

Figure 18 shows examples of various gems purchased from the trade for GIA's Dr. Eduard J. Gübelin Collection. The individual gems were scanned using a non-contact measuring device to derive the facet angles and arrangement. A photo of each gem, showing the representative pattern viewed face-up, is accompanied by an AG contrast map derived from DiamCalc. The observer's face and torso are about 18–20 inches from the stone, and the photo captures a good representation of what the observer would typically see in the gem. The following is a brief discussion on the appearance of each gem.

Figure 18A: This native-cut golden sapphire (RI near 1.77) is particularly bright because the center of the gem reflects light gathered from around the observer and returns that light to the observer. Yet the outer areas window slightly, and in lighter colored gems this is distracting. This view can be explained by looking at the color-coded contrast map (AG with white contrast map). Red and green indicate higher-contrast areas that provide some brightness in those parts of the gem. Note that these extend out to the girdle, which is very important. The outer areas contain blue, resulting from lower-angle lighting. The outer white areas are the windows where the observer sees through the gem.

Figure 18B: When gently rocking this apatite (RI near 1.64), the observer sees much of their own dark reflection in the middle. The apparently bright outer edges in the photograph of the stone are actually dull; the observer sees through the gem. This produces a stone that is not very attractive or visually dynamic. The black area of the color-coded contrast map (AG

Figure 17. For this sample gemstone, there is little black (retro-reflection of the observer) in the AG environment. Red reflection (70°–83° arc) is arranged in a narrow, wagon-wheel pattern from the girdle edge to the near-center. Red will be bright when the gemstone is held at some distance, but dark if the gem is close to the observer. The evenly distributed green shows where light is returned from around the observer's head (55°–70° arc). Violet (40°–55° arc) comes from a low angle on the horizon and is generally dark. The lowest angles (0°–40° arc) would be seen as light blue. Together, these work to compose a uniformity of varying contrasts within the gem.
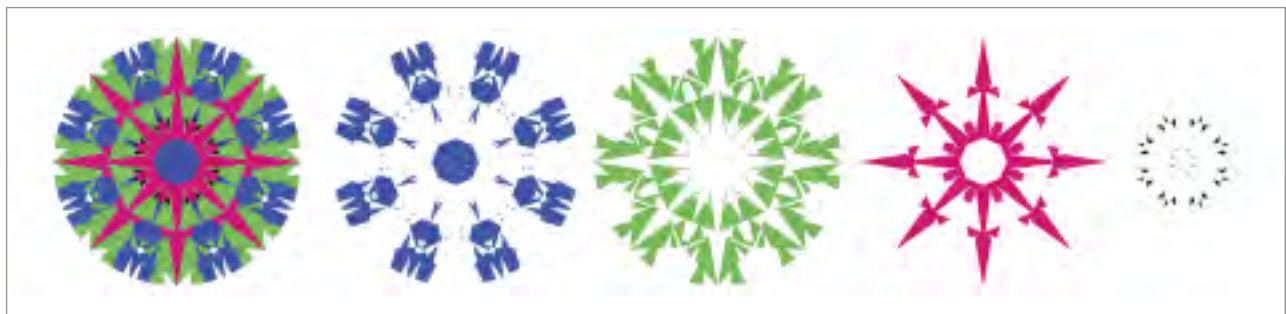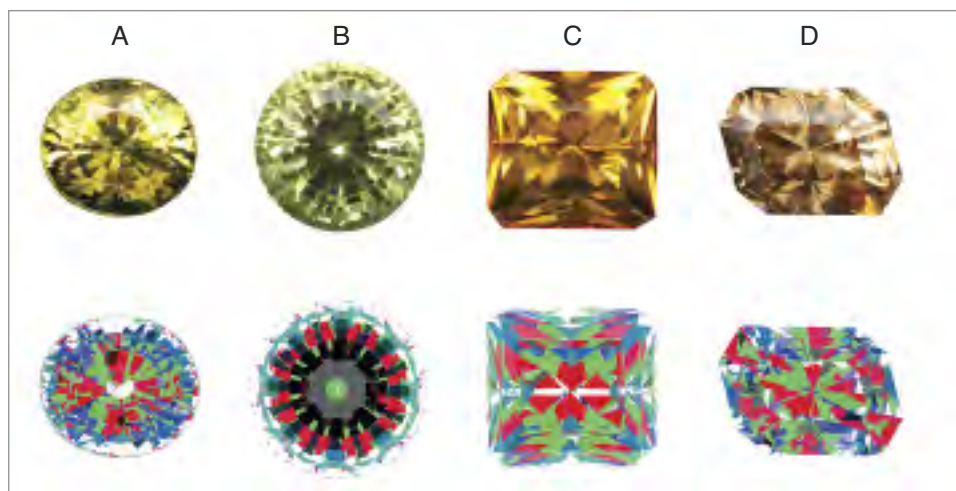
Figure 18. Four gemstones from GIA's Dr. Eduard J. Gübelin Collection were scanned using a non-contact optical measuring device to obtain a 3D image of each. Photos showing the representative patterns when viewed face-up are equated to the AG contrast maps derived from DiamCalc.

with white contrast map) is a reflection of the observer. Red and green indicate higher contrast areas of brightness, and some of the outer areas contain dull blue-green, resulting from lower-angle lighting. Again, the outer white areas are windows.

The next two examples show better cut optimization:

Figure 18C: Despite this amber's soft appearance (RI near 1.54) caused by facets that are slightly rounded and less crisp, its brightness—even when rocked—comes from effective use of high-angle entry light to provide dynamic contrast and minimal observer reflection (black). In the red areas of the map, the observer's reflection may come into view when the gem is slightly tilted. The prominent green areas represent a large amount of bright light entering the gem. The even distribution of red and green from culet to girdle adds to the attractiveness. Minimal areas of blue (lower-angle lighting) and white (windowing) keep this gem bright.

Figure 18D: This grossular garnet (RI near 1.74) is bright and does not window easily, even when rocked. Its brightness comes from the effective use of high-angle light entry to create a good mix of dynamic contrast, with little reflection of the observer. Red areas indicate that when the gem is slightly tilted, the observer's reflection may come into view. The abundance of green areas helps by directing bright light into the gem. For maximum visual appeal, the red and green areas should be evenly distributed and extend from culet to girdle. In this map, there is little blue (lower-angle lighting) or white (windowing).

APPLICATION TO GEMCAD-BASED OR 3-D WIREFRAME DESIGNS
The following discussion provides examples of how to read and interpret the AG contrast maps to optimize

cutting schemes. Six different GemCad designs specifically for quartz (or other gems with an RI near 1.55) were chosen from the DataVue file of GemCad designs. The name of the design, the creator, and the publication where it first appeared are listed. Each shows a table where the pavilion depth and crown height change by 1% of girdle width (and all pavilion and crown angles change accordingly). The resulting angles can be obtained from the GemCad file, but for simplicity this article uses crown and pavilion percentage differences. The table size is constant, as altering it would result in many more combinations. The original design's proportions are outlined and marked "original." For reference, the graphic design is also shown, accompanied by a contrast plot for an idealized round brilliant. The idealized contrast plot demonstrates the types of color distribution that contribute to effective designs. It serves as a visual reference for the types of dominant colors and balance that might be desired.

Design 13022 (figure 19): This design performs well with a variety of angle differences. It is a very forgiving design that can be used with a variety of crown heights to better utilize the rough. But note that all of these contrast plots have a predominance of green in the middle. Where does the contrast belong? Green represents brightness, but brightness alone is not terribly interesting. For more visual interest, a cutter could try a 46% pavilion/21% crown or a 47% pavilion/12% crown modification to add contrast. As mentioned before, trying several patterns will help identify which specific elements are the brightest and most attractive.

Design 13061 (figure 20): This example demonstrates the need for caution in trusting a cutting plan, regardless of the source. The original gem is fairly dull, perhaps due to a typographical error in the plan, a design not meant for quartz, or incorrect entering of the angles. While a large amount of red around the

London Shield
Norman Steele, *Seattle Facet Design*, Oct. 1988, p. 3

PAVILION DEPTH % ⟶

13022
DATAVUE #
RI 1.55
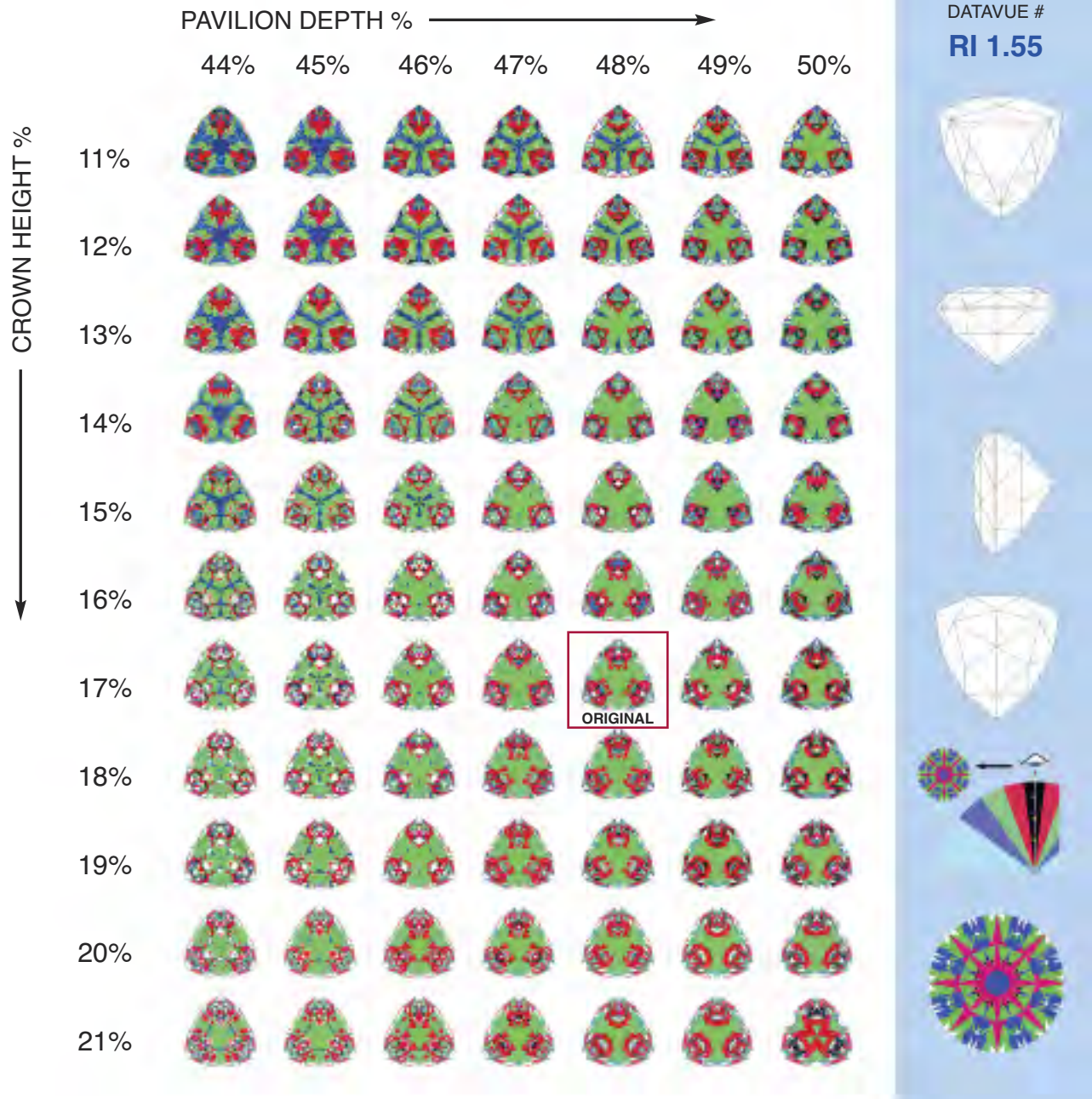
Figure 19. In this design, the six center pavilion main facets tend to gather light from the same direction, without breaking it up much (seen here as large green center areas). For more visual interest, a cutter could try a shallower crown and pavilion, which would give it more contrast into the center.

girdle edge does not always produce the best design, the 41% pavilion/11% crown combination may provide the most contrast, with some blue at the girdle edge to break up the red.

Design 13096 (figure 21): This design offers abundant contrast, and the resulting gemstone would be quite dynamic. Whereas the contrast areas with combinations of red and red/black can slightly darken the stone, green/red is generally a better combination. Designs should minimize blue

Barion Old Mine Triangle
Ben Dawson, *Facets*, June 1989

PAVILION DEPTH % ⟶

| | 36% | 37% | 38% | 39% | 40% | 41% | 42% |

CROWN HEIGHT %

10% 11% 12% ORIGINAL 13% 14% 15% 16% 17% 18% 19% 20%

13061
DATAVUE #
RI 1.55
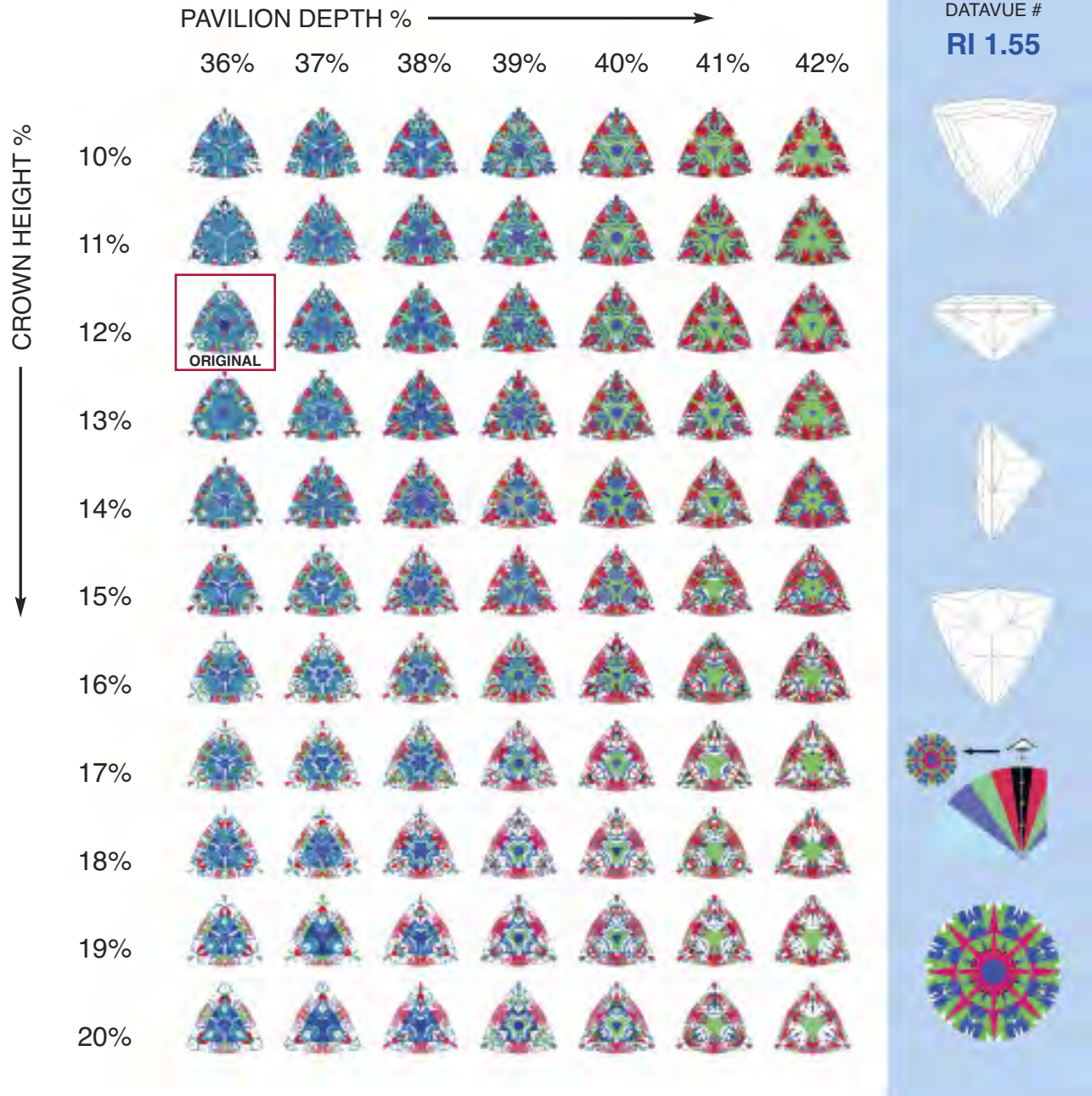
Figure 20. This design is fairly dull, and a much steeper pavilion and shallow crown would dramatically improve its appearance.

points in the center. For this design, a 45% pavilion/11% crown or 41% pavilion/17% crown would be more effective.

Design 13138 (figure 22): Of the triangular designs chosen for these illustrations, this is probably the most dynamic example. It is another forgiving design and also has high contrast all the way into the middle of the stone, with greens and reds throughout. While the original proportion set has a little too much blue in that quadrant of the plots, it would still produce a
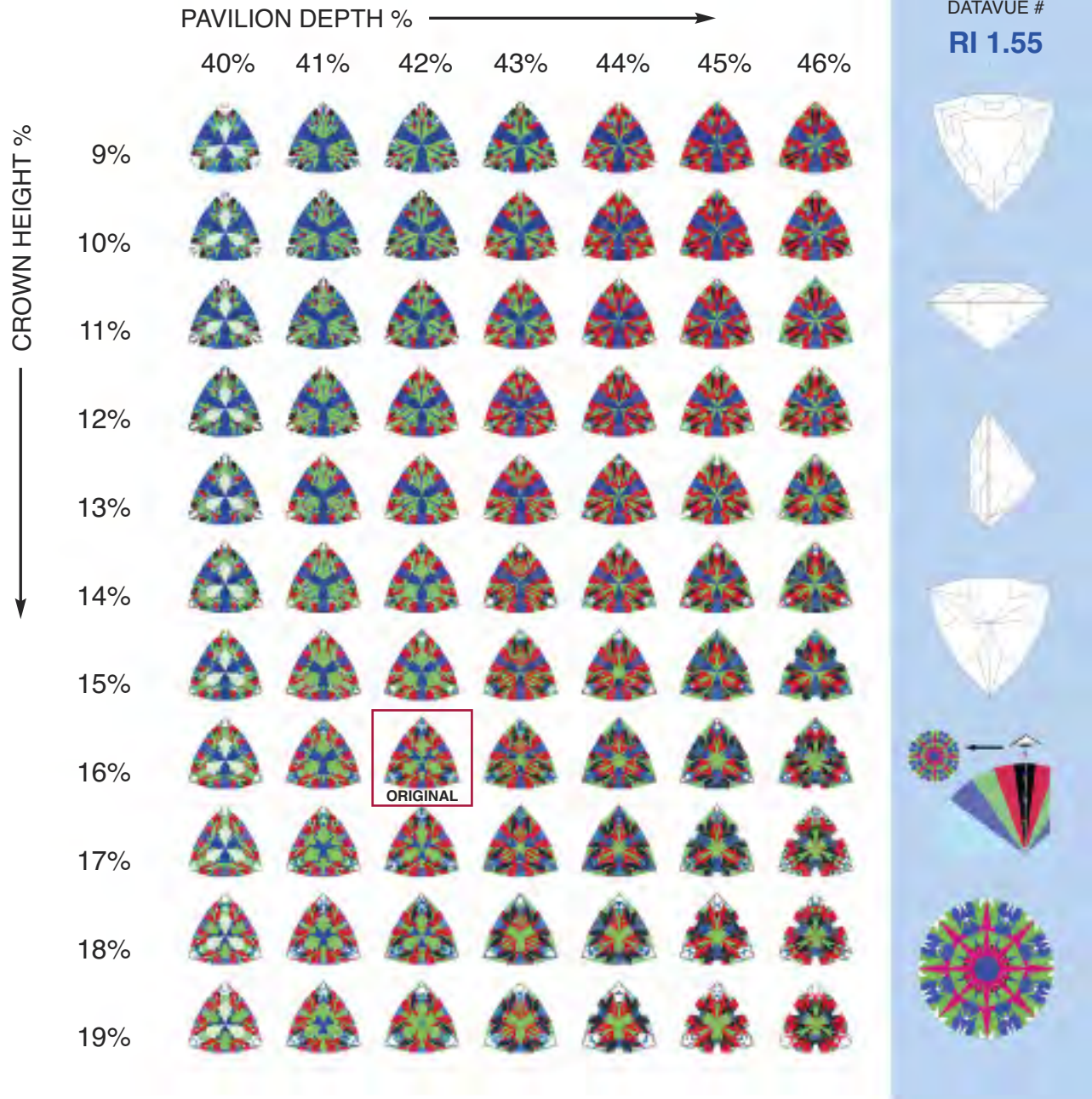
Figure 21. This design presents high contrast. The cutter merely needs to choose steeper pavilion angles (≥44% pavilion depth) and slightly shallower crown angles to avoid windowing.

very good appearance. Slightly increasing the pavilion depth—for instance, 47% pavilion/14% crown—would improve the design.

Design 13141 (figure 23): Note the prominence of red among these choices. The red areas start to pick up reflections of the observer (black areas) when slightly tilted, sometimes darkening the stone slightly. Therefore, this design should not be used with dark material, and only with slightly light or medium colors. The original angle combinations offer a good balance between contrasts of different light-entry angles. If the material is slightly dark, a

Trilogy
Robert Strickland, *TFG Newsletter*, Oct.-Dec. 1996, Vol. 17, No. 4, p. 18

13138
DATAVUE #
RI 1.55

PAVILION DEPTH % ⟶

CROWN HEIGHT %
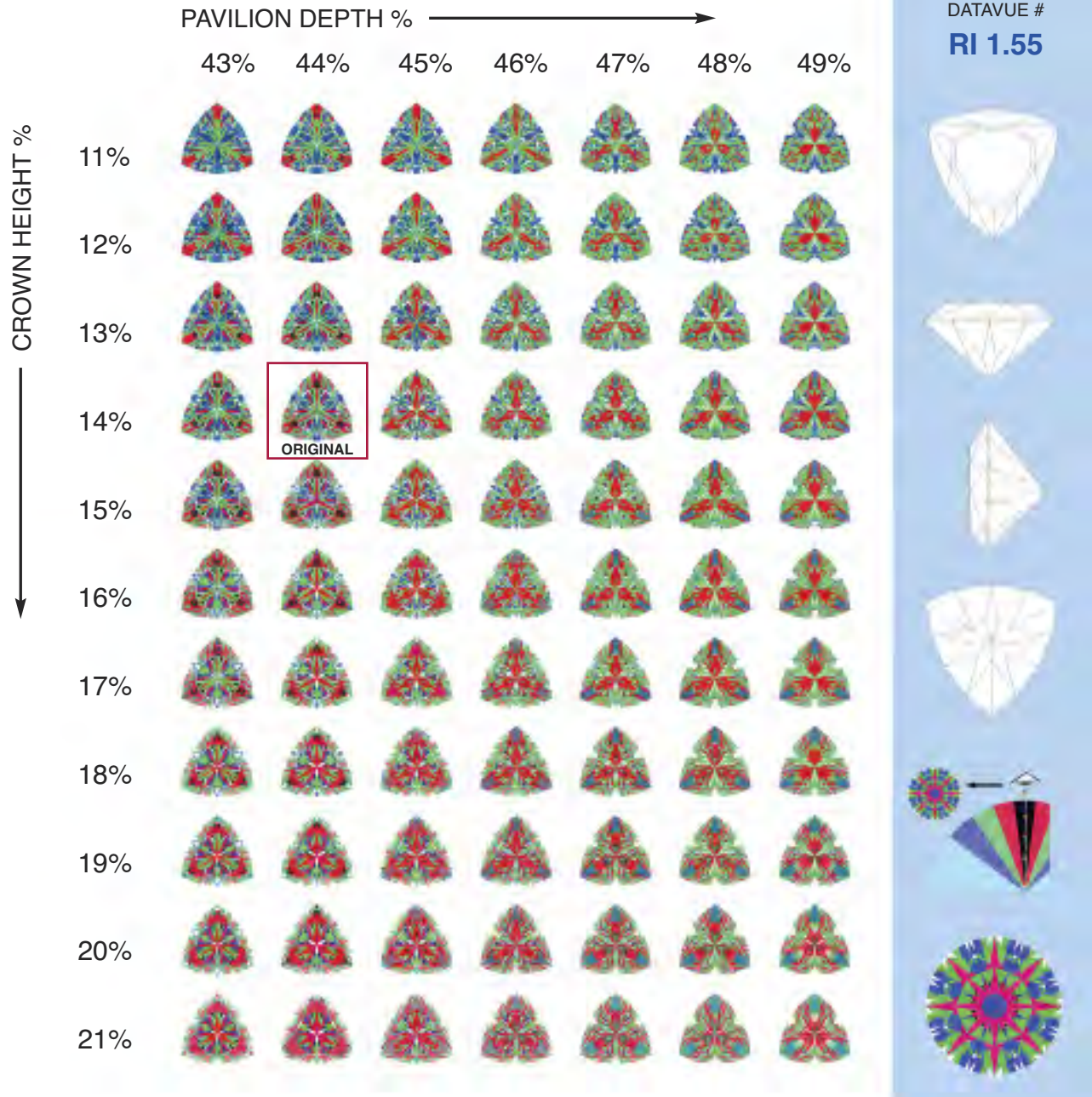
Figure 22. This is a forgiving design with high contrast into the center. With pavilion depths from 43% to 49% and a crown ranging from 12% to 17%, all working effectively, this design can be adapted to shallow or thick rough.

44% pavilion/12% crown will produce a little less darkness in the stone.

Design 13146 (figure 24): Note that this gem has a narrow range of feasible pavilion depth. At 45%, there is strong windowing, which also occurs in the white area in the 46% column. While not shown here, tilting the example in the 46% column will also produce windowing. At 50%, the substantial amount of blue (low-angle light entry) does not allow much brightness. The original proportions will work very well, but higher proportions of green in a contrast map—for instance, 48% pavilion/17% crown—are generally preferable. To

Brazil Cushion Triangle 1

Richard C. Walker, *Facets*, Sept. 1988, p. 3

PAVILION DEPTH % ⟶

13141
DATAVUE #
RI 1.55

CROWN HEIGHT %

| | 44% | 45% | 46% | 47% | 48% | 49% | 50% |

9%
10%
11%
12% — ORIGINAL
13%
14%
15%
16%
17%
18%
19%
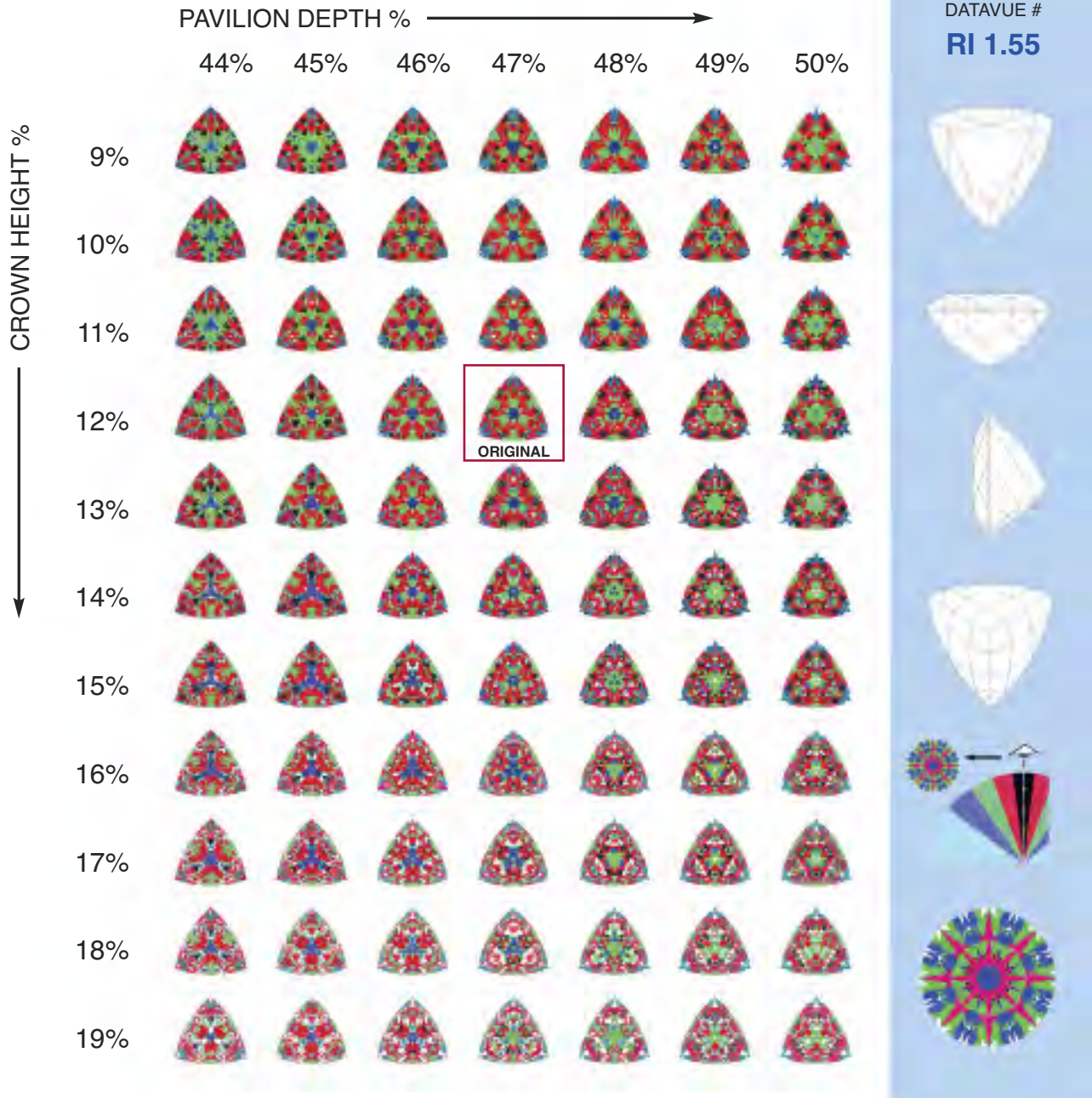
Figure 23. Another forgiving design with high contrast, this should be used with lighter materials. The red areas start to pick up reflections of the observer when the stone is tilted, darkening its appearance.

achieve good contrast, the adjoining facets need to have offset angles. This design only does so in a very narrow range of proportions.

Computer modeling can assist in effective design by simulating the best angle combinations and/or modifying the design (adding or removing facets, or changing their placement). By using lighting schemes such as AG and ASET in design planning, facet arrangement can be optimized to produce the most visually interesting results.

Third Millennium

Ernie Hawes, *New Mexico Facetor*, Nov.-Dec. 1999
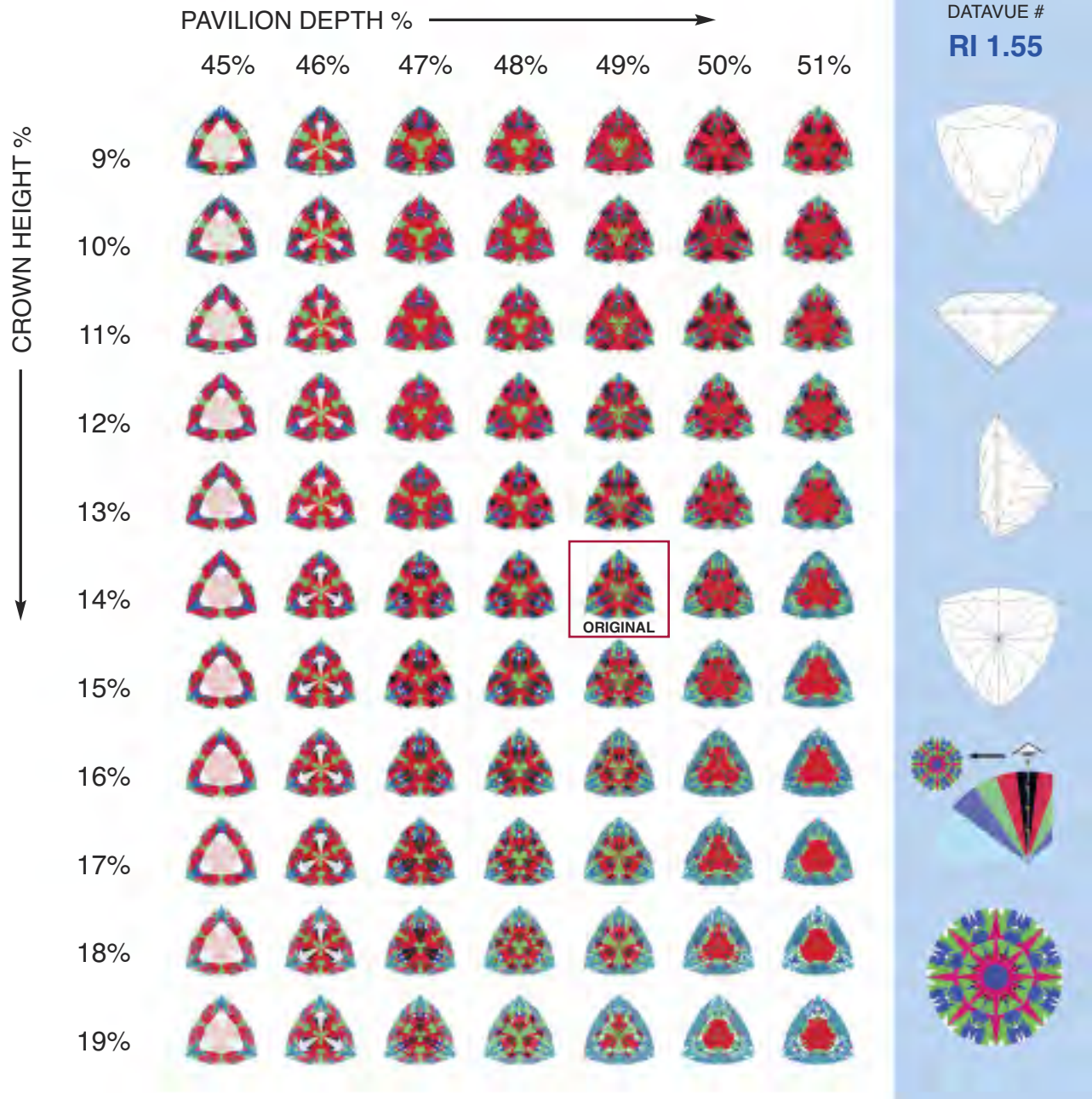
Figure 24. This design is effective in a limited range of proportions and should be used with lighter materials.

GENERAL CUTTING CONSIDERATIONS

1. Designs for equal-sided gems (e.g., square, round, equilateral triangular) can easily be made more dynamic. Elongated shapes are inherently more difficult to optimize to the same degree.

2. Step cuts are more difficult to optimize. With the addition of four or more rows on the pavilion, the difficulty increases. In optimizing step cuts, very careful attention must be paid to step width, as well as the design execution.

Figure 25. Each image shows a 2° rotation clockwise from the previous image. A spot light source contributes a small amount of fire (seen here as red, blue, green, or yellow virtual facets). As the gem is rotated, some virtual facets go from light to dark (examples are circled). As a facet nears the border between light and dark, the observer will see fire. Some of these flares of color last through larger degrees of rotation than others (larger red circles). While not illustrated, when a facet only slightly darkens or lightens, fire is faint. Strong changes in contrast create stronger fire. More fire is exhibited by materials of higher dispersion values.

3. Some designs are more effective for certain RI ranges than others. For example, the standard round brilliant is far more effective for gems with a high RI (diamond, zircon, etc.) than for lower-RI materials.

4. The gem's physical size also dictates design considerations. For example, when cutting a 10 mm gem, a simple single-cut design with eight pavilion and eight crown facets (plus the table facet) is not as effective as a 57-facet round brilliant design. A 181-facet design, for instance, does not succeed unless the gem is of substantial size, because tiny facets are less distinct and look "fuzzy."

5. Adding small facets to designs that contain large facets is rarely practical. For example, splitting stars into three small facets while leaving the others at a normal size will have little effect and may actually diminish the design. Often that center facet provides less contrast than if there were only two facets.

6. Every now and then, faceters concern themselves with dispersion, which jewelers refer to as "fire." It is a measurement that indicates how much light is spread by different materials. Generally, lower-RI gems do not contain much visible fire. Adding color saturation to the material hides what little fire might be there. On the other hand, highly dispersive gem materials (with dispersion values above 0.039) provide some unique opportunities to display fire. This effect depends on two considerations:

   a. Lighting environment: Where the lighting is primarily diffused (e.g., reflected from a white ceiling with no direct spot-type source directed at the gem), the observer will see little fire. If the lighting environment provides strong contrast, using bright spot-lighting against a dark background, fire is strongly enhanced.

   b. Strong contrast: Areas of strong contrast in the gem will create fire as those areas alternate between dark and bright when the gem is rotated. Figure 25 shows a gem being rotated in 2° increments with the light source in a fixed position. As the gem is rotated, the movement of facets causes them to fluctuate between dark and light. At the threshold between light and dark, the observer will see fire. If the gem is moved slowly, with facets only slightly changing in relation to the light source and the reflection to the eye, the change in color of the facet will be gradual. If movement is sudden, the observer may only see where the facet is dark and then light, without seeing the fire. When a facet only slightly darkens or lightens, fire is faint.

Following these rules for optimization, such as creating a design with strong contrast, will also improve the appearance of a gem and increase its fire.

Before implementing personal preferences, the faceter should be aware that the colored gem market is very focused on color: hue, saturation and tone. Color quality is critical, but often suffers in lightly colored gems when the design is modified toward brightness. Instead, optimization may be needed to enhance the color first and foremost, with scintillation a secondary priority. Understanding the elements of brightness can help the faceter achieve it without compromising color.

REFERENCES

Albert M.K. (1995) Genericity and the Perception of Visual Contours and Surfaces. Ph.D. dissertation, University of California, Irvine, p. 25.

Caudill J., Sasian J., Yantzer P. (2008) Methods, apparatus, and systems for evaluating gemstones. US Patent number: 7336347, filed Dec 20, 2004, issued Feb. 26, 2008.

Cowing M. (2009) Describing diamond beauty—assessing the optical performance of a diamond. ACA Gem Laboratory, http://www.acagemlab.com/articles/Describing.htm [date accessed: Aug. 30, 2012].

Gilbertson A. (2003) Device for judging symmetry, brightness, and efficacy of light return in precious stones. U.S. Patent 6665058, filed May 24, 2000, issued Dec. 16, 2003.

Harding B. (1975) Faceting limits. *G&G*, Vol. 15, No. 3, pp. 78–88.

Hoffman D. (1998) *Visual Intelligence: How We Create What We See.* W.W. Norton & Co, New York, NY.

GIA (2006) Diamond Grading Lab Manual. Gemological Institute of America, Carlsbad, California, p. 21.

Kanizsa G. (1955) Margini quasi-percettivi in campi con stimolazione omogenea [Quasiperceptual margins in homogenously stimulated fields]. *Rivista di Psicologia*, Vol. 49, No. 1, pp. 7–30. Translated by W. Gerbino, in Petry and Meyer, 1987, pp. 40–49).

Petry S.J., Meyer G.E. (1987) *The Perception of Illusory Contours.* Springer-Verlag, New York, NY.

Purves D. (2011) An empirical explanation: Simultaneous brightness contrast. Center for Cognitive Neuroscience, Duke University, http://www.purveslab.net/research/explanation/brightness/brightness.html [date accessed: Aug. 30, 2012].

Reflector technologies (undated) Good Old Gold, www.goodoldgold.com/technologies/reflectortechnologies/history [date accessed: June 5, 2013].

Sarcone G., Waeber M.-J. (undated) Colors of the mind, http://www.archimedes-lab.org/color_optical_illusions.html [accessed on Aug. 30, 2012].

Sasián J., Quick J., Sheffield J., Caudill J., Yantzer P. (2007) Evaluation of brilliance, fire, and scintillation in round brilliant gemstones. *Optical Engineering*, Vol. 46, No. 9, p. 60936014–6093625.

White M. (1979) A new effect on perceived lightness. *Perception*, Vol. 8, pp. 413–416.

For online access to all issues of GEMS & GEMOLOGY, visit:

gia.edu/gems-gemology

FLUORESCENCE PRODUCED BY OPTICAL DEFECTS IN DIAMOND: MEASUREMENT, CHARACTERIZATION, AND CHALLENGES

Yun Luo and Christopher M. Breeding

Three-dimensional fluorescence spectra were collected from both natural-color and treated diamonds with common color centers (including N3, H3, H4, 480 nm, and N-V) to characterize the fluorescence produced by each defect. Unlike individual spectra, 3D presentations of multiple spectra allow quick and simultaneous determination of the fluorescence-producing defect(s), the excitation energy that yields maximum fluorescence intensity, the variation of fluorescence with excitation, and the peak position and band shape of individual and overall fluorescence emissions. The combination of 3D fluorescence spectra from common defects and emission spectra from several standard ultraviolet light sources revealed noticeable inconsistencies in the fluorescence observed. Our data indicate that variations in UV lamp output can significantly affect the fluorescence color observed in gem diamonds.

Fluorescence is the emission of electromagnetic radiation (e.g., visible light, ultraviolet light, X-rays, and gamma rays) from a substance, stimulated by the absorption of incident electromagnetic radiation. The emission persists only as long as the stimulating radiation is continued. The terms *fluorescence* and *photoluminescence* often appear interchangeably, but gemologists commonly use the former to describe the visible light emission from ultraviolet (UV) excitation. In most cases the emitted light has a longer wavelength, and therefore lower energy, than the absorbed radiation. Diamonds containing no defects or impurities generally do not absorb visible and UV light (>230 nm) and thus produce no color or fluorescence. But when impurities or defects (often referred to as *color centers*) are present, they may absorb visible and UV light to produce color, fluorescence, or both. In diamonds with multiple color centers, the fluorescence from one defect may even excite the emission from another center more efficiently than the external UV light. Conversely, the fluorescence from one color center may be absorbed by other defects, dramatically reducing the overall fluorescence. *Phosphorescence* commonly refers to visible light emitted by a diamond after the stimulating UV light source has been discontinued. While related to fluorescence, it is a relatively uncommon visual property of gem diamonds and not a focus of this study.

Fluorescence in diamonds has been studied for nearly a century (e.g., Becquerel, 1868; Mani, 1944; Shipley, 1947; Wild and Biegel, 1947; Cotty, 1956; Dyer and Matthews, 1958; Collins, 1974, 1982; Fritsch and Waychunas, 1994; Eaton-Magaña et al., 2007; Holloway, 2009; Shigley and Breeding, 2013). While much is known and published about diamond defects and fluorescence, most gemologists do not have ready access to this information. This article seeks to clearly outline the defects that cause fluorescence in diamond, and explain how the gemological tools used to evaluate this property may impact observations. For decades, investigations of diamond fluorescence have mainly focused on visual observation (Moses et al., 1997; figure 1), while more recent studies have dealt with individual spectra and the physics of individual defects. The application of 3D fluorescence spectroscopy has been limited. Eaton-Magaña et al. (2007)
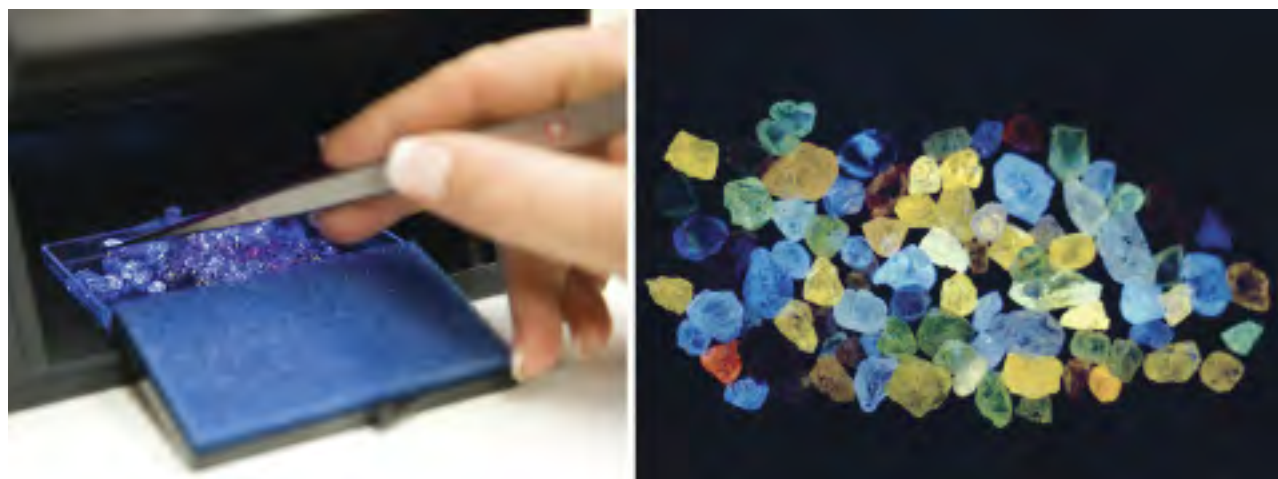
Figure 1. For decades, UV lamps have been used in the jewelry industry and by gemological laboratories to assess diamond fluorescence. Left: A gemologist examines fluorescence reactions from a suite of colorless faceted diamonds in a long-wave UV fluorescence box. Right: A group of rough stones illustrates the range of fluorescence colors seen in diamond under LWUV excitation. Note that GIA evaluates fluorescence of individual stones, not in bulk as shown here. Photos by Eric Welch.

presented a few spectra for diamond in this format, and Hoover and Theisen (1993) investigated other colored gemstones with this approach.

Visual evaluation of fluorescence is standard practice in gemological laboratories, and fluorescence color and intensity are often documented on laboratory reports. When selecting diamonds, jewelers also rely on fluorescence to ensure a good color match under a variety of lighting circumstances. The most common excitation source is a handheld UV lamp, which often has dual modes for long-wave (LW) and short-wave (SW) UV radiation. The typical color centers in diamond fluoresce more intensely under LWUV excitation. Fluorescence assessment relies mainly on visual observation at room temperature—fluorescence can vary in intensity and color at different temperatures—and sometimes requires a set of reference diamonds for comparison. Observation of fluorescence can be affected by three main factors: (1) the nature of the emission from the UV light source; (2) the nature of the defect(s) responsible for the fluorescence; and (3) methodology, including the viewing geometry and the distance from the radiation source. Within current industry practices, complications exist for each of these factors.

First, the excitation produced by different light sources may vary and not consist of "pure" LWUV or SWUV light, which generally have wavelengths of 365 nm and 254 nm, respectively. Differences in excitation wavelengths between lamps may produce inconsistent fluorescence reactions. Warm-up time,

the materials used in the UV filters, and aging of lamps and filters can also affect the radiation output. Secondly, multiple defect centers may exist within the same diamond and produce different emission peaks simultaneously. To the human eye, multiple emissions combine to produce a single, albeit mixed, fluorescence color (e.g., blue + yellow = apparent whitish fluorescence). Visual evaluation of fluorescence does not allow for identification of multiple defects or irregular emission peaks. Finally, the distance between the radiation source and the diamond as well as the stone's orientation (table-down versus face-up) may produce noticeably different fluorescence by changing the amount of excitation energy that interacts with the diamond.

In this study, a high-resolution luminescence spectrometer was used to study fluorescence emissions from common color centers in gem diamonds by obtaining three-dimensional scans of excitation, emission, and fluorescence intensity. From the 3D scans, we can quickly and simultaneously determine the nature of observed fluorescence and the energy at which the fluorescence maximizes or changes by systematically varying the excitation energy wavelength. Furthermore, emission characteristics such as peak position and band shape that are characteristic of particular defect centers can be evaluated.

With detailed, direct knowledge of fluorescence-producing diamond defects in hand, we surveyed several common UV light sources to better understand how much variability exists in UV excitation and to
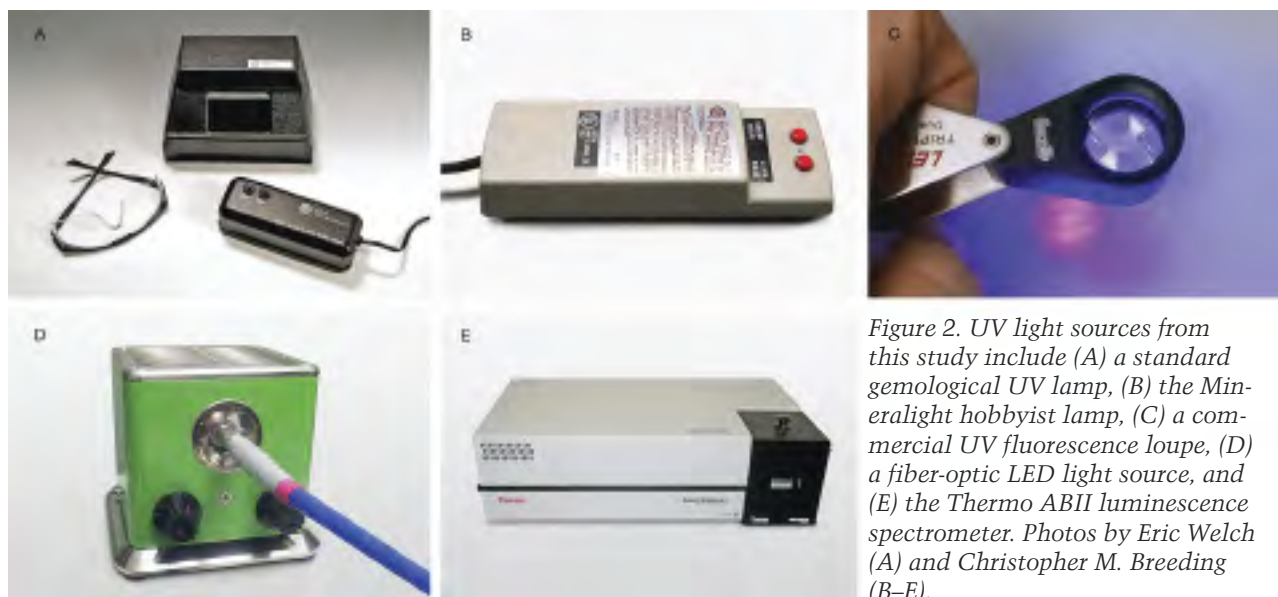
Figure 2. UV light sources from this study include (A) a standard gemological UV lamp, (B) the Mineralight hobbyist lamp, (C) a commercial UV fluorescence loupe, (D) a fiber-optic LED light source, and (E) the Thermo ABII luminescence spectrometer. Photos by Eric Welch (A) and Christopher M. Breeding (B–E).

further investigate the effect of UV source on observed fluorescence colors. While a few previous articles have made similar investigations (e.g., Eaton-Magaña et al., 2007; Pearson, 2011), our survey includes newer LED-based sources that have only recently seen widespread use in the industry. The outcome of this study could be beneficial to both the diamond industry and gemological laboratories in that accurate, consistent, and reproducible fluorescence measurements are vital for industry confidence. In addition, better methods for measurement of fluorescence from different defect centers may lead to more effective methods of detection and separation of natural, synthetic, and treated diamonds.

MATERIALS AND METHODS

Samples. Three-dimensional fluorescence spectra were collected from 25 faceted diamonds, including 19 natural-color samples and six treated by high-pressure, high-temperature (HPHT) and irradiation (table 1). GIA issues reports on thousands of colored diamonds each year, providing a large selection of samples. The diamonds in this study, all of which carried GIA reports indicating natural- or treated-color origin, were chosen as representative of their respective defect group. While multiple fluorescence-producing color centers occur in most diamonds, each of our samples was dominated by one of the following:

1. N3 center
2. H3 or H4 center
3. 480 nm band
4. N-V center

Emission Spectra from Industry UV Light Sources. To evaluate the excitation energy produced, we collected emission spectra from various UV light sources over the 200–900 nm range using an Ocean Optics USB 2000 CCD spectrometer with a UV-transmitting fiber-optic cable. Output spectra from five UV sources—including a GIA UV lamp (model

In Brief

- 3D fluorescence spectra allow quick, simultaneous characterization of the excitation energy that maximizes fluorescence, variation in fluorescence with excitation, as well as position and band shape of individual and overall fluorescence emissions.

- Common mercury-based UV lamps and LED-based UV loupes do not produce pure 365 nm LWUV emissions.

- UV lamp output variation can significantly affect fluorescence color and intensity observed in diamond.

- A standardized UV excitation source is necessary for accurate and reproducible determination of fluorescence.

745000), a custom-made GIA fluorescence measurement device with UV LEDs (not shown), a handheld UVP Mineralight hobbyist lamp, a UV LED loupe, and a commercial 365 nm LED light source (figure 2, A–D)—were measured and output peak positions were recorded.

3D Luminescence Spectroscopy. A Thermo Aminco Bowman II (ABII) luminescence spectrometer (figure
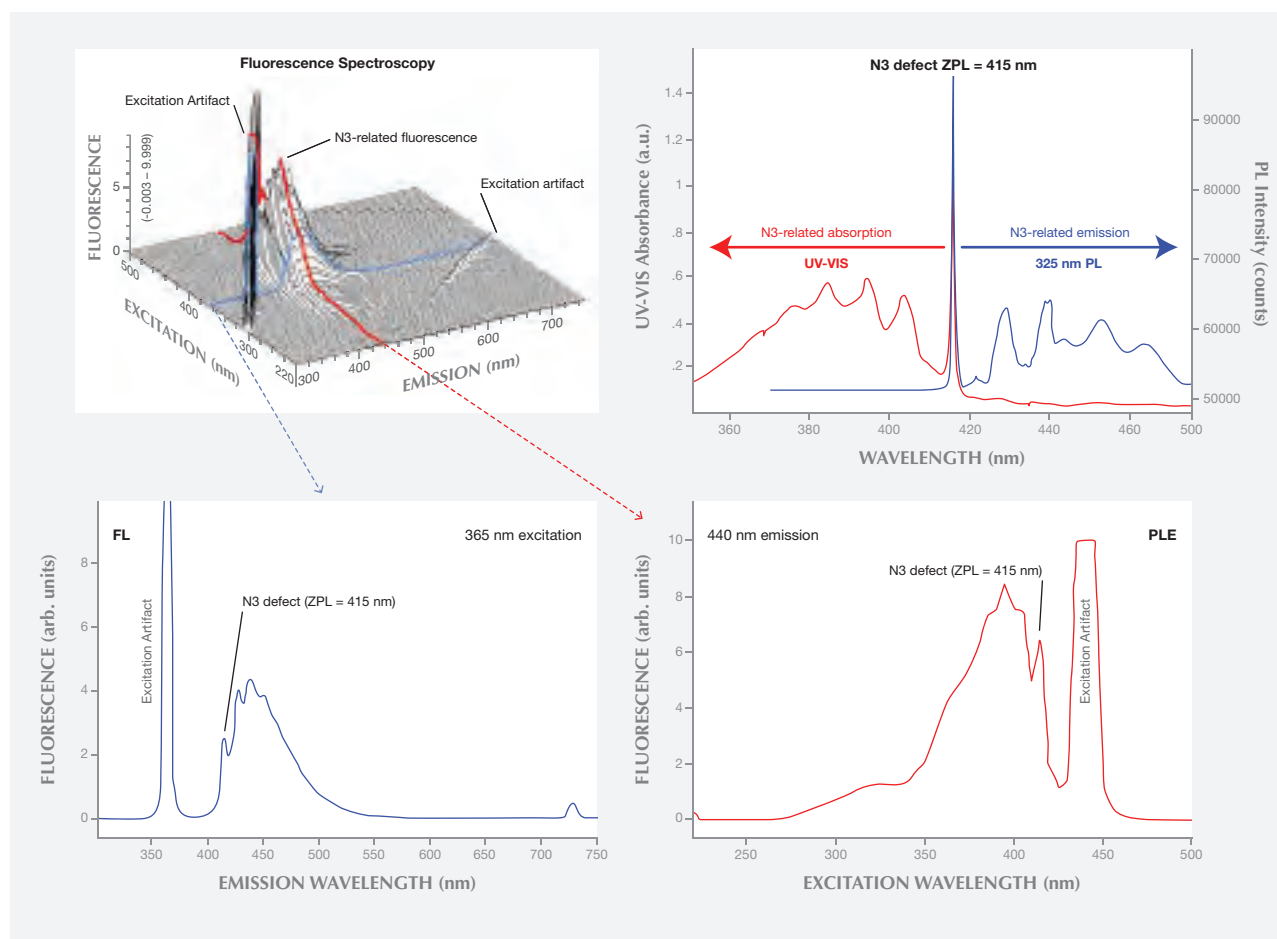
Figure 3. Top left: 3D fluorescence spectra are composed of many individual fluorescence spectra collected at different excitation wavelengths. This example from a colorless diamond containing N3 defects (sample 2) shows how a single spectrum (top left, blue line) at a given excitation (365 nm) can be extracted and examined in detail (bottom left). PLE excitation spectra can also be extracted from the 3D data (top left, red line and bottom right). Top right: Absorption (UV-Vis) and PL emission spectra confirm the presence of a defect such as N3 and relate to the data taken from a 3D spectrum. Fluorescence (bottom left) and PL (top right, blue line) emissions from the defect are similar and longer in wavelength than the ZPL, whereas PLE (bottom right) and UV-Vis absorption spectra (top right, red line) correlate and show defect-produced bands at wavelengths shorter than the ZPL.

2E) was used to investigate the samples' fluorescence. The analyses were conducted at room temperature to simulate typical observation conditions. Three-dimensional fluorescence spectra were recorded in the 300–750 nm emission range (2 nm resolution, 4 nm bandpass) using an excitation of 220 to 500 nm (5 nm intervals, 4 nm bandpass). Detector voltage was adjusted so that the highest peak in the spectrum comprised 80%–90% of the instrument's maximum fluorescence intensity range. The ABII spectrometer is not configured with excitation filters, so most of the 3D spectra collected contained first-, second-, and sometimes third-order artifacts produced by the spectrometer grating at 1×, 2×, and 3× the excitation wavelength. In most of the spectra

presented, the 2× and 3× artifacts have been removed. The 1× artifact was retained to avoid potential data loss.

Each 3D scan took approximately four hours to complete and consisted of 57 individual spectra. The advantage of a 3D plot is that all aspects of excitation and emission can be derived. Any of the 57 fluorescence emission spectra for a given excitation can be separated, and data for excitations not specifically analyzed can be interpolated. In addition, photoluminescence excitation (PLE) spectra for a given emission wavelength can be obtained to see the effect of excitation light frequency on fluorescence. Figure 3 illustrates these features in the anatomy of a 3D fluorescence spectrum.

Additional Absorption and PL Spectroscopy. Ultraviolet/visible/near-infrared (UV-Vis-NIR), Fourier-transform infrared (FTIR), and photoluminescence (PL) spectra were collected to complement the fluorescence data, providing additional detail about the defects under more readily measurable conditions (again, see figure 3). UV-Vis-NIR spectra were collected with an Ocean Optics integrating sphere and HR 4000 CCD spectrometer over the 380–1000 nm range (~1 nm resolution) at ~77K temperature. FTIR spectra (not shown) were collected to identify diamond type using a Thermo Nexus 6700 FTIR spectrometer (6000–400 cm^{-1}, 1 cm^{-1} resolution, 128 scans, room temperature). Breeding and Shigley (2009) describes diamond type and its use in gemology. Photoluminescence spectra were collected using a Renishaw inVia Raman microscope (325, 488, 514, 633, and 830 nm laser excitations, various scan ranges, and ~77K temperature).

RESULTS

UV Light Sources. *GIA UV Lamp.* Gemologists use conventional UV lamps (figure 2A) to observe a stone's fluorescence color in response to long- or short- wave radiation. The lamps in this study were sold by GIA Instruments until 2009 and are still prevalent in the trade. It is well known that traditional UV lamps do not provide single characteristic 365 nm (LWUV) and 254 nm (SWUV) emission lines (Williams, 2007; Pearson, 2011) due to the variety of materials used in UV filters and the aging of lamps and filters. Rather than a single 365 nm emission peak, LWUV lamps often emit 404 and 435 nm lines and a broad band that extends from the UV to the visible region of the spectrum. Similarly, SWUV lamps always have distinct peaks at 254, 315, and 365 nm instead of a single 254 nm emission. All of these emission lines, as well as several weaker ones, are produced by the mercury lamp inside the units. The filter materials used to remove mercury radiation are not 100% efficient and leak undesired emissions. As the filters age, the leaked emissions become stronger and more prominent.

Examination of two handheld UV lamps manufactured by GIA and used at its laboratory revealed a major peak at 368 nm (FWHM = 17 nm) with LWUV excitation, accompanied by a small peak at 404 nm (figure 4A). In addition to the 252 nm (FWHM = 3 nm) SWUV emission, which shifted 2 nm from typical 254 nm SWUV, there were major peaks at 312, 365, 404, and 435 nm, as well as minor peaks at 296, 302, and 334 nm. Interestingly, the peak intensity at

365 nm (the typical LWUV emission) was more intense than the 252 nm SWUV peak (figure 4B), likely due to filter aging. The existence of this intense 365 nm peak in the excitation may have a pronounced effect on what is observed as SWUV fluorescence. Because most gemologists use UV lamps for many years and never replace the filters, these tests are representative of industry practices.

UVP Mineralight Lamp. The UVP Mineralight is another dual LW-SW lamp widely used in the industry and by hobbyists (figure 2B). Though similar in appearance and function to the GIA UV lamps, this lamp showed different results. LWUV excitation produced an intense broad band at 355 nm, along with the primary LW peak at 365 nm (FWHM = 37 nm) and weak emissions at 313, 405, and 437 nm. Shortwave excitation showed a similar array of peaks using the GIA lamp, with major emissions at 254 (FWHM = 4 nm), 313, and 366 nm, as well as minor peaks at 297, 303, 335, and 405 nm (figures 4C and 4D).

Note: Both the GIA and Mineralight lamps are able to produce LWUV and SWUV because they contain low-pressure mercury lamps that emit initially sharp mercury lines, but the phosphors inside the lamp are creating a conversion to broadband wavelengths at a longer wavelength. The lamps emit a range of light that spans both LWUV and SWUV. They are equipped with a daylight filter that removes most of the visible light so that mainly the desired UV band passes through the filter (R. Geurts, personal communication, 2012).

Digital GIA LED Fluorescence Device. GIA uses a custom-made fluorescence meter with LWUV LEDs to measure the fluorescence intensity documented on its diamond grading reports. Designed to improve fluorescence measurement consistency, this instrument uses an LED excitation source with a single emission peak at 367 nm and an FWHM of 14 nm (figure 4E).

UV LED Loupe. A generic commercial UV loupe sometimes used in the trade (figure 2C) was also examined. The LED excitation source from this loupe gave a single peak at 403 nm with an FWHM of 17 nm (figure 4F).

Commercial LED Light Source. For comparison with the other LED sources, we also tested a commercially available "365 nm" LED light source manufactured by Ocean Optics (figure 2D). This excitation
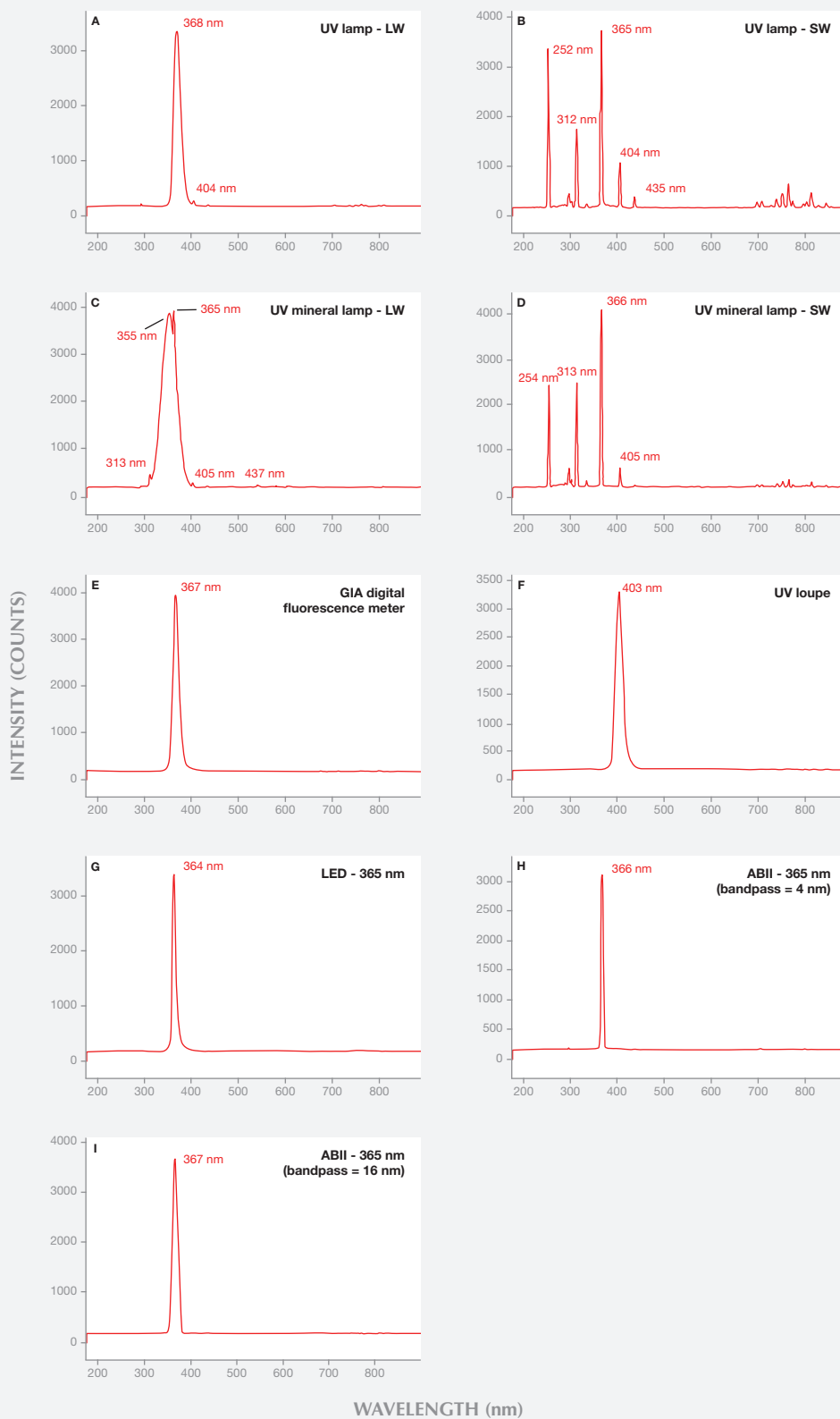
SPECTRA FROM UV LIGHT SOURCES

Figure 4. The UV light sources from this study showed clear differences in emission characteristics.

TABLE 1. Diamonds examined in this study.

Sample	Natural color or treated	Color[a]	Weight (ct)	Shape	LWUV reaction[b]	SWUV reaction[b]	Prominent color center
1	Natural	Colorless (D)	1.10	Round	Medium green	None	
2	Natural	Colorless (D)	0.37	Round	Strong blue	Medium green	
3	Natural	Colorless (E)	0.31	Round	Medium blue	None	
4	Natural	Near-colorless (I)	1.12	Round	Strong blue	Weak green	N3
5	Natural	Near-colorless (I)	1.51	Round	Strong blue	Weak green	
6	Natural	Faint yellow (L)	1.01	Cushion	Strong blue	Medium green	
7	Natural	Very Light pink	1.02	Heart	Strong blue	Medium blue	
8	Natural	Fancy Light greenish yellow	0.14	Round	Strong yellow	Medium yellow	
9	Natural	Fancy yellow-green	0.69	Round	Strong blue + yellow (uneven)	Medium blue + yellow (uneven)	
10	Natural	Fancy Intense greenish yellow	1.01	Heart	Medium to strong yellow + blue	Weak yellow	H3
11	HPHT-treated	Fancy Vivid green-yellow	2.34	Round	Strong green + weak blue	Medium green	
12	Natural	Fancy Intense yellowish green	3.10	Rectangle	Very strong green	Strong green	
13	Natural	Fancy Light yellow-green	0.58	Round	Strong green	Strong green	H4
14	Natural	Fancy Light yellowish green	1.04	Round	Strong green	Medium green	
15	Natural	Fancy Deep orange-yellow	0.40	Round	Strong yellow	Medium yellow	
16	Natural	Fancy Deep brownish orangy yellow	1.62	Pear	Strong orange	Medium to strong orange	
17	Natural	Fancy Vivid yellow-orange	0.72	Pear	Strong orange	Strong orange	480 nm band
18	Natural	Fancy Intense orange-yellow	1.02	Marquise	Strong orange	Strong yellow	
19	HPHT-treated	Fancy Intense orangy yellow	0.19	Round	Strong yellow	Medium yellow	
20	HPHT-treated	Fancy Intense yellow	0.39	Round (partial)	Strong orange	Medium orange	
21	Natural	Fancy brown-pink	1.51	Old Mine	Weak red	Weak to medium red	
22	Natural	Very Light pinkish brown	2.01	Pear	Very weak orange	Very weak orange	
23	HPHT-treated and Irradiated	Fancy red	1.49	Square	Weak red	Medium red	N-V
24	HPHT-treated and Irradiated	Fancy Deep pink	0.90	Oval	—	—	
25	Irradiated	Fancy red	0.17	Round	Strong red	Very strong red	

[a]Assigned using standard GIA color grading practices.
[b]LWUV and SWUV reactions were observed using excitation from a standard handheld UV lamp.

source showed a single peak at 364 nm with an FWHM of 10 nm (figure 4G).

ABII Excitation Light Source. The ABII spectrometer (figure 2E) was selected to provide well-constrained, high-resolution fluorescence spectra. To understand how its excitation compared to that of other sources, different excitation wavelengths of the ABII CW Xenon source were examined (the instrument can produce excitation of 200–950 nm). As shown in figures 4H and 4I, when the instrument was set to 365 nm excitation with 4 nm bandpass, the resultant

emission showed a narrow peak at 366 nm with an FWHM of 5 nm. With a 16 nm bandpass parameter (which most closely resembled the output of a GIA LW-UV lamp), a peak was observed at 367 nm with an FWHM of 15 nm. To precisely characterize the fluorescence from a given excitation wavelength, we chose the smallest available bandpass setting (4 nm), and thus the narrowest excitation emission, for the 3D-fluorescence spectra collection.

N3 Center. The N3 center is the most common color-producing defect in diamond, consisting of a va-

Figure 5. Diamonds with N3 defect centers include samples 1–3, which are colorless (1 and 3 have a brownish hue); samples 4–6, which are near colorless to faint yellow (not shown); and sample 7, a pink diamond with both N3 and H3 defect centers. Samples with the H3 center (8–11) and H4 center (12–14) are yellow to light green. Diamonds with the 480 nm band (15–20) are yellow to orange, while those with N-V centers (21–25) are pale to intense pink or red. Photos by Don Mengason and Robison McMurtry.

cancy surrounded by three nitrogen atoms on a {111} plane. The zero phonon line (ZPL), the identifying emission for N3, occurs at 415 nm. This line, along with a broadband emission with dominant peaks at 429, 439, and 450 nm, results in typical blue fluorescence (Collins, 1982).

Absorption and PL Spectroscopy. UV-Vis-NIR spectra for samples 1–7 all showed the N3-related ZPL at 415 nm. Sample 7 also showed a 550 nm band, which causes the stone's pink bodycolor. FTIR analysis identified them as type Ia diamonds with both A and B nitrogen aggregates in various concentrations. Samples 1 and 3 showed more A aggregates, which are known to quench fluorescence (Collins,

1982), possibly explaining the weaker fluorescence observed (table 1). PL spectra confirmed the presence of N3 in sample 2 (figure 3). The 503.2 peak in the PL spectra of samples 1, 3, and 7 revealed an H3 center as well. The H3 center in sample 1 was the source of the visible greenish component of the fluorescence.

Fluorescence Spectroscopy. Among the seven diamonds examined in this category, six have color in the D-to-Z range (colorless to pale yellow) and one has a light pink color (figure 5). All seven showed relatively intense fluorescence emission, with the ZPL at 415 nm and three peaks at 429, 439, and 450 nm superimposed on a ~400–550 nm broadband, all charac-
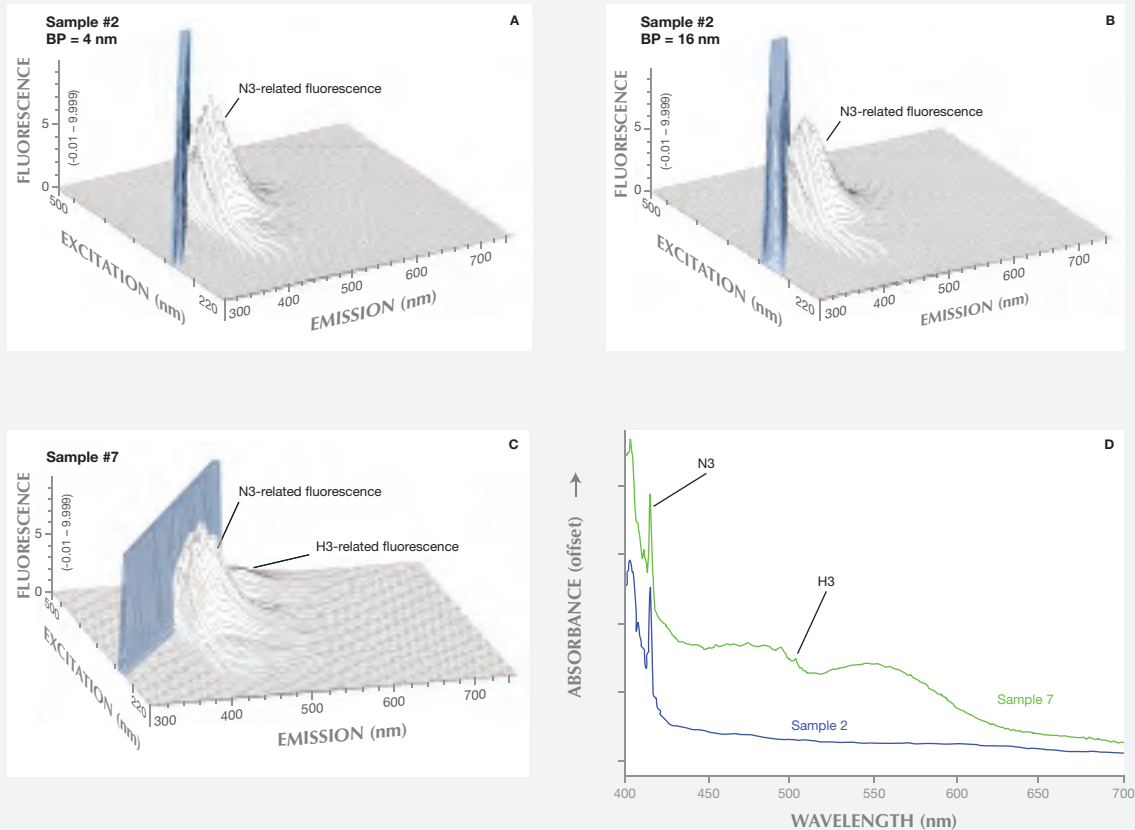
Figure 6. These 3D fluorescence spectra were collected from diamonds with N3 as the major defect center. The top two spectra are from the same sample using different excitation energy peak widths. Sample 7 (bottom left) contains both N3 and H3 centers. UV-Vis-NIR spectra (bottom right) confirm the particular fluorescence defects. Excitation artifacts are marked in blue.

teristic of the N3 center (Eaton-Magaña et al., 2007). The 3D fluorescence spectra indicated that this N3-related emission reaches its maximum at 395 nm excitation energy and is not excited above 430 nm (figure 6). Figures 6A and 6B show fluorescence spectra collected on sample 2 but with different bandpass settings (4 and 16 nm). From these two spectra, it is clear that the bandpass does not affect the position or maximum intensity of N3 fluorescence. Similar results occurred for other defects. Although the bandpass of 16 nm most closely resembles the output of a handheld LWUV light source, the 4 nm bandpass chosen for all the 3D fluorescence spectra in this study adequately represented the corresponding excitation.

Aside from the N3-related emission, which is not active with excitation energy above 435 nm, sample 7 showed a 520 nm emission band with a maximum at 470 nm excitation. This feature is caused by the

H3 center, which was observed from photoluminescence spectra in these three samples but not in the other four from this category. As stated earlier, most diamonds contain multiple color centers.

H3 and H4 Center. The H3 center consists of a vacancy trapped at an A aggregate of nitrogen, which gives an uncharged defect consisting of two nitrogen atoms separated by a vacancy—for instance, $(N-V-N)^0$. Optical absorption at this center has a ZPL at 503 nm and creates a yellow bodycolor in diamond, while also commonly producing green luminescence with visible-light stimulation. The H4 center consists of four nitrogen atoms separated by two vacancies. It is created when a vacancy migrates through the diamond lattice and combines with a B aggregate of nitrogen. This center has a ZPL at 496 nm and typically produces yellow color in diamond. Both H3
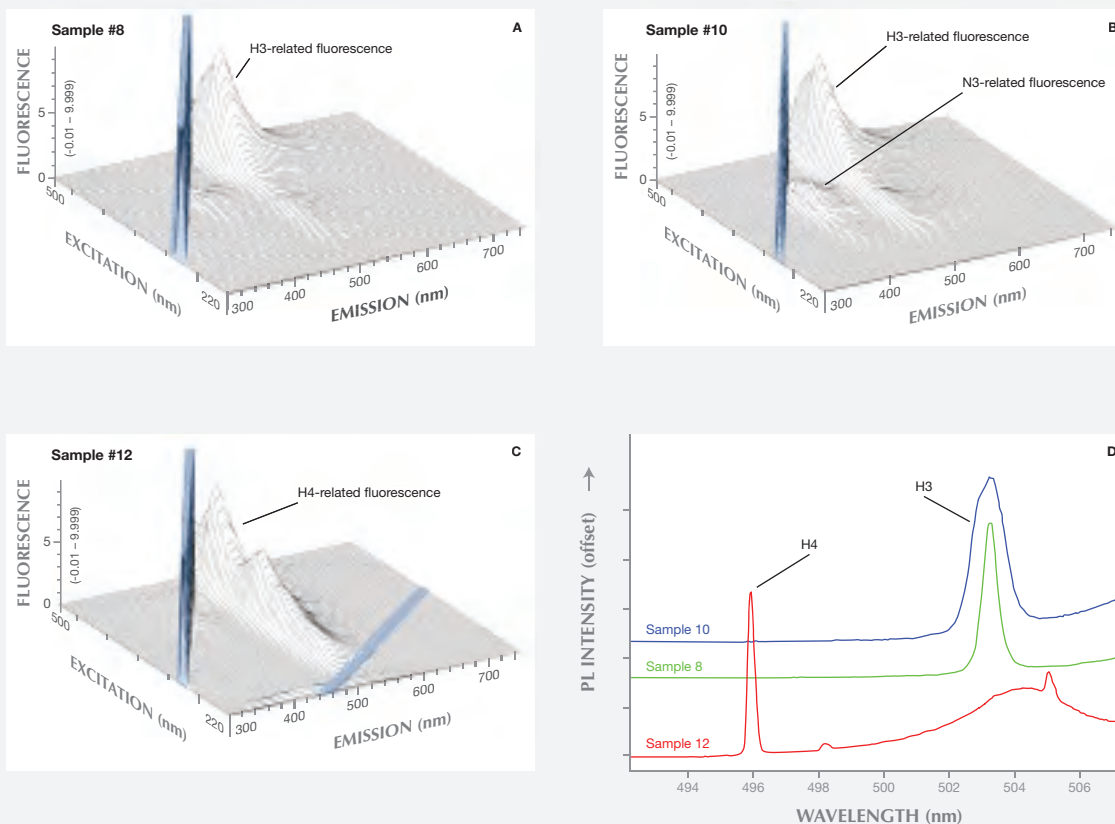
Figure 7. These 3D fluorescence spectra were collected on diamonds with H3 (samples 8 and 10) and H4 (sample 12) as the major defect centers. Both H3 samples also contained weak N3 emissions. In the bottom right corner, PL spectra show the presence of H3 and H4 in the respective samples. Excitation artifacts are marked in blue.

and H4 centers can occur naturally or during treatment (Collins, 1982).

Seven diamonds were examined in this category, including six samples determined by GIA to be naturally colored and dominated by H3 and H4 (three each), as well as one HPHT-treated diamond dominated by H3 (samples 8–14; figure 5). Sample 8 is a Fancy Light greenish yellow stone that fluoresced strong yellow under LWUV and medium yellow under SWUV. Samples 9, 10, and 11 all have some combination of yellow and green bodycolors and exhibited an uneven fluorescence with blue and yellow zones. Samples 12, 13, and 14 have yellowish green bodycolors and showed very strong green fluorescence under both long- and short-wave UV.

Absorption and PL Spectroscopy. UV-Vis-NIR spectra showed the H3-related ZPL at 503 nm for samples

8, 9, 10, and 11, as well as ZPL at 415 nm from the N3 center. The H3 defect requires the presence of aggregated nitrogen, making the occurrence of N3 in such stones very likely. Samples 12, 13, and 14 showed H4-related ZPL at 496 nm in the UV-Vis-NIR spectra. FTIR analysis identified sample 8 as type IaA diamond, and samples 9, 10, and 11 as type Ia with both A and B aggregates in various concentrations. Samples 12, 13, and 14 are type IaB diamonds. Strong 503 nm peaks for samples 8, 9, 10, and 11 and 496 nm peaks for samples 12, 13, and 14 in the PL spectra further confirmed the presence of dominant H3 and H4 centers, respectively (figure 7D).

Fluorescence Spectroscopy. The 3D fluorescence spectra of samples 8–11 show an emission maximum at 520 nm with a wide band extending from ~480 to 650 nm, a feature that manifested itself as a green or

yellowish green fluorescence (figures 7A and 7B). This emission feature is caused by H3 and has a maximum at 470 nm excitation. Unlike N3, the 503 nm ZPL of H3 is not seen at room temperature. The N3-related fluorescence feature was also observed with various intensities due to different defect concentrations (figure 7B). The spectrum for 365 nm excitation, which most closely approximates the LWUV lamp, showed both H3 and N3 emissions at relatively low intensity. Fluorescence spectra from the HPHT-treated sample (11) were not noticeably different from those of other H3-dominated natural-colored samples.

The 3D fluorescence spectra of samples 12–14 (see sample 12 in figure 7C) showed an emission peak centered at 512 nm with a band from ~470 to 630 nm that resulted in green color from H4 fluorescence. This emission feature increases at 395 nm excitation and maximizes at 470 nm. Similar to H3, the ZPL for H4 (496 nm) is not visible at room temperature but was clearly seen in liquid nitrogen–cooled PL spectra for these samples.

Both H3- and H4-related fluorescence emissions showed a broad fluorescence band at ~470 to 650 nm. But the H3 fluorescence peak is shifted to the higher-wavelength side and has a wider tail toward this direction, resulting in a yellowish fluorescence rather than the green fluorescence of H4 (figure 8).

480 nm Band. Although the structure of the 480 nm band is not understood, it is known to be associated with yellow fluorescence in diamond. Six diamonds with 480 nm bands in the UV-visible absorption spectra were examined (samples 15–20; figures 5 and 9). Four of the samples were naturally colored, and two were HPHT-treated. Samples 15–19 had a combination of orange and yellow in bodycolor and fluoresced strong yellow to orange and medium yellow to orange under long- and shortwave UV lamps, respectively. Sample 16 had a brownish color component as well. Sample 20 had yellow bodycolor and showed strong orange and medium orange fluorescence under long- and shortwave UV, respectively.

Absorption and PL Spectroscopy. UV-Vis-NIR spectra showed the typical 480 nm absorption band for all six samples (figure 9D). FTIR analysis identified all of them as type IaA diamonds with traces of isolated nitrogen. Sample 18 contained much higher concentrations of aggregated nitrogen impurities than the other samples. PL spectra at 514 nm excitation showed a
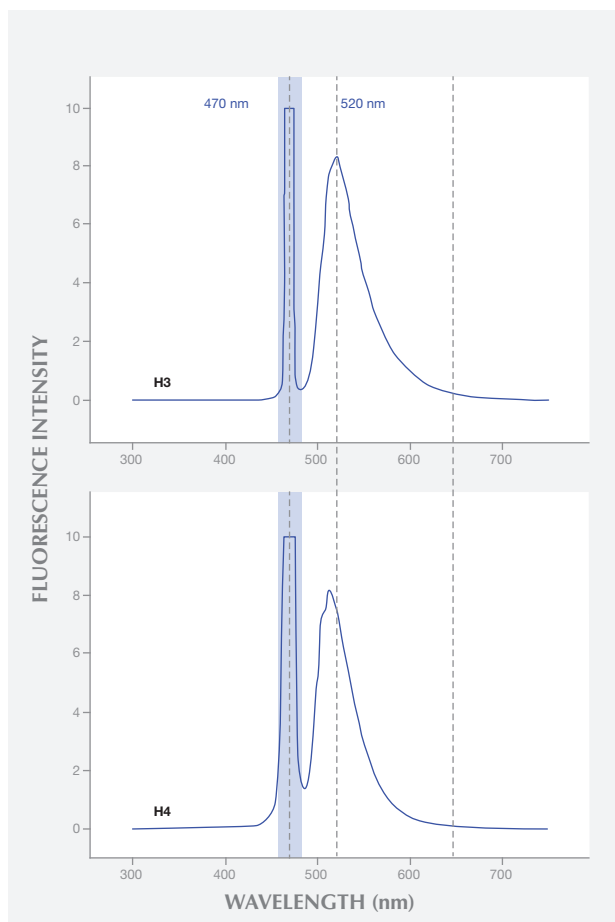
Figure 8. Fluorescence spectra collected at 470 nm excitation from H3 (top, sample 8) and H4 centers (bottom, sample 12) using the ABII luminescence spectrometer show distinct differences in emission peak position and distribution (represented by dashed lines). Excitation artifacts are marked in blue.

wide band from 600 nm to more than 850 nm, typical of diamond with 480 nm bands.

Fluorescence Spectroscopy. 3D fluorescence spectra from 480 nm-band diamonds are complex. All of the samples showed two major features: (1) a wide band centered at ~653 nm (maximum shifts between 630 and 655 nm) that maximized with 485 nm excitation energy, and (2) a ~539 nm-band (maximum shifts between 505 and 541 nm) that increased with 420, 345, and 285 nm excitation energies (figure 9, A–C). The combination of both bands ranged from ~500 to 700 nm and produced yellow to orange fluorescence when excited by visible light (near-LWUV). The band in the red part of the spectrum (630–655 nm) could be excited independently of the ~539 nm band using longer-wavelength light. The fluorescence from this

480 nm BAND
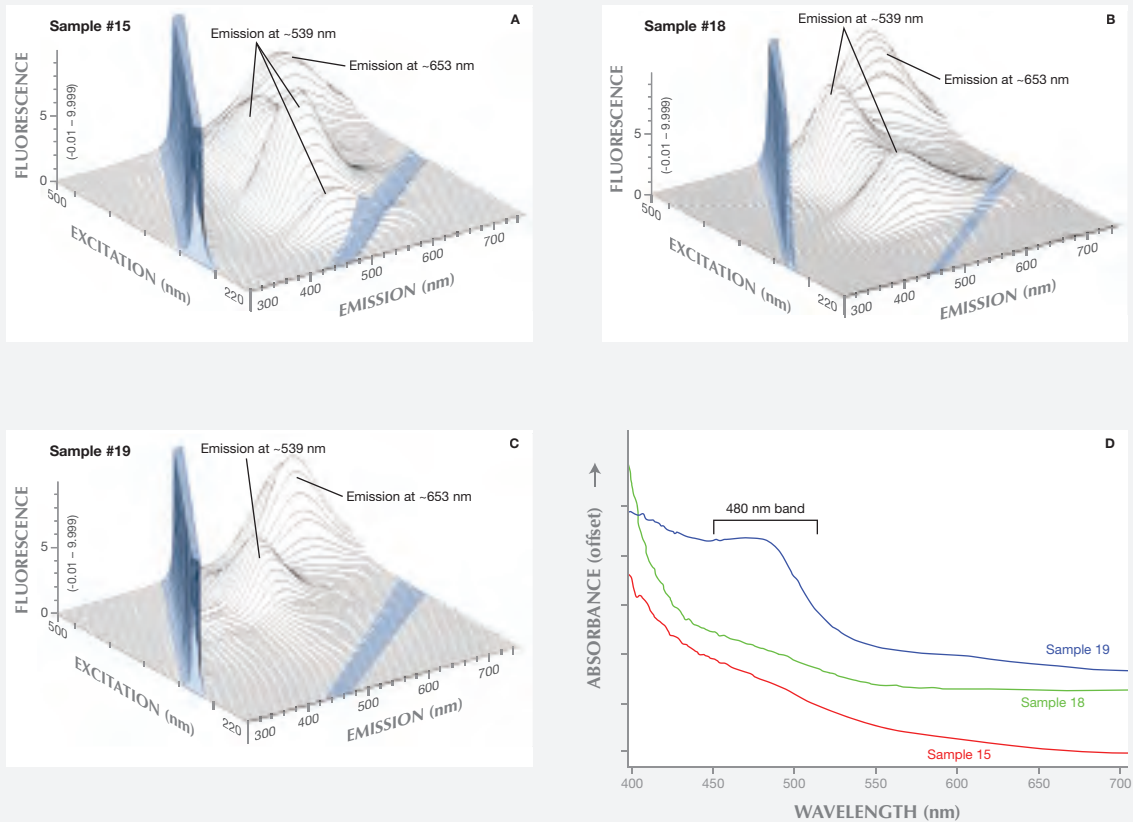
Figure 9. These 3D fluorescence spectra collected on diamonds with 480 nm visible absorption bands as the major defect center vary considerably. In the bottom right corner, UV-Vis-NIR spectra show differences in the shape and intensity of the 480 nm bands. Excitation artifacts are marked in blue.

feature is likely the same as the PL broadband seen after excitation with a 514 nm laser. In general, the band's intensity increased with the size of the 480 nm absorption band. No clear correlations explain the differences in the ~539 nm band. The two HPHT-treated samples showed no obvious systematic differences from the naturally colored samples.

**N-V Center.** The N-V center consists of a single nitrogen atom adjacent to a vacancy in the diamond lattice. The center can exist in an uncharged state, $(N-V)^0$ with ZPL at 575 nm, or in a negative charge state, $(N-V)^-$ with ZPL at 637 nm. N-V defects are commonly associated with orange and red fluorescence (Collins, 1982).

We examined five diamonds with N-V centers (samples 21–25; figures 5 and 10): two naturally colored, two multi-treated, and one irradiation-treated. Samples 21 and 22 were brownish pink and very light

pinkish brown natural-color diamonds that showed weak orange to red fluorescence under both long- and short-wave UV lamps. Samples 23–25 were red and deep pink diamonds that had undergone combination treatments (HPHT + irradiation + annealing; samples 23–24) or standard irradiation + annealing treatment (sample 25). The treated diamonds exhibited red fluorescence under both LWUV and SWUV lights.

Absorption and PL Spectroscopy. The UV-Vis-NIR spectra of samples 21 and 22 featured a broad 550 nm band (thought to be caused by plastic deformation) that contributed to their pink color, as well as the $(N-V)^-$ center at 637 nm. FTIR indicated type IIa stones with no measureable nitrogen or hydrogen impurities. PL spectra showed evidence for significant concentrations of $(N-V)^0$, H3, and $(N-V)^-$ defects (figure 10D). For samples 23 and 24, UV-Vis spectra indicated
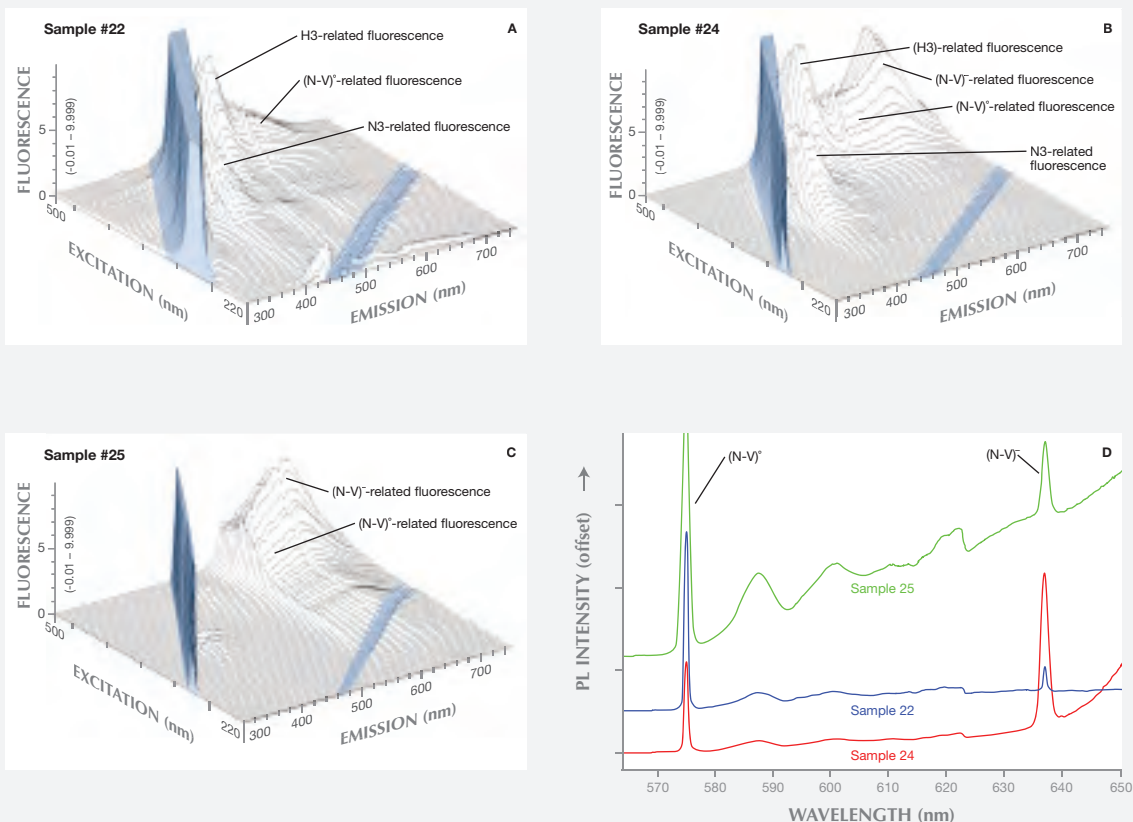
Figure 10. These 3D fluorescence spectra collected on diamonds with N-V centers show combinations of several defect centers. In the bottom right corner, PL spectra from corresponding samples confirm the presence of N-V centers. Excitation artifacts are marked in blue.

an abundance of (N-V)⁻ centers; FTIR identified them as type IaAB with traces of isolated nitrogen. PL spectra showed both $(N-V)^0$ and $(N-V)^-$ centers as well as H3 defects. For sample 25, UV-Vis spectra indicated the presence of a strong $(N-V)^-$ center and FTIR demonstrated a low concentration of type Ib isolated nitrogen defects. PL spectra showed both $(N-V)^0$ and $(N-V)^-$ centers, together with H3 centers.

Fluorescence Spectroscopy. The 3D fluorescence spectra for most of the N-V center samples are complicated by multiple fluorescence-producing defects, sometimes as many as three. Both naturally colored samples (21 and 22; figure 10A) showed the fluorescence emission feature of the $(N-V)^0$ center, with ZPL at 575 nm and an emission band extending from 575 to more than 700 nm with peaks at 586, 600, and 618 nm. We also saw clear fluorescence from two defects: N3 (triplet peaks at 410–450 nm) and H3 (a 520 nm

peak that maximized at 470 nm excitation). Despite its presence in PL spectra, fluorescence from $(N-V)^-$ was not observed in these samples. Sample 21 also displayed fluorescence of unknown origin at ~340–360 nm. The treated samples (23–25) contained both the $(N-V)^0$ and $(N-V)^-$ centers as overlapping bands, with the latter fluorescence band dominating at 660 nm and extending beyond 750 nm (figures 10B and 10C). Sample 25 (figure 10C) featured only N-V defects in the fluorescence spectrum, consistent with the occurrence of mainly isolated nitrogen impurities (type Ib). Samples 23 and 24 contain aggregated nitrogen impurities and, as expected, showed fluorescence from N3 and H3 color centers.

DISCUSSION

UV Light Sources. Emissions from the widely used mercury-based UV lamps (GIA and UVP Mineralight lamps) do not contain pure 365 nm LWUV and

254 nm SWUV peaks, but instead show multiple excitation energies of widely varying bandwidths. Similarly, the popular LED UV loupe has a visible emission of 405 nm, rather than the standard for LWUV (365 nm). The emissions from GIA's LED fluorescence meter and commercial LED light sources show a well-constrained LWUV emission in the 364–367 nm range. The variability in excitation wavelengths and bandwidths among commonly used lamps and LED UV sources demonstrates that the colors and intensities of observed fluorescence in a single sample can vary depending on the light source. UV lamp emissions tend to fluctuate according to the age of the bulbs and filters as well as warm-up times, making it very difficult to achieve consistent results from one source to another. LED sources are far more constrained in emission bandwidth and purity, but they are manufactured in such a wide range of wavelengths that consistency among different products remains a problem. Nevertheless, the well-controlled emissions suggest that LEDs can provide better accuracy and consistency in interpreting the fluorescence response to a LWUV source, as long as an LED near 365 nm is used.

Fluorescence Colors from Different Defect Centers. 3D fluorescence spectra provide an excellent opportunity to examine fluorescence produced by individual defects as well as the contributions of multiple defects. By directly depicting the relationship between UV excitation and fluorescence emission, these spectra illustrate the emission resulting from the various optical centers. Fluorescence spectra from diamonds dominated by individual color centers are relatively simple and consistent, as discussed for each defect in the Results section.

In most diamonds, multiple defect centers occur together. Even under pure 365 nm LWUV excitation, the fluorescence color will be a mixture of the fluorescence from different defect centers. The fluorescence may also have uneven zoning due to defect distributions. Visual observation alone is not an adequate basis for interpreting a diamond's fluorescence color with respect to the corresponding defect centers. The energy of the excitation source can have a profound effect on the resulting fluorescence color and luminescence spectra, and it must be carefully considered.

Potential Effects of UV Light Sources on Fluorescence Color and Intensity. Analysis clearly shows that LWUV sources emit not only varying intensities and bandwidths of light at 365 nm, but also "extra"

peaks resulting from mercury lamps and leaking filters. Our 3D fluorescence spectra demonstrate that small changes in excitation wavelength, even from a "pure" LWUV emission, can significantly affect the intensity and possibly the color of the fluorescence. For example, the intensity of N3 luminescence (measured at 439 nm) when excited by 400 nm excitation is approximately double that of the same emission measured at 360 nm excitation (figure 6). The mixture of the emission peaks from the UV lamp will affect the apparent color and intensity of the fluorescence, limiting the effectiveness and consistency of visual observation.

To illustrate the potential variations introduced by "extra" excitation energy, figure 11A shows the fluorescence emission peaks from sample 15 (extracted from the 3D fluorescence spectra of this sample containing the 480 nm band) at 365, 405, and 435 nm excitation energies. These are the three emission peaks measured from the GIA LWUV lamp (365 nm being the strongest). The spectra were processed to produce equivalent colors by conversion to equivalent CIE L*a*b* color values using GRAMS AI software (including artifact removal, 2° viewing angle, and CIE D65 illumination; all spectral intensities were scaled up 30× to facilitate color reproduction). The fluorescence peak generated by 365 nm excitation is centered at 520 nm, producing a green color with a slightly yellow tint, whereas the fluorescence peaks caused by 405 and 435 nm excitation energies are shifted up to ~545 nm with a tail extending beyond 750 nm, adding an orange-red component to the yellowish green fluorescence. The strong yellow fluorescence of this diamond under the conventional gemological UV lamp is a mixture of the three emission colors from these LW-UV excitation peaks. Under a "pure" 365 nm LED source, this diamond shows a yellowish green fluorescence. While it would be ideal to illustrate this effect with photos, we could not achieve a long enough exposure to photograph the fluorescence.

These multiple emission peaks from the handheld UV lamp can also affect the intensity of the fluorescence color observed. Figure 11B shows the fluorescence emission peaks from sample 7 (extracted from the 3D fluorescence spectra of its N3 center) at the same 365, 405, and 435 nm excitation energies used in the example above. Compared to 365 nm excitation, the fluorescence color with 405 nm excitation is almost twice as intense. The 435 nm excitation gives a relatively small emission peak
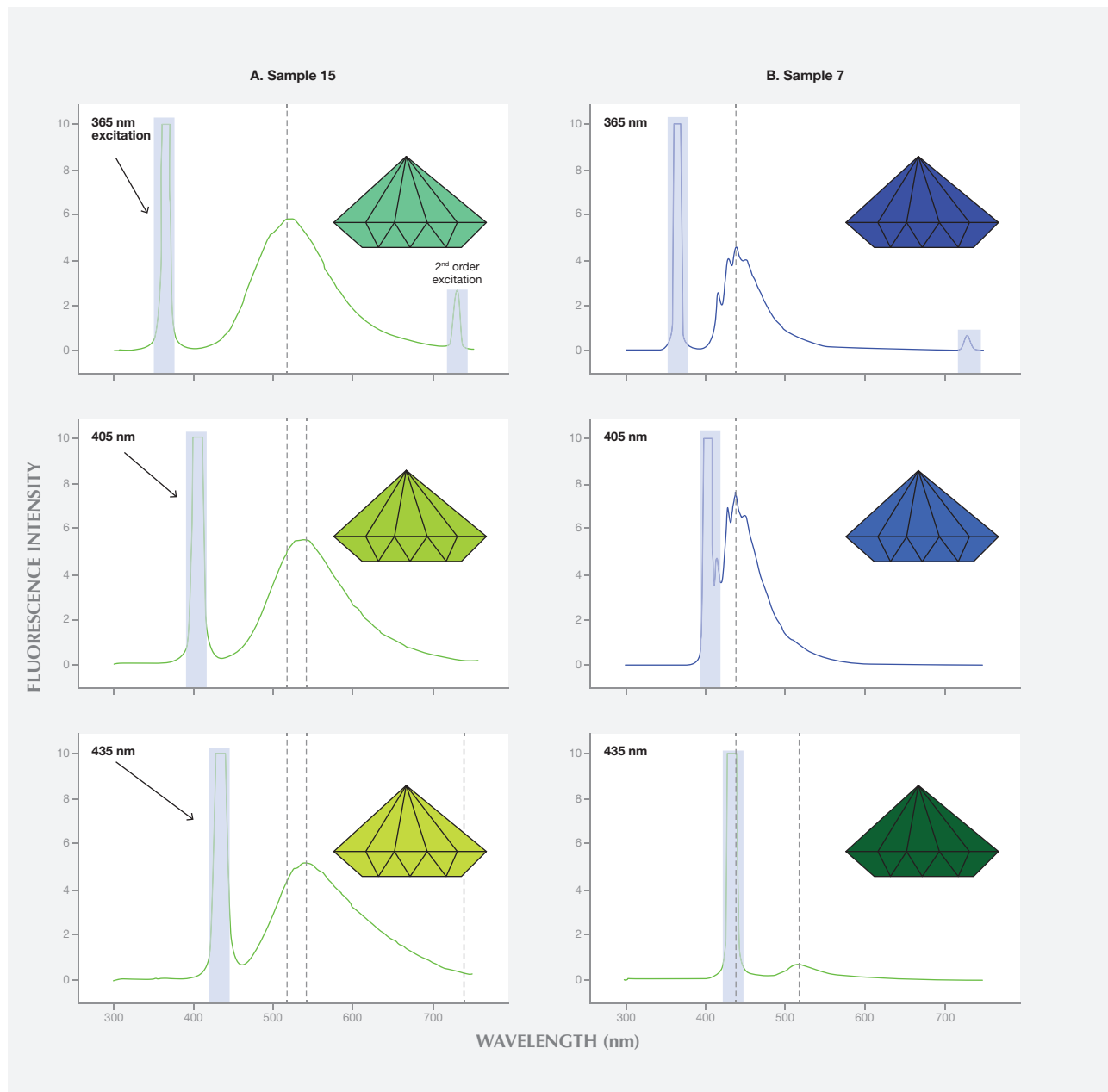
Figure 11. A comparison of diamond fluorescence color (samples 7 and 15) from a conventional UV lamp and a single 365 nm excitation shows the effect of multiple emissions on the color and intensity of diamond fluorescence. Colors were reproduced from spectra by conversion to equivalent CIE L*a*b* values with CIE D55 illumination using Thermo GRAMS AI software. Excitation artifacts are marked in blue.

centered at ~520 nm due to the presence of the H3 center, resulting in a weak green color. "Extra" emission from the conventional UV lamp at 405 nm causes the diamond's blue fluorescence to be more intense than that from a "pure" 365 nm LED source. Such discrepancies contribute to problems with consistency and reproducibility of fluorescence observations within the industry.

Fluorescence as a Tool for Identifying Treatment. Although we tested a limited number of samples, some differences in the fluorescence behavior of natural and treated diamonds were observed. In diamonds with H3 or 480 nm band defects, 3D fluorescence spectra did not show significant differences between the natural-color and treated samples. Yet treated diamonds tended to show much more fluorescence

from the (N-V)⁻ center, partially overlapping with the band from the (N-V)⁰ center, whereas naturally colored stones showed a dominant (N-V)⁰ defect (again, see figure 10). Because the fluorescence from the (N-V)⁻ center was much more intense in the treated diamonds and shifted to longer wavelengths of >750 nm, the fluorescence color from the treated diamonds with both N-V centers was a more intense red color than in the untreated samples with only the (N-V)⁰ center, which produced an orange color. While this trend for N-V centers after HPHT treatment is well documented (e.g., Fisher and Spits, 2000) and also proved true in this study, gemologists should not rely solely on the observation of orange or red fluorescence to ascertain diamond treatment.

CONCLUDING REMARKS

Testing of diamonds with various primary defect centers has shown that to define their fluorescence characteristics, a UV source with consistent output energy is necessary. Traditional gemological UV lamps and light sources used in the diamond industry produce widely variable emissions, making it difficult to achieve reproducible fluorescence observations. LED light sources can provide narrow, well constrained UV emissions to produce more reliable diamond fluorescence reactions.

This study characterizes the fluorescence generated by the most common defect centers in diamond. Changes in fluorescence relative to excitation energy were carefully examined to determine where fluorescence maxima occur for each defect, as well as the peak positions and band shapes that can impact fluorescence colors and intensities. Our findings demonstrate the diamond industry's need for a standardized UV excitation source, to provide consistent and reproducible determinations of fluorescence.

ABOUT THE AUTHORS
Dr. Luo (yun.luo@gia.edu) is supervisor of global metrology and Dr. Breeding is a research scientist at GIA in Carlsbad.

REFERENCES

Becquerel M.E. (1868) *Sources de Lumière: Ses Causes et Ses Effets [Sources of Light: Its Causes and Effects]*. Librairie de Firmin Didot Frères, Paris, 431 pp.

Breeding C.M., Shigley J.E. (2009) The "type" classification system of diamonds and its importance in gemology. *G&G*, Vol. 45, No. 2, pp. 96–111, http://dx.doi.org/10.5741/GEMS.45.2.96.

Collins A.T. (1982) Colour centers in diamond. *The Journal of Gemmology*, Vol. 18, No. 1, pp. 37–75.

——— (1974) Visible luminescence from diamond. *Industrial Diamond Review*, Vol. 34, pp. 131–137.

Cotty W.F. (1956) Identification of diamonds by their fluorescence. *The Journal of Gemmology*, Vol. 5, No. 7, pp. 339–341.

Dyer H.B., Matthews I.G. (1958) The fluorescence of diamond. *Proceedings of the Royal Society of London: Series A, Mathematical and Physical Sciences*, Vol. 243, No. 1234, pp. 320–335, http://dx.doi.org/10.1098/rspa.1958.0002.

Eaton-Magaña S., Post J.E., Heaney P.J., Walters R.A., Breeding C.M., Butler J.E. (2007) Fluorescence spectra of colored diamonds using a rapid, mobile spectrometer. *G&G*, Vol. 43, No. 4, pp. 332–351, http://dx.doi.org/10.5741/GEMS.43.4.332.

Fisher D., Spits R.A. (2000) Spectroscopic evidence of GE POL HPHT-treated natural type IIa diamonds. *G&G*, Vol. 36, No. 1, pp. 42–49, http://dx.doi.org/10.5741/GEMS.36.1.42.

Fritsch E., Waychunas G.A. (1994) Gemstones. In M. Robbins, Ed., *Fluorescence: Gems and Minerals Under Ultraviolet Light*, Geoscience Press Inc., Phoenix, AZ.

Holloway G. (2009) Blue fluorescence in diamond. *The Australian Gemmologist*, Vol. 23, No. 9, pp. 408–414.

Hoover D.B., Theisen A.F. (1993) Fluorescence excitation-emission spectra of chromium-containing gems: An explanation for the effectiveness of the crossed filter method. *The Australian Gemmologist*, Vol. 18, No. 6, pp. 182–187.

Mani A. (1944) The fluorescence and absorption spectra of diamond in the visible region. *Proceedings of the Indian Academy of Sciences A*, Vol. 19, pp. 231–252.

Moses T.M., Reinitz I.M., Johnson M.L., King J.M., Shigley J.E. (1997) A contribution to understanding the effect of blue fluorescence on the appearance of diamonds. *G&G*, Vol. 33, No. 4, pp. 244–259, http://dx.doi.org/10.5741/GEMS.33.4.244.

Pearson G. (2011) Review of ultraviolet sources for gem fluorescence and testing. *The Journal of Gemmology*, Vol. 32, No. 5-8, pp. 211–222.

Shigley J.E., Breeding C.M. (2013) Optical defects in diamond: A quick reference chart. *G&G*, Vol. 49, No. 2, pp. 107–111, http://dx.doi.org/10.5741/GEMS.49. 107.

Shipley R.M. (1947) Notes on the abundance and color of fluorescent diamonds. *G&G*, Vol. 5, No. 9, pp. 395–397.

Wild G.O., Biegel H. (1947) The fluorescence of diamonds. *The Gemmologist*, Vol. 16, No. 193, pp. 228–229.

Williams B. (2007) Technology update—ultraviolet light. *Gem Market News*, Vol. 26, No. 1, pp. 8–11.

NEPHRITE JADE FROM VAL MALENCO, ITALY: REVIEW AND UPDATE

Ilaria Adamo and Rosangela Bocchio

Alpe Mastabia, in the Val Malenco district of northern Italy, has been a source of nephrite jade since the early 2000s. Twenty-one samples from this locality were investigated by classical gemological methods; X-ray powder diffraction, combined with quantitative phase analysis; scanning electron microscopy in combination with energy-dispersive spectrometry; electron microprobe analysis; mass spectrometry; and mid-infrared spectroscopy. From a mineralogical standpoint, this jade consists mainly of tremolite amphibole, with variable amounts of other constituents, especially calcite (up to approximately 30 wt.%), but also pyroxene, apatite, and sulfide minerals. Its pale green color is related to the low iron content of the tremolite amphibole, whereas the other minerals are responsible for different colors (calcite for white, molybdenite and galena for gray). On the basis of minor and trace-element composition, we can classify this jade as dolomite-related nephrite (para-nephrite). Although new material could be recovered from this area, future production will probably be limited by access difficulties.

Nephrite jade is an almost monomineralic rock, composed primarily of tremolite $[Ca_2Mg_5Si_8O_{22}(OH)_2]$ to actinolite $[Ca_2(Mg,Fe)_5Si_8O_{22}(OH)_2]$ amphiboles (Leake et al., 1997). Although tremolite-actinolite is considered the predominant phase in nephrite jade, its specific weight percentage range is still debatable.

Major sources include the Kunlun Mountains in Qinghai Province and the Xinjiang Uygur Autonomous Region of China; the East Sayan Mountains of Siberia; Chuncheon in South Korea; South Westland in the South Island of New Zealand; and Cowell, Australia (Harlow and Sorensen, 2005; Liu et al., 2011a,b; Zhang et al., 2011).

A new deposit of gem-quality nephrite jade (figure 1) was discovered at the beginning of the 2000s at Alpe Mastabia, located in the Val Malenco district in the Sondrio province of northern Italy (figure 2). Mr. Pietro Nana first noticed an attractive green stone in the discarded waste materials of an abandoned talc mine (figure 3) located at an altitude of 2,077 meters (Nichol and Geiss, 2005). The events leading to the discovery of the Alpe Mastabia nephrite as well as the geologic environment bear striking similarities to those reported by Dietrich and De Quervain (1968) for the better-known nephrite deposit at Scortaseo (Val Poschiavo, Switzerland), situated less than 20 km away.

Figure 1. Nephrite jade from Val Malenco is used in gems and ornamental carvings, such as these bird statuettes (approximately 15 cm high). Courtesy of Pietro Nana.
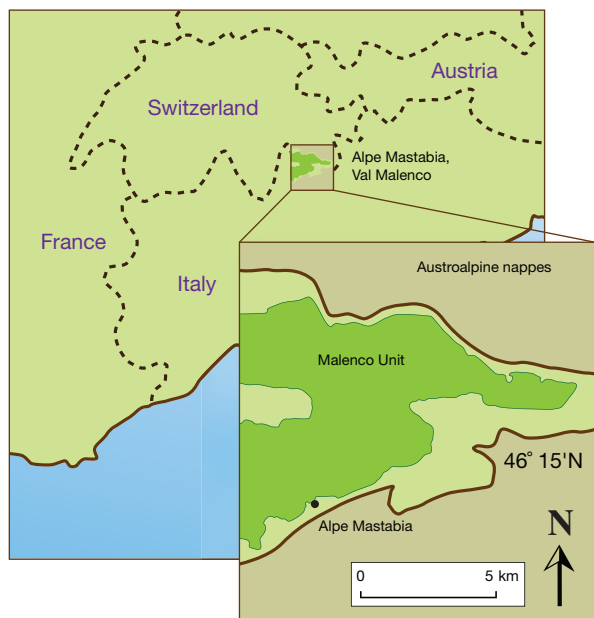
Figure 2. Alpe Mastabia in Val Malenco, northern Italy, has been producing gem-quality nephrite jade since the beginning of the 2000s. The inset shows the area's main geologic features. The Alpe Mastabia talc/nephrite deposit is enclosed in schists, gneiss, and marbles.

This study aims to provide a review and update of the nephrite jade from Val Malenco, by investigating a suite of rough and cut gem-quality samples using X-ray powder diffraction combined with quantitative phase analysis based on the Rietveld method; scanning electron microscopy in combination with energy-dispersive spectrometry (SEM-EDS); electron microprobe analysis in wavelength dispersion mode (EMPA-WDS); mass spectrometry; and mid-infrared (IR) spectroscopy.

GEOLOGIC SETTING

Val Malenco is an extremely interesting geological and mineralogical district (Adamo et al., 2009) situated in the Rhetic Alps near the Italian-Swiss border between the Southern Alps and the so-called "root zone" of the Alpine nappes. The main geological unit is an ultra-mafic body (the "Malenco unit") that is one of the largest ophiolitic masses of the Alps (figure 2). It is exposed in an area of about 130 km^2 and consists of serpentinized peridotite with minor relics of lherzolite and harzburgite (Trommsdorff et al., 1993). The Alpe Mastabia talc mine is situated in a narrow tectonic zone (Lanzada-Scermendone) at the southern margin of the Malenco unit (figure 2). About 300 meters away is serpentinized rock, and the rocks around the talc mine are orthogneisses and schists (see box A) of the pre-Mesozoic crystalline basement, situated among Triassic white calcitic to dolomitic marbles. The origin of the talc deposit, as well as of tremolite and nephrite, is ascribed to metasomatic processes within

Figure 3. Left: A view of the Alpe Mastabia talc mine with the nephrite deposit. Right: Pietro Nana stands near the entrance. Courtesy of Pietro Nana and Vincenzo De Michele.

Nappe: A large body or sheet of rock that has shifted far from its original position by thrust faulting during continental collisions. Also known as an *allochton*.

Ultramafic (or ultrabasic): Describing igneous and meta-igneous rocks with very low silica content (less than 45% SiO_2), generally greater than 18% MgO, high FeO, and low potassium. Ultramafic rocks are usually composed of greater than 90% mafic minerals, which are dark and have high magnesium and iron contents.

Peridotite: Coarse-grained ultramafic rock consisting mainly of olivine (at least 40% by volume) and pyroxene (ortho-/clino-). Peridotites are distinguished according to their different mineralogical composition. *Dunite* contains more than 90% olivine. *Wherlite* is mostly composed of olivine (40–90%), clinopyroxene, and a minor amount of orthopyroxene (<10%). *Lherzolite* contains olivine (40–90%) and approximately equal amounts of clinopyroxene and orthopyroxene. *Harzburgite* contains olivine (40–90%), orthopyroxene, and small amounts of clinopyroxene (<10%).

Orthogneiss: Rock derived from the metamorphism of igneous rocks. Orthogneiss is distinguished from *paragneiss*, which derives from sedimentary rocks.

Schist: Metamorphic rock having a foliated or plated structure called *schistosity*, in which the flaky minerals (micas) are visible to the eye.

Metasomatic: Referring to a process by which the chemical composition of a rock or portion of rock is altered in a pervasive manner. Metasomatism involves the introduction or removal of chemical components as a result of the rock's interaction with aqueous solutions. During metasomatism, the rock remains in a solid state.

---

the dolomitic marbles during the Alpine metamorphism (Montrasio, 1984; Nichol and Giess, 2005).

HISTORY AND PRODUCTION

During the years of operation at the Alpe Mastabia talc mine, from 1964 to 1994, nephrite boulders associated with the talc were ignored or discarded as waste (Andreis, 1970; De Michele et al., 2002; Nichol and Giess, 2005). The mine was abandoned, and entrances to its horizontal tunnels and galleries that once led to the ore body have mostly caved in or been barricaded (again, see figure 3), making the deposit difficult to access. In 1995, while examining the waste material outside the mine, Mr. Nana noticed some attractive nephrite boulders. Recognizing their gemological value, he consigned rough samples to lapidary workshops in China and Idar-Oberstein, Germany. The production and marketing of nephrite jade from Alpe Mastabia started at the beginning of the new millennium, with about 25 tons produced since the discovery. Production still flourishes due to the high quality of the finished jewelry pieces and other ornamental objects.

MATERIALS AND METHODS

We examined 21 samples from the Val Malenco deposit, consisting of 13 cut (3.33–25.34 ct; figure 4) and eight rough (0.35–2.50 ct) specimens. All 13 cut samples underwent standard gemological testing to determine their refractive index (RI), specific gravity (SG), and ultraviolet (UV) fluorescence.

X-ray powder diffraction measurements were carried out on six rough specimens to determine the jade's mineralogical composition. Data were collected by means of a Panalytical X'Pert-PROMPD X'Celerator X-ray powder diffractometer, using CuKα radiation (λ=1.518 Å) at a beam voltage of 40

Figure 4. These cut nephrite jades from Val Malenco (3.33–25.34 ct) were investigated in this study. Photo by Monica Odoli.

kV and a current of 40 mA. X-ray powder diffraction patterns were collected over the 9–80° range of the scattering angle 2θ, with steps of 0.02° 2θ and a count time of 25 seconds per step. The phase identification was based on data from the PDF-2 database (International Center for Diffraction Data, Newton Square, Pennsylvania). Quantitative phase analysis (box B) was performed with the Rietveld method using the

In Brief

- Nephrite jade is an almost monomineralic rock, composed mainly of tremolite to actinolite amphiboles.

- The nephrite deposit at Alpe Mastabia, located in northern Italy's Val Malenco district, has been producing nephrite jade since the beginning of the 2000s.

- The nephrite from Val Malenco is associated with dolomitic marbles (para-nephrite).

- This jade's pale green color is due to the low concentration of iron, although other minerals (i.e., calcite, molybdenite, and galena) can also influence the color.

GSAS software package (Larson and Von Dreele, 1994) to treat the experimental 2θ-profile.

The microstructural features of six rough samples were investigated using a Cambridge STEREOSCAN 360 scanning electron microscope (SEM), with an acceleration current of 15 kV. Semi-quantitative chem-

ical analyses were performed using the electron microscope's EDS system (ISIS 300 Oxford).

We also performed quantitative chemical analyses *in situ* of the fibrous crystals constituting the four rough nephrite samples previously analyzed with X-ray powder diffraction. We used a JEOL JXA-8200 electron microprobe in wavelength-dispersive mode (EMPA-WDS) under the following conditions: 15 kV accelerating voltage, 15 nA beam current, and a count time of 60 seconds on peaks and 30 seconds on the background. The following standards were used: natural grossular (for Si and Ca), anorthite (Al), fayalite (Fe), olivine (Mg), rhodonite (Mn), omphacite (Na), ilmenite (Ti), K-feldspar (K), and pure V and Cr for those elements. The raw data were corrected for matrix effects using a conventional ΦρZ routine in the JEOL software package.

The trace-element composition of the same fibrous crystals in four rough samples was determined by laser ablation–inductively coupled plasma–mass spectroscopy (LA-ICP-MS). The instrument consisted of a Quantel Brilliant 266 nm Nd:YAG laser coupled to a Perkin Elmer DRCe quadrupole ICP-MS. The spot size was 40 μm, using NIST SRM 610 glass as an external standard and Ca as an internal standard, as analyzed by microprobe. Precision and accuracy estimated on the basaltic glass standard BCR2 were better than 10%.

Additional information was derived from hydrogen isotope composition, obtained through multiple analyses of a few milligrams of selected tremolite

BOX B: QUANTITATIVE PHASE ANALYSIS

Quantitative phase analysis (QPA) is used to determine the concentration of various phases present in a mixture after the identity of every phase has been established (*qualitative* phase analysis). Powder diffraction is a direct method to identify and quantify phases on the basis of their unique crystal structures (Pecharsky and Zavalij, 2003; Dinnebier and Billinge, 2008).

Among existing QPA methods, the Rietveld (1969) technique appears to be one of the fastest and most reliable. The foundation of the Rietveld method is that the difference between the measured and calculated whole powder diffraction profile should be close to zero by means of the following minimized function (Pecharsky and Zavalij, 2003):

$$\Phi = \sum_{i=1}^{n} w_i \left(Y_i^{obs} - Y_i^{calc} \right)^2$$

where Y_1^{obs} is the observed and Y_1^{calc} is the calculated intensity of a point i of the powder diffraction pattern, and w_i is the weight assigned to the ith data point.

The entire calculated powder diffraction pattern is based on simultaneously refined models of the crystal structures, diffraction optics effects, instrumental factors, and other specimen features. Rietveld refinement of multiphase samples can generate a relatively accurate QPA, because the Rietveld scale factors determined during the refinements for every phase in the mixture are proportional to the weight of the corresponding phases (Pecharsky and Zavalij, 2003; Dinnebier and Billinge, 2008).

TABLE 1. Gemological properties of the 13 cut nephrite jade samples from Val Malenco, Italy, investigated in this study.

	A	B	C	D	E	F	G	H	I	L	M	N	O
Color	Whitish green	Greenish white	White-green	Greenish white	Greenish white	Whitish green	Greenish white	White	White	Greenish white	Yellowish green	Yellowish green	Green
Diaphaneity	Opaque	Opaque	Opaque	Opaque	Opaque	Opaque	Opaque	Opaque	Opaque	Opaque	Opaque	Opaque	Opaque
Refractive index[a]	1.60	1.60	1.60	1.60	1.60	1.60	1.60	1.60	1.60	1.60	1.60	1.60	1.60
Specific gravity	2.95	2.89	2.89	2.89	2.96	2.90	2.86	2.77	2.74	2.85	2.96	2.96	2.96
Mohs hardness	6.5	6.5	6.5	6.5	6.5	6.5	6.5	6.5	6.5	6.5	6.5	6.5	6.5
UV fluorescence	Inert	Inert	Inert	Inert	Inert	Inert	Inert	Inert	Inert	Inert	Inert	Inert	Inert

[a] Measured by the distant vision method

fibers by mass spectrometry following standard procedures (Vennemann and O'Neil, 1993).

Mid-infrared absorption spectroscopy (4000–600 cm^{-1}) was carried out on four rough specimens using a Nicolet Nexus Fourier-transform infrared (FTIR) spectrometer, operating in transmission mode with KBr pellets, at a resolution of 4 cm^{-1} and 200 scans per sample.

RESULTS

Gemological Properties. The gemological properties of the 13 cut jades from Val Malenco are listed in table 1. The color of both the polished and rough samples ranged from a common white and white-green to a rarer yellowish green and green (figure 4). Two rough samples had a blackish gray color (similar to the bracelet's color in figure 11). The RI was constant, while SG ranged from 2.74 to 2.96, with the lower values in the whitest samples. The SG values of the two blackish gray rough samples were 2.80 and 2.86. All the stones were opaque and inert to long- and short-wave UV radiation. Irregular striped or spotted color zoning was observed in nearly every sample.
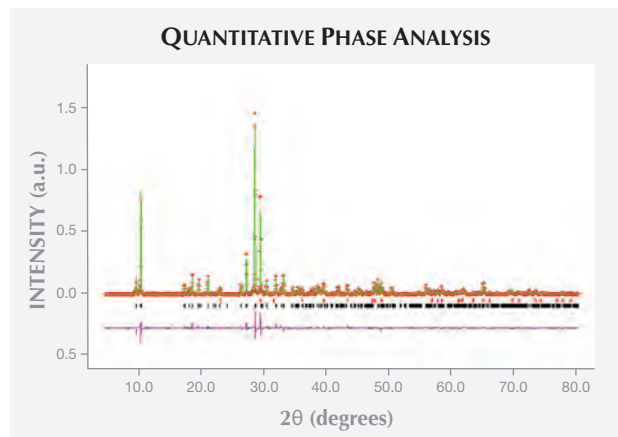
X-ray Powder Diffraction Data. Quantitative phase analysis based on XRPD data showed that five specimens consisted mainly of tremolite amphibole, with various amounts of other minerals, especially calcite. This mineral was generally less than 5 wt.%, though exceptional values of about 25–30 wt.% were found in the two most whitish samples (table 2; figure 5).

Microstructure. The nephrite jade from Val Malenco showed a micro- to crypto-crystalline texture that consisted of a dense intergrowth of fine (about 10–20 μm long) randomly oriented bundles of tremolite

Figure 5. Based on Rietveld refinement of the X-ray powder diffraction pattern (9–80° 2θ-angle range) of the white nephrite sample 4C, the main constituent phases are about 70 wt.% tremolite and 30 wt.% calcite (peak positions marked in black and red, respectively). The lower pattern represents the residual between the calculated and experimental curves.

TABLE 2. Mineralogical composition (wt.%) of the six rough nephrite jade samples from Val Malenco.

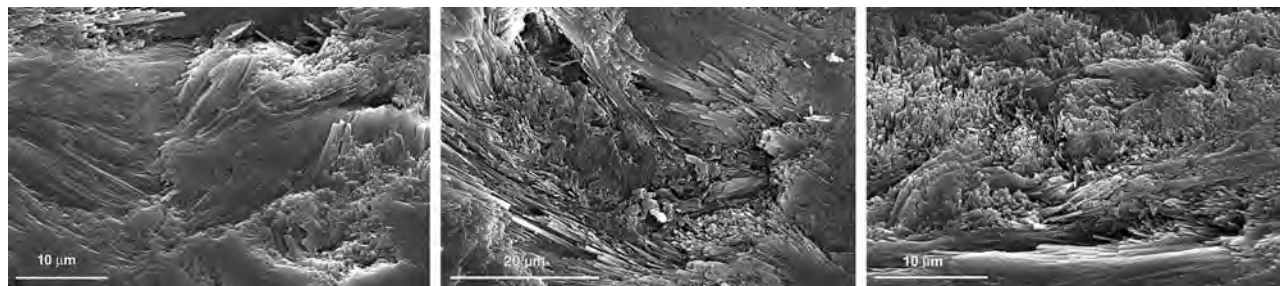| Sample	4S	6A	6B	13	12	4C
Color	Green	Green	White-green	White-green	White	White
Tremolite	100	99	97	95	76	70
Calcite	0	1	3	5	24	30

QUANTITATIVE PHASE ANALYSIS

Figure 6. Nephrite jade from Val Malenco is characterized by a finely fibrous texture, as shown in these SEM photos.

fibers (figure 6). Other minerals were identified by SEM-EDS as calcite, diopside, apatite, and opaque minerals (molybdenum, iron, lead, and zinc sulfides; see figure 7). Calcite was widespread in almost all

Figure 7. SEM photos show the mineralogical composition of the blackish gray (top) and white specimens (bottom). Tremolite is labeled T, calcite C, galena G, and molybdenite M.


samples, whereas the other minerals were rarer. In particular, molybdenite and galena were more concentrated in the blackish gray nephrite samples. These minerals were distributed unevenly in nephrite.
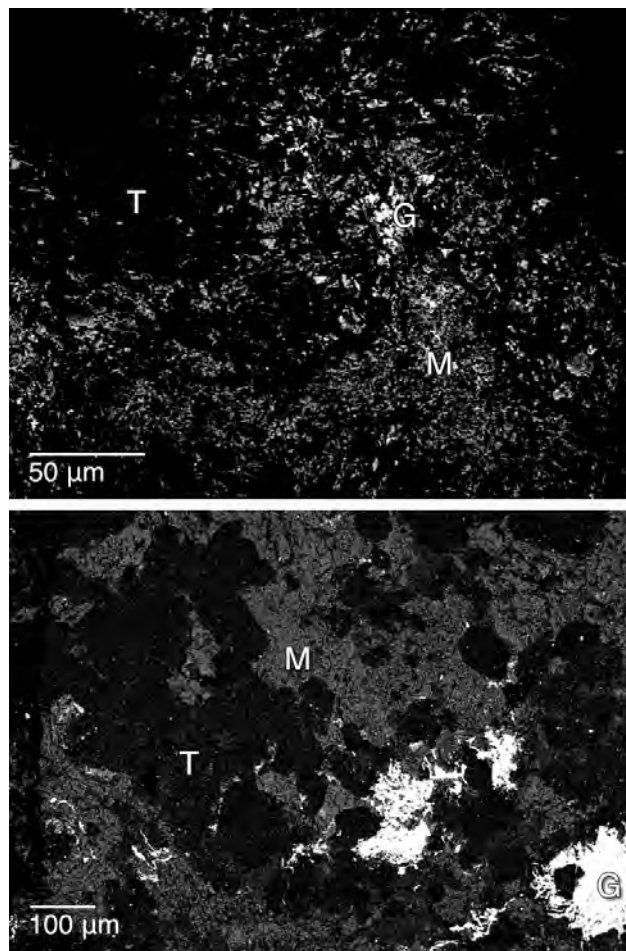
Chemical Composition. The chemical composition of the fibrous crystals in the jade is reported for four samples in table 3.

Chemical analyses of the fibrous mineral showed a composition close to that of tremolite amphibole, $Ca_2Mg_5Si_8O_{22}(OH)_2$, according to the classification of Leake et al. (1997), with a low concentration of most trace elements. All elements of the first transition series (Sc, Ti, V, Cr, Mn, Fe, Co, Ni, Cu, and Zn), as well as the alkaline earth metals (Sr, Ba), and alkaline metals (K, Rb, Cs) were always less than 0.1 wt.%, with the lone exception of Na, ranging from 0.14 to 0.20 wt.% as Na_2O. Among the chromophore ions, iron was the most abundant, with contents ranging from 527 to 670 ppm (as Fe), followed by vanadium at about 200 ppm (as V); chromium was much lower, with concentration ≤4 ppm (as Cr; table 3).

In terms of stable isotopic composition, the

Figure 8. The IR spectrum of the white nephrite sample 4C shows absorption bands of tremolite (labeled T) and calcite (C).
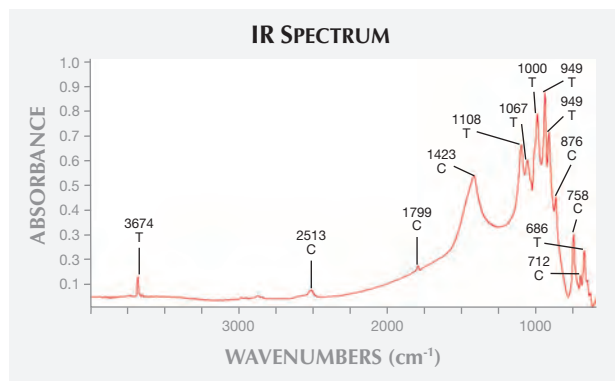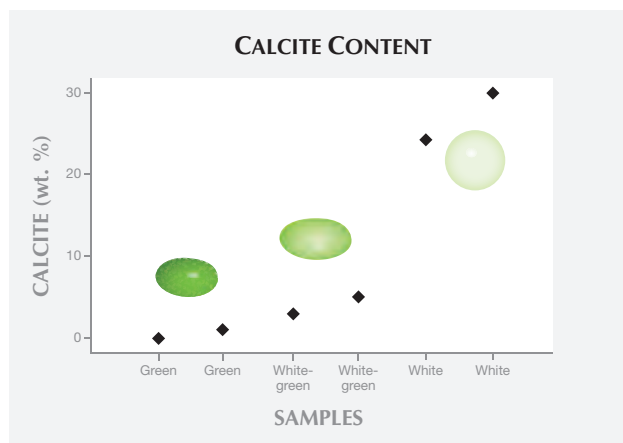
CALCITE CONTENT

Figure 9. Calcite contents obtained by X-ray powder diffraction analyses (see table 2) are shown for six nephrite jade samples.

nephrite samples had a hydrogen isotopic mean value (δD) of -113 ± 4.8‰.

Mid-Infrared Spectroscopy. The samples' mid-IR absorption spectra, collected in transmission mode with KBr pellets (figure 8), were characterized by bands at 3674, 1108, 1067, 1000, 949, 922, 758, and 688 cm^{-1}, typical of tremolite (Hawthorne and Della Ventura, 2007). The whitest samples (12 and 4C) also contained the absorption features of calcite (2513, 1799, 1423, 876, and 712 cm^{-1}; Farmer, 1974).

DISCUSSION

The various samples from Val Malenco exhibited RI values typical for nephrite jade (O'Donoghue, 2006). Their SG values, which showed variation with the color of the stones, were in agreement with those commonly reported for this jade (SG=2.9–3.1; O'Donoghue, 2006), except for the lower values in the two white samples (2.77 and 2.74, respectively; see H and I, table 1). These SG values are compatible with a significant amount of calcite, whose SG (2.70 ± 0.01) is lower than that of tremolite. The Mohs hardness of 6.5 and the finely felted fibrous texture are typical of nephrite from localities worldwide (O'Donoghue, 2006).

The fine fibers of tremolite amphibole occurred together with other unevenly distributed constituents. Calcite was the most abundant, although its content varied from 0 to about 30 wt.%; pyroxene, apatite, and sulfide minerals were rarer. The variable amount of calcite corresponded with a white hue (figure 9), while molybdenite and galena were responsible for the gray and black hues.

Chemical analysis of the tremolite fibers revealed a low abundance of minor and trace elements, with

TABLE 3. Average chemical composition of tremolite amphibole in the nephrite jade from Val Malenco.

Sample	4S	6A	6B	4C
Electron microprobe analyses[a]				
Oxides (wt.%)				
SiO$_2$	59.41	59.87	59.60	58.98
TiO$_2$	0.01	0.02	0.02	0.02
Al$_2$O$_3$	0.26	0.04	0.29	0.48
FeO	0.03	bdl[b]	0.01	0.08
MnO	0.01	0.01	0.01	0.02
MgO	23.14	23.01	23.12	22.89
CaO	13.22	13.16	13.12	13.42
Na$_2$O	0.14	0.15	0.18	0.20
K$_2$O	0.04	0.04	0.05	0.04
Total	96.26	96.31	96.39	96.12
Fe/(Fe+Mg)	0.001	0.000	0.000	0.002
Ions per 23 oxygens				
Si	8.127	8.176	8.137	8.093
Ti	0.001	0.002	0.002	0.002
Al	0.041	0.007	0.046	0.077
Fe	0.003	bdl	0.001	0.009
Mn	0.001	0.001	0.001	0.002
Mg	4.719	4.684	4.705	4.681
Ca	1.937	1.926	1.919	1.972
Na	0.038	0.039	0.047	0.053
K	0.007	0.007	0.008	0.008
LA-ICP-MS analyses[c]				
Element (ppm)				
Sc	1.24	1.42	1.38	1.16
Ti	21.0	12.2	18.7	19.2
V	215	271	293	220
Cr	2.10	2.47	4.20	2.20
Mn	81.2	80.7	84.5	87.8
Fe	584	527	572	670
Co	0.19	0.19	0.29	0.19
Ni	0.46	0.57	0.81	0.66
Zn	52.7	42.0	51.5	38.9
Sr	6.88	7.21	6.46	5.34
Y	0.72	0.68	0.93	0.23
Zr	0.14	0.18	0.39	0.66

[a] *Ten points per sample were analyzed. FeO is the total iron. Cr is below detection limit in all samples.*
[b] *Abbreviation: bdl = below detection limit (0.01 wt.%).*
[c] *Five points per sample were analyzed.*

iron as the most abundant chromophore ion. Yet its content shows comparable values in the various sample colors from white to green (again, see figure 9). This suggests that the occurrence of other mineral phases (e.g., calcite) could influence the jade's color variation.

Nephrite's minor and trace-element chemical composition plays an important role in tracing its geologic origin. It is used to distinguish nephrite associated with dolomitic marbles (dolomite-related
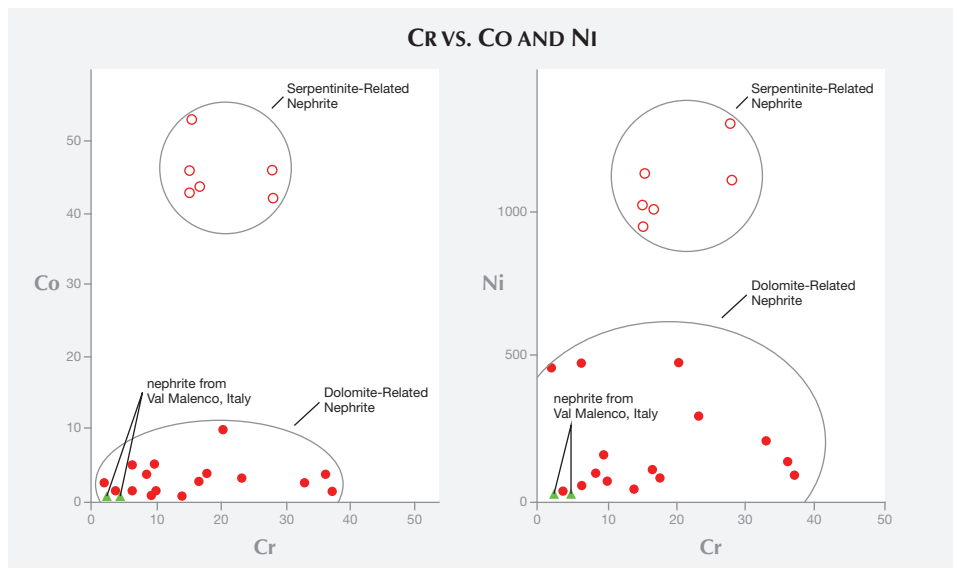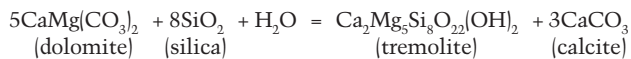
Figure 10. Chromium versus cobalt and nickel plots of the Italian nephrite jade (green triangles) are compared with nephrite data from Siqin et al. (2012).

nephrite or para-nephrite) from that associated with serpentinite rock (serpentinite-related nephrite or ortho-nephrite); see, for instance, Nichol (2000) and Siqin et al. (2012). In particular, various authors (e.g., Siqin et al.) have shown that serpentine- and dolomite-related nephrite minerals can be separated on the basis of their Fe/(Fe+Mg) ratio (0.064–0.118 and 0.001–0.074, respectively) and their concentrations of Cr, Co, and Ni, which are higher in nephrite associated with serpentinite. Based on the very low Fe/(Fe+Mg) ratio (always <0.002), as well as the low contents of Co (0.19–0.29 ppm), Cr (2.10–4.20 ppm), and Ni (0.46–0.81 ppm) found in the nephrite jade from Val Malenco (table 3 and figure 10), we can classify this material as dolomite-related nephrite or para-nephrite.

The possible formation process for this type of nephrite deposit is commonly ascribed to a metasomatic reaction involving dolomite replacement by silicic fluids (Harlow and Sorensen, 2005). This is consistent with the reaction proposed by Nichol and Giess (2005) for nephrite from Val Malenco, which produces excess calcite as isolated grains or aggregates:

$$5CaMg(CO_3)_2 + 8SiO_2 + H_2O = Ca_2Mg_5Si_8O_{22}(OH)_2 + 3CaCO_3$$
(dolomite) (silica)   (tremolite)   (calcite)

Yet the occurrence of diopside grains as rare relicts within tremolite also suggests a second stage of formation involving the intermediate formation of diopside from dolomite, subsequently replaced by tremolite. In any case, the formation of the Alpe Mastabia deposit in Val Malenco implies an intense fluid-rock reaction by hydrothermal solutions, percolating at the contact between the dolomitic marbles and the enclosing schists (Nichol and Giess, 2005). The very low δD-depleted value determined on this nephrite also suggests a possible contamination of the hydrothermal fluid with water of meteoric origin (Yui and Kwon, 2002; Harlow and Sorensen, 2005).

CONCLUSIONS

Nephrite jade from Val Malenco, northern Italy, entered the market at the beginning of the 2000s. Since the discovery of nephrite there in 1995, the deposit has produced about 25 tons of gem-quality rough,

Figure 11. These necklaces (top) and bracelet (bottom) consisting of approximately 10 mm diameter spheres are fashioned from nephrite jade from Val Malenco. Photos by Pietro Nana.

carved into ornamental objects or fashioned into jewelry (figure 11). This study, performed on both cut and rough specimens, shows that nephrite jade from Val Malenco is composed of tremolite amphibole. It contains a low concentration of iron as a chromophore, in agreement with its pale green color. Variable amounts of other constituents also influence the color: Calcite is responsible for the rather common white hue, while molybdenite and galena cause the black and gray colors. The nephrite's compact microstructure and soft color make it an attractive gem material. Although new finds could be limited by access difficulties, the geologic features of the deposit suggest significant potential for further production.

ABOUT THE AUTHORS
Dr. Adamo (ilaria.adamo@unimi.it) is junior researcher, and Dr. Bocchio is professor of mineralogy, in the Earth Sciences department of the Università degli Studi di Milano, Italy.

REFERENCES

Adamo I., Bocchio R., Diella V., Pavese A., Vignola P., Prosperi L., Palanza V. (2009) Demantoid from Val Malenco, Italy: Review and update. *G&G*, Vol. 45, No. 4, pp. 280–287, http://dx.doi.org/10.5741/GEMS.45.4.280.

Andreis C. (1970) Il talco di Mastabia in Val Malenco (Prov. di Sondrio). Master's thesis, Università degli Studi di Milano (Italy).

De Michele V., Liborio G., Nana P., Piacenza B. (2002) Nefrite della Val Malenco (Provincia Sondrio, Lombardia, Italia). *IVM Magazine*, Bollettino dell'Istituto di Mineralogia "F. Grazioli," Vol. 1, pp. 13–15.

Dinnebier R.E., Billinge S.J.L., Eds. (2008) *Powder Diffraction: Theory and Practice*. Royal Society of Chemistry, Cambridge, UK.

Dietrich V., De Quervain F. (1968) Die Nephrit-Talklagerstätte Scortaseo (Puschlav, Kanton Graubünden) [The Scortaseo nephrite-talc deposit (Poschiavo, Grisons Canton)]. *Beiträge zur Geologie der Schweiz, Geotecnische Serie*, Vol. 46.

Farmer V.C. (1974) *The Infrared Spectra of Minerals*. Mineralogical Society, London.

Harlow G.E., Sorensen S.S. (2005) Jade (nephrite and jadeitite) and serpentinite: metasomatic connections. *International Geology Review*, Vol. 47, No. 2, pp. 113–146, http://dx.doi.org/10.2747/0020-6814.47.2.113.

Hawthorne F.C., Della Ventura G. (2007) Short-range order in amphiboles. In Hawthorne F.C., Oberti R., Della Ventura G., Mottana A., Eds., *Amphiboles: Crystal Chemistry, Occurrence and Health Issues*, Reviews in Mineralogy and Geochemistry, Vol. 67, pp. 173–222.

Larson A.C., Von Dreele R.B. (1994) General structure analysis system (GSAS). Los Alamos National Laboratory Report, LAUR 86-748.

Leake B.E., Woolley A.R., Arps C.E.S., Birch W.D., Gilbert M.C., Grice J.D., Hawthorne F.C., Kato A., Kisch H.J., Krivovichev V.G., Linthouut K., Laird J., Mandarino J.A., Maresch W.V., Nickel E.H., Rock N.M.S., Schumacher J.C., Smith D.C., Stephenson N.C.N., Ungaretti L., Whittaker E.J.W., Youzhi G. (1997) Nomenclature of amphiboles: Report of the Subcommittee on Amphiboles of the International Mineralogical Association, Commission on New Minerals and Mineral Names. *American Mineralogist*, Vol. 82, No. 9/10, pp. 1019–1037, http://dx.doi.org/10.1180/minmag.1997.061.405.13.

Liu Y., Deng J., Shi G., Sun X, Yang L. (2011a) Geochemistry and petrogenesis of placer nephrite from Hetian, Xinjiang, Northwest China. *Ore Geology Review*, Vol. 41, No. 1, pp. 122–132, http://dx.doi.org/10.1016/j.oregeorev.2011.07.004.

Liu Y., Deng J., Shi G., Yui T-F., Zhang G., Abuduwayiti M., Yang L., Sun X. (2011b) Geochemistry and petrology of nephrite from Alamas, Xinjiang, China. *Journal of Asian Earth Sciences*, Vol. 42, No. 3, pp. 440–451, http://dx.doi.org/10.1016/j.jseaes.2011.05.012.

Montrasio A. (1984) The "Lanzada-Scermendone Zone": An ophiolitic unit of continental affinity in the southern Rhaetic Alps (Prov. Sondrio-Italy). *Schweizerische Mineralogische und Petrographische Mitteilungen*, Vol. 64, No. 1/2, pp.111–129.

Nichol D. (2000) Two contrasting nephrite jade types. *Journal of Gemmology*, Vol. 27, No. 4, pp. 193–200.

Nichol D., Giess H. (2005) Nephrite jade from Mastabia in Val Malenco, Italy. *Journal of Gemmology*, Vol. 29, No. 5/6, pp. 305–311.

O'Donoghue M., Ed. (2006) *Gems*, 6th ed. Butterworth-Heinemann, Oxford, UK.

Pecharsky V. K., Zavalij P.Y. (2003) *Fundamental of Powder Diffraction and Structural Characterization of Materials*. Kluver Academic Publishers, USA.

Rietveld H.M. (1969) A profile refinement method for nuclear and magnetic structures. *Journal of Applied Crystallography*, Vol. 2, No. 2, pp. 65–71, http://dx.doi.org/10.1107/S0021889869006558.

Siqin B., Qjan R., Zhuo S., Gan F., Dong M., Hua Y. (2012) Glow discharge mass spectrometry studies on nephrite minerals formed by different metallogenic mechanisms and geological environments. *International Journal of Mass Spectrometry*, Vol. 309, No. 1, pp. 206–211, http://dx.doi.org/10.1016/j.ijms.2011.10.003.

Trommsdorff V., Piccardo G.B., Montrasio A. (1993) From magmatism through metamorphism to sea floor emplacement of subcontinental Adria lithosphere during pre-Alpine rifting (Malenco, Italy). *Schweizerische Mineralogische und Petrographische Mitteilungen, Vol. 73*, No. 2, pp. 191–203.

Vennemann T.W., O'Neil J.R. (1993) A simple and inexpensive method of hydrogen isotope and water analyses of minerals and rocks based on zinc reagent. *Chemical Geology*, Vol. 103, No. 1-4, pp. 227–234, http://dx.doi.org/10.1016/0009-2541(93)90303-Z.

Yui T.-F., Kwon S.-T. (2002) Origin of a dolomite-related jade deposit at Chuncheon, Korea. *Economic Geology*, Vol. 97, No. 3, pp. 593–601, http://dx.doi.org/10.2113/gsecongeo.97.3.593.

Zhang B., Lu T., Chen H., Ke J. (2011) Research and identification of natural and treated nephrite in China. *G&G*, Vol. 47, No. 2, pp. 122.

OPTICAL DEFECTS IN DIAMOND: A QUICK REFERENCE CHART

James E. Shigley and Christopher M. Breeding

Gem diamonds owe much of their value to their color, or lack thereof. Defects in the atomic structure of diamond are responsible for this color and are important for the identification of color treatments. This article and its tables are intended as a quick reference for gemologists as they read about various common diamond defects in the gemological literature.

Despite the commercial value of natural-color diamonds, distinguishing them from treated diamonds remains a significant identification challenge. While some diagnostic visual features exist (inclusions, color or growth zoning, and absorption bands seen with a spectroscope), the separation of natural from synthetic or treated diamonds is not always possible using standard gemological methods. In such cases, advanced spectroscopic analysis at a professional gem-testing laboratory is required. Imaging of luminescence distribution patterns is also a helpful tool for recognizing synthetic diamonds (Martineau et al., 2004; Shigley et al., 2004).

In a laboratory setting, the identification of diamonds is based mainly on the detection of tiny imperfections in the atomic lattice. These "defect centers" may include foreign impurity atoms (typically nitrogen, and occasionally boron or hydrogen); carbon atom vacancies in the lattice (either single or clusters of neighboring vacancies); carbon atoms positioned in between normal lattice locations (interstitials); and dislocations where planes of carbon atoms are offset from one another due to plastic deformation. Not all of these lattice imperfections create spectroscopic features, but several do so by allowing the diamond to absorb particular energies of incident light or radiation. Defects can occur randomly or in particular locations within the lattice. Diamonds can contain more than one type of defect, and in natural diamonds, defects can be altered over geologic time in the earth or by exposure to heat or radiation during color treatment.

So-called optical defects (or optical centers) cause absorption in the visible or near-visible portions of the electromagnetic spectrum, often producing coloration (e.g., figure 1). Luminescence reactions result when defects absorb higher-energy incident radiation and then reemit lower-energy radiation as visible light. Optical defects occur in very low concentrations in all diamonds, and their presence can be detected using spectroscopic techniques. A theoretically "pure and perfect" diamond containing no such defects would appear colorless.

Figure 1. The red color of the graining in this Fancy red diamond from Brazil is caused by absorption related to the 550 nm band. This band, the most common cause of pink to red color in natural, untreated diamonds, is thought to be the result of a defect created by plastic deformation. Photomicrograph by Jian Xin (Jae) Liao; magnified 50×.
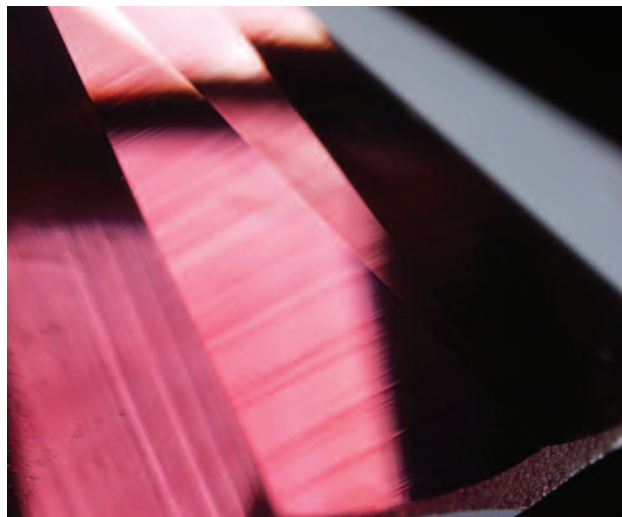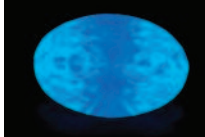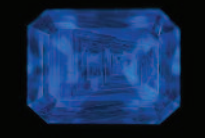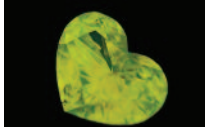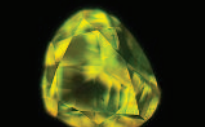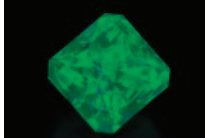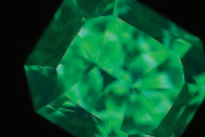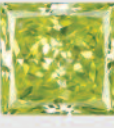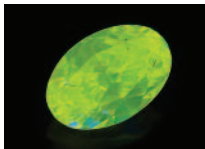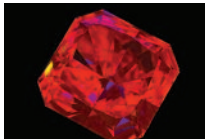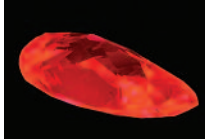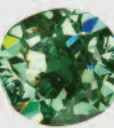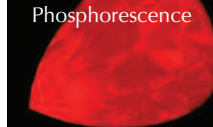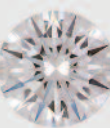
TABLE 1. Important optical defects in diamond and their effect on color and luminescence.

Color	Optical defect and spectroscopic means of detection	LWUV fluorescence (~365 nm lamp)	DiamondView luminescence (<220 nm source)
No effect	**ND1:** A defect with an absorption line at **393.6 nm** (3.150 eV). Thought to consist of a vacancy in the negative charge state (V⁻). Produced by natural or artificial irradiation. *UV*	No effect	No effect
	N3: An impurity and intrinsic defect with an absorption line at **415.2 nm** (2.985 eV) and associated bands. Thought to consist of three substitutional nitrogen atoms surrounding a vacancy (3N+V). Often occurs with the associated N2 (477.2 nm) and several other related bands (465, 452, 435, and 423 nm) in "Cape" diamond spectra. All are naturally occurring. *UV, PL, EPR*		
	480 band: A naturally occurring optical defect of uncertain structure (sometimes attributed to substitutional oxygen) in type I diamonds with a broad absorption band centered at **480 nm** (2.580 eV). *UV*		
	H4: An impurity and intrinsic defect with an absorption line at **496.2 nm** (2.498 eV). Thought to consist of four substitutional nitrogen atoms surrounding two vacancies (4N+2V). Occurs naturally or can be produced by irradiation followed by annealing. *UV, PL*		
	H3: An impurity and intrinsic defect with an absorption line at **503.2 nm** (2.463 eV) and associated bands. Thought to consist of two substitutional nitrogen atoms separated by a vacancy in a neutral charge state (N-V-N)⁰. Occurs naturally or can be produced by irradiation followed by annealing or by high-pressure, high-temperature annealing. *UV, PL*		
May contribute to a green color	**3H:** A defect with an absorption line at **503.4 nm** (2.462 eV). Thought to be related to interstitial carbon (I). Produced by natural or artificial irradiation. *UV, PL*	No effect	No effect
	550 band: An optical center of uncertain structure with a broad absorption band centered at **550 nm** (2.250 eV). Thought to result from plastic deformation of the lattice structure. Occurs naturally. *UV*	No effect	No effect
	NV⁰: An impurity and intrinsic defect with an absorption line at **575 nm** (2.156 eV) and associated bands. Thought to consist of a single substitutional nitrogen atom associated with a vacancy in a neutral charge state (NV⁰). Occurs naturally or can be produced by irradiation followed by annealing. *PL, EPR, UV*		
May contribute to other colors	**595 band:** An optical defect of uncertain structure with an absorption band at **594.4 nm** (2.086 eV). Thought to be related to nitrogen. Occurs naturally or can be produced by irradiation followed by annealing. *UV*	No effect	No effect
	NV⁻: An impurity and intrinsic defect with an absorption line at **637 nm** (1.945 eV) and associated bands. Thought to consist of a single substitutional nitrogen atom associated with a vacancy in a negative charge state (NV⁻). Occurs naturally or can be produced by irradiation followed by annealing or by high-pressure, high-temperature annealing. *PL, EPR, UV*		
	GR1: A defect with a pair of absorption lines at **740.9 nm** (1.673 eV) and at **744.4 nm** (1.665 eV) and associated bands. Thought to consist of a vacancy in a neutral charge state (V⁰). Produced by natural or artificial irradiation. *UV, PL*	No effect	No effect

Color	Optical defect and spectroscopic means of detection	LWUV fluorescence (~365 nm lamp)	DiamondView luminescence (<220 nm source)
May contribute to a green color	**H2:** An impurity and intrinsic defect with an absorption line at **986.3 nm** (1.256 eV, 10125 cm^{-1}) and associated bands. Thought to consist of two substitutional nitrogen atoms separated by a vacancy in a negative charge state (N-V-N)$^-$. Occurs naturally or can be produced by irradiation followed by annealing or by high-pressure, high-temperature annealing. *IR, PL*	No effect	No effect
No effect	**H1c:** An impurity and intrinsic defect of uncertain structure with an infrared absorption line at **1934 nm** (0.6408 eV, 5171 cm^{-1}). Thought to be associated with nitrogen B centers. Occurs naturally or can be produced by irradiation followed by annealing. *IR*	No effect	No effect
No effect	**H1b:** An impurity and intrinsic defect of uncertain structure with an infrared absorption line at **2024 nm** (0.612 eV, 4941 cm^{-1}). Thought to be associated with nitrogen A centers. Occurs naturally or can be produced by irradiation followed by annealing. *IR*	No effect	No effect
	Hydrogen: Defect(s) of uncertain structure with many related infrared absorption lines, most notably at **3107 cm^{-1}** (0.385 eV). Occurs naturally. This defect can also produce yellow and violet colors. *IR, UV*	No effect	No effect
	Boron: A defect with a primary infrared absorption line at **2803 cm^{-1}** (0.348 eV) and associated lines, and a band extending into the visible region. Thought to consist of single substitutional boron atoms. Occurs naturally. This defect produces red phosphorescence. *IR*	Phosphorescence	Phosphorescence
	A center: A defect with an infrared absorption band at **1282 cm^{-1}** (0.159 eV). Thought to consist of two adjacent substitutional nitrogen atoms (N-N). Occurs naturally. *IR*	Quenches luminescence	Quenches luminescence
	B center: A defect with an infrared absorption band at **1175 cm^{-1}** (0.146 eV). Thought to consist of four adjacent substitutional nitrogen atoms surrounding a vacancy (4N+V). Occurs naturally. *IR*	No effect	No effect
	C center: A defect with an infrared absorption band at **1130 cm^{-1}** (0.140 eV). Thought to consist of a single substitutional nitrogen atom (N). Occurs naturally or can be produced by high-pressure, high-temperature annealing of diamonds containing A or B centers. *IR, UV, EPR*	No effect	No effect
No effect	**H1a:** An impurity and intrinsic defect of uncertain structure with an infrared absorption line at **1450 cm^{-1}** (0.180 eV). Thought to be associated with interstitial nitrogen. Occurs naturally or can be produced by irradiation followed by annealing. *IR*	No effect	No effect
No effect	**Platelet:** An impurity and intrinsic defect of uncertain structure with an infrared absorption line at about **1360 cm^{-1}** (0.169 eV). Thought to be associated with groups of interstitial carbon atoms. Occurs naturally. *IR*	No effect	No effect
	Vacancy cluster: A defect of uncertain structure with increasing absorption toward the blue end of the spectrum. Thought to consist of groups of vacancies. Occurs naturally. *UV*	No effect	No effect

UV = Ultraviolet-visible absorption spectroscopy
IR = Infrared absorption spectroscopy

PL = Photoluminescence spectroscopy
EPR = Electron paramagnetic resonance spectroscopy

TABLE 2. Spectroscopic techniques for characterizing lattice defects in diamond.

Technique	Type of spectroscopy	Typical scan range	Commonly detected features and defects	Test conditions	Advantages	Disadvantages	Comments
Ultraviolet/ visible/near-infrared (UV-Vis-NIR)	Absorption (transmission)	250–800 nm	ND1, N3, N2, H3, H4, 595 nm, and GR1	~77 K temperature	Evaluation of color-causing defects; relatively inexpensive	Large samples absorb too much light, causing detector saturation; difficulty quantifying results from faceted stones because of the uncertain path length of light travel	Staple technique in gemological laboratories; can be performed with scanning or dispersive detector
Mid- to near-infrared (IR)	Absorption (transmission)	400–11,000 cm^{-1}	A and B aggregate centers, C centers, various hydrogen-related defects, H1a, H1b, H1c, H2, and "amber centers"	Room temperature	Determination of diamond type; relatively in-expensive; defect concentrations can be quantified by normalization	Large samples absorb too much light, causing detector saturation	Staple technique in gemological laboratories
Raman	Luminescence	100–2000 cm^{-1} Raman shift	Diamond Raman line (1332 cm^{-1})	Room temperature	Identification of diamond; analysis of internal strain	Expensive; yields little information regarding treatment; difficulty analyzing strongly fluorescent samples	Typically used for diamond vs. non-diamond identification (provides little other information)
Photoluminescence (PL)	Luminescence	350–1000 nm	N3, 490.7 nm, H4, H3, NV^0, NV$^-$, GR1, H- and Ni-related defects	~77 K temperature or lower	Detection of HPHT treatment; characterization of low-concentration defects; small analysis area allows for detailed investigation	Expensive; difficulty analyzing strongly fluorescent samples; variety of laser excitations required to activate various defects; requires carefully controlled cryogenic test temperatures	Lasers of various wavelengths used for excitation (most commonly 325, 488, 514, 532, and 633 nm); required for effective treatment detection
Cathodoluminescence (CL)	Luminescence	400–700 nm	A band, B band, N3, H3, and H4	Room temperature	Evaluation of internal structure; detection of defects causing luminescence	Requires an electron beam and a vacuum; provides little information about color treatment	Rarely used, limited data obtainable
Electron-spin/paramagnetic resonance (ESR, EPR)	Resonance absorption in a changing magnetic field		C centers, NV defects	Room temperature	Detection of very low-concentration defects; evaluation of specific defect structures and charges	Very expensive; long sample run times; provides little information about color treatment	Typically used for defect research

As a quick reference for gemologists, table 1 lists the most common lattice defects, including those that can create color and/or luminescence reactions in diamond. The scientific name of the defect, as well as the wavelength (or wavenumber) and electron volt (eV) positions of the main and associated spectral bands, are shown along with photos of representative diamonds. The most common spectroscopic technique used to detect the defect center is indicated by a code shown in italics.

Some precautions should be kept in mind when using this table. Each lattice defect is known to produce a particular diamond color or luminescence. For instance, the GR1 center produces green or blue-green color. But the reverse is not necessarily true—for example, not all green diamonds owe their color to the GR1 center. In fact, there are several causes of green color. In some cases, a diamond contains more than one optical defect, and its color stems from a combination of defects. In other cases, a diamond's

color may arise from absorption caused by one optical center, while its luminescence may result from another optical center.

Table 2 provides a comparison of the most common spectroscopic techniques for diamond characterization. For further reading on color in diamond, the Additional Reading list serves as a reference guide to access the much larger range of gemological and technical literature on diamond identification.

ADDITIONAL READING

Collins A.T. (2001) The colour of diamond and how it can be changed. *Journal of Gemmology*, Vol. 27, No. 6, pp. 341–359.

——— (2003) The detection of colour-enhanced and synthetic gem diamonds by optical spectroscopy. *Diamond and Related Materials*, Vol. 12, No. 10/11, pp. 1976–1983, http://dx.doi.org/10.1016/S0925-9635(03)00262-0.

Cunningham D. (2011) *The Diamond Compendium*. NAG Press, Robert Hale Ltd., London.

Deljanin B., Simic D., Zaitsev A., Chapman J., Dobrinets I., Widemann A., del Re N., Middleton T., Deljanin E., De Stefano A. (2008) Characterization of pink diamonds of different origin: Natural (Argyle, non-Argyle), irradiated and annealed, treated with multiprocess, coated and synthetic. *Diamond and Related Materials*, Vol. 17, No. 7/10, pp. 1169–1178, http://dx.doi.org/10.1016/j.diamond.2008.03.014.

Eaton-Magaña S., Post J.E., Heaney P.J., Walters R.A., Breeding C.M., Butler J.E. (2007) Fluorescence spectra of colored diamonds using a rapid, mobile spectrometer. *G&G*, Vol. 43, No. 4, pp. 332–351, http://dx.doi.org/10.5741/GEMS.43.4.332.

Fritsch E. (1998) The nature of color in diamond. In G.E. Harlow, Ed., *The Nature of Diamonds*. Cambridge University Press in association with the American Museum of Natural History, New York, pp. 23–47.

Hofer S.C. (1998) *Collecting and Classifying Coloured Diamonds: An Illustrated Study of the Aurora Collection*. Ashland Press, New York.

Martineau P.M., Lawson S.C., Taylor A.J., Quinn S.J., Evans D.J.F., Crowder M.J. (2004) Identification of synthetic diamond grown using chemical vapor deposition (CVD). *G&G*, Vol. 40, No. 1, pp. 2–25, http://dx.doi.org/10.5741/GEMS.40.1.2.

Shigley J.E., Breeding C.M., Shen A.H. (2004) An updated chart on the characteristics of HPHT-grown synthetic diamonds. *G&G*, Vol. 40, No. 4, pp. 303–313, http://dx.doi.org/10.5741/GEMS.40.4.303.

Tappert R., Tappert M.C. (2011) *Diamonds in Nature: A Guide to Rough Diamonds*. Springer, New York, pp. 45–68.

Zaitsev A.M. (2000) Vibronic spectra of impurity-related optical centers in diamond. *Physical Review B*, Vol. 61, No.19, pp. 12909–12922, http://dx.doi.org/10.1103/PhysRevB.61.12909.

——— (2001) *Lattice Defects in Diamonds: A Data Handbook*. Springer-Verlag, Berlin.

ABOUT THE AUTHORS
Dr. Shigley (jshigley@gia.edu) is a distinguished research fellow, and Dr. Breeding is a research scientist, at GIA's laboratory in Carlsbad, California.

THANK YOU DONORS

GIA appreciates gifts to its permanent collection, as well as gemstones, library materials, and other non-cash assets to be used in education and research activities. These contributions help GIA further its public service mission while offering donors philanthropic benefits. We extend sincere thanks to all 2012 contributors.

CIRCLE OF HONOR*

$100,000 and higher

The Aaron Group

Dr. Suman Agrawal

Almaza Jewelers
(Ziad H. Noshie)

American Pearl Company

Amsterdam Sauer

Robert and Marlene Anderson

Aurafin-Oroamerica

Banks International Gemology Inc.
(Daniel and Bo Banks)

The Bell Group-Rio Grande

Allan Caplan

Chatham Created Gems Inc.
(Thomas H. Chatham)

PierLuigi Dalla Rovere

The De Beers Group

Debbie and Mark Ebert

Fabricjewelry

Dallas R. Hales

Dr. H. Tracy Hall

Dr. Gary R. and Barbara E. Hansen

James Y. Hung, M.D.

Inta Gems Inc.

J.O. Crystal Company Inc.
(Judith Osmer)

Jewel America Inc.
(Zvi and Rachel Wertheimer)

Kazanjian Bros., Inc.

KCB Natural Pearls
(K.C. Bell)

William F. and Jeanne H. Larson

Stephen Lentz

Sophie Leu

Honoring Betty H. Llewellyn

Marshall and Janella Martin

Roz and Gene Meieran

Nancy B. & Co.

Dr. Kurt Nassau

John & Laura Ramsey

R. Ed Romack

Art Sexauer

Shades of the Earth
(Laura and Wayne Thompson)

Ambaji Shinde

S.H. Silver Company
(Stephen and Eileen Silver)

Dr. Geoffrey A. Smith

D. Swarovski & Co.

Touraine Family Trust

United States Pearl Co.
(James and Venetia Peach)

Robert H. Vanderkay

Vicenza Fair

2012 D0NORS*

$50,000 to $99,999
Steven and Betty Lou Neely

$10,000 to $49,999
David & Gale Kempf

Cos Altobelli

Jerry Bearman

Dudley Blauwet

Mark Mauthner

$5,000 to $9,999
G. Scott Davies

House of Onyx

New Era Gems
(Steve Ulatowski)

Joanna Seetoo Designs
(Joanna Joy Seetoo)

In Memory of
Dr. Frederick H. Pough

Albert & Louise Garcia

$2,500 to $4,999
In Memory of Larry Crandall

In Memory of Harry Nest

Hussain Rezayee

In Memory of Rudolf Loewenthal

In Memory of Dr. V. Premanda

William "Flint" Carter

Cynthia Renée Inc.

$1,000 to $2,499
Aurora Gems

Bill Barker

Alexandre Reza

Rattanachart Mining Co., Ltd.

Oceanview Mines, LLC
(Jeff Swanger)

Courtland Lee

Stephen Lewis Solomon
J.D., G.G.

Kaufman Enterprises (Mark Kaufman)

Terri Ottaway

$500 to $999
Renée Newman

Nalini Pattni

Aucoin Hart Jewelers

Dr. Jaroslav Hyršl

Under $500
Jewelry Design by Ruth Fitzgerald

Suzanne Harned

Marco Campos-Venuti

Throwin' Stones/Intuitively Inspired Designs

Mawingu Gems

Gems TV

Rajneesh Bhandari

German Salazar

Robert Sielecki

In Memory of Arthur Metzger
(Elise A. Skalwold and William A. Bassett of Cornell University)

Kathryn Kimmel

In Memory of Bobby R. Prade

Kessler Mfg. & Imports Inc.

Jeweler Profit Inc.

Fabrice Danet

Brendan M. Laurs

Ginger Bartlett Hughes

Revere Academy of Jewelry Arts

Sea Hunt Pearls

David S. Bunevich

John Catron

Cosmos Gems (Leonardo Silva Souto)

R.T. Boyd Limited

TheBeautyInTheRocks.com
(Mauro Pantò)

* All are cumulative donations

If you are interested in making a donation and receiving tax benefits information, please contact:

MCKENZIE SANTIMER
call: (760) 603-4150
fax: (760) 603-4056
email: mckenzie.santimer@gia.edu

G&G Lab Notes

Editors
Thomas M. Moses | Shane F. McClure

Atypical Freshwater CULTURED PEARLS with Damaged Nacre

Recently the East Coast laboratory received four baroque-shaped pearls ranging in size from 9.07 × 13.50 × 14.03 mm to 9.32 × 11.34 × 15.77 mm and weighing between 10.63 and 13.60 ct. On each of the four samples, the outermost surface nacre layers exhibited large holes and gaps, revealing one or more distinct nacreous layers underneath (figure 1). These underlying nacreous layers displayed good luster and overlapping platelet surface structures, and the large gaps between the inner and outermost nacre layers indicated that smaller pearls had been used as nuclei during the culturing process.

Further gemological testing by energy-dispersive X-ray fluorescence (EDXRF) and inductively coupled

plasma–mass spectrometry (ICP-MS) confirmed that both the outer and inner nacre layers originated from a freshwater environment. Some of these pearls contained widely varying amounts of trace elements (i.e., Mn and Mg) between the outer and inner layers, but previous studies have found that uneven distribution of trace elements can also occur in a pearl's cross section (R. Lu et al., "Operational considerations of EDXRF, LA-ICP-MS, and photoluminescence techniques in the analysis of pearls," Summer 2011 G&G, pp. 149–150).

Two did not show any distinct internal demarcation when examined with X-radiography in various directions (figure 2). This lack of a clear internal boundary may be due to multiple culturing attempts using the same pearl as a nucleus, which can cause overlapped internal structures and multiple distinct nacreous layers under the surface (figure 1, sample 3). In addition, structures typical of non-bead cultured pearls were observed in these micro X-radiographs, suggesting that freshwater cultured pearls were used as nuclei during the culturing process.

Finally, photographs of the X-ray fluorescence reactions of all four pearls were taken in a dark environment (figure 3). Various intensities of green and yellowish green fluorescence could be observed within each nacreous layer, presumably due to varying concentrations of manganese between layers and among the pearls themselves (H.A. Hanni et al., "X-ray luminescence, a valuable test in pearl identification," 2005 Journal of Gemmology, 29, 5/6, pp. 325–329). More interestingly, reddish fluorescence was also observed around the damaged areas of the nacre in samples 3 and 4. This was possibly caused by foreign material between the "nucleus-pearl" and the outer nacre layers, which may also contribute to the lack of distinct demarcation observed in the cultured structure.

While similar types of pearls with intact outer nacre surfaces have been reported on previously (E. Stack, "Chinese freshwater cultured pearls beaded with baroque freshwater cultured pearls," Fall 2011 G&G, pp. 244–245), the ambiguous internal structures, interesting X-ray fluorescence properties,

Figure 1. These four atypical freshwater cultured pearls with damaged nacre reveal one or more distinct nacreous layers underneath. Left to right: samples 1–4.
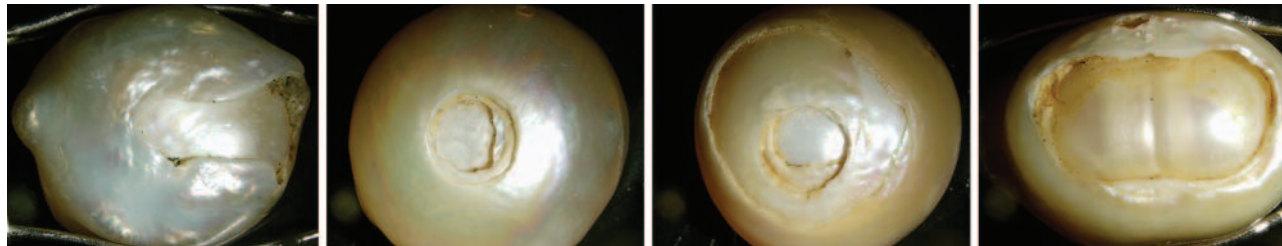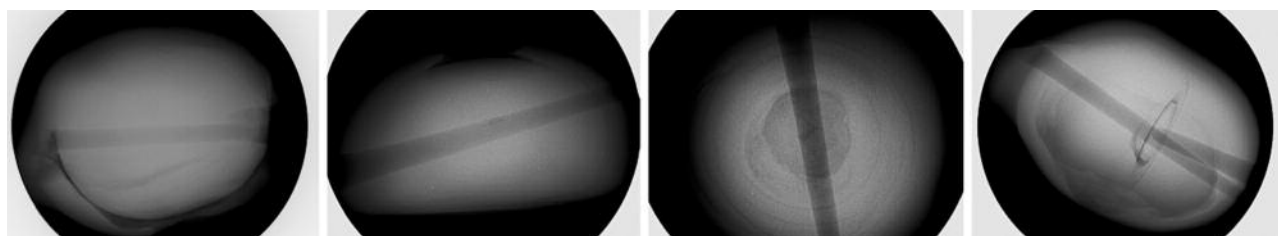
Figure 2. X-radiographs show partial demarcation between the outer and inner structures of cultured pearls 1 and 2, but fail to reveal any clear boundaries in samples 3 and 4.

and large gaps in the outer nacre layers of these four samples offer a rare view of their internal physical structure and appearance, obtained free of destructive testing.

Chunhui Zhou

DIAMOND
Calcium Fluoride Coating Found On 13 "Fancy" Pinks

Coating gemstones to alter or improve their color is the oldest known enhancement method. Early coatings, particularly on diamond, were easily detected, often visible using a 10× loupe. But advances made after World War II resulted in more durable coatings and films that were subtler and harder to detect.

A common coating was calcium fluoride (CaF_2) doped with gold (Au) nanoparticles. CaF_2 causes a broad absorption band at about 520 nm, similar to the band at about 550 nm that largely accounts for the pink color of natural diamonds.

Recently submitted to the East Coast laboratory for identification and grading was a group of 13 pink diamonds (figure 4). The round brilliants ranged from 0.42 to 0.50 ct and had a Fancy pink to Fancy Intense pink color. Figure 4 also shows the patchy appearance characteristic of coated diamonds. Microscopic examination using reflected light revealed obvious coating on the pavilion facets, with patchy colorless areas where it had been removed (figure 5).

The UV-visible spectra of all 13 diamonds exhibited a broad band centered at about 520 nm, not at 550 nm as expected. This band is responsible for the pink coloration, and the 520 nm position identified the coating as fluoride.

This example demonstrates that traditional treatments such as coating are still prevalent in the trade, and great care must be taken to identify them. Because coatings are not permanent, all 13 diamonds were issued identification reports disclosing the treatment.

Fish-Like Inclusion

It is always a pleasant surprise to find a new and interesting inclusion during routine observation. But an inclusion that reminds us of a particular shape, an effect known as *pareidolia* (Winter 2007 Lab Notes, pp. 363–364), is a geologic wonder.

The New York laboratory recently received a natural yellow (graded as Fancy yellow) "Cape" 0.51 ct rectangular faceted diamond exhibiting such a feature. Examination of the stone revealed a series of table-reaching fractures and clouds that seemed to form the outline and scale-like detail of a fish (figure 6). The inclusion is large in relation to the stone, encompassing nearly 75% of the table.

Figure 4. These face-up images of 0.45 ct and 0.5 ct pink round brilliants are representative of the 13 coated pink diamonds submitted.
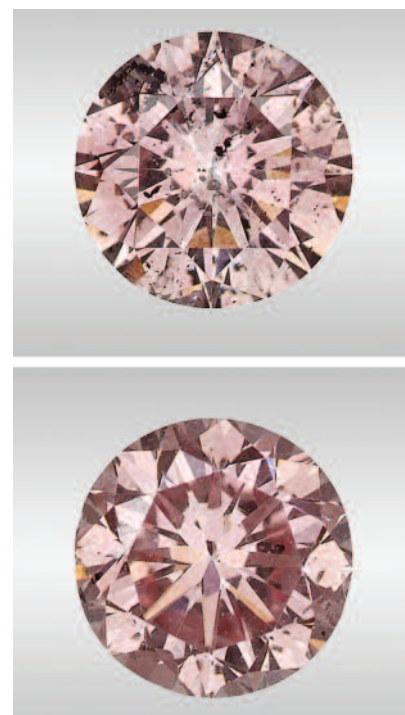

Figure 3. X-ray fluorescence images of the four cultured pearls showing various degrees of green or yellowish green fluorescence between inner and outer layers. Atypical orangy red fluorescence is also visible between the layers in samples 3 and 4.
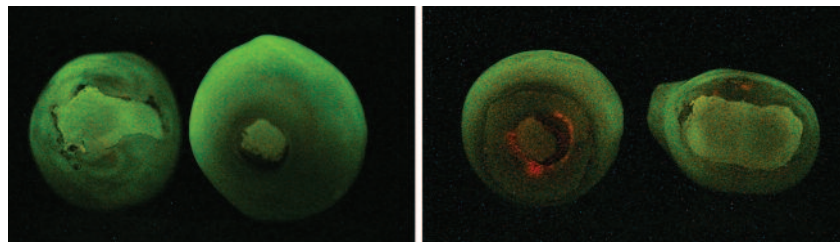
Figure 5. Photomicrographs of the diamonds from figure 4, taken with reflected light at 80× and 100× magnification, reveal the coating applied to the pavilion facets.

Figure 7. This 24.16 ct oval-cut diamond (20.47 × 14.00 × 10.72 mm) was color graded as Fancy Intense green-yellow, and identified as artificially irradiated and annealed.

Nearly all fractures in diamond result from the interaction among multiple cleavage directions (*The MicroWorld of Diamonds*, Gemworld International, 2000, p. 97). While often detrimental to the value of a stone, this inclusion serves as a useful identifier, and such findings help keep the study of gems enjoyable.

Martha Altobelli

A Large Irradiated Green-Yellow

Artificially irradiated diamonds are common in the trade, and identifying them remains a challenge. The New York lab recently identified a large diamond as artificially irradiated based on careful spectroscopic analysis and a review of the lab's database.

This 24.16 ct oval-cut diamond (20.47 × 14.00 × 10.72 mm) was color graded as Fancy Intense green-yellow

(figure 7). The color was distributed evenly throughout the stone, with no color zoning detected. It showed strong yellow and blue fluorescence to long-wave UV radiation, and moderate yellow fluorescence to short-wave UV radiation. This fluorescence reaction and absence of chalkiness are seen in some natural diamonds with a similar bodycolor. Absorption spectrum in the mid-infrared region showed saturated absorptions in the one-phonon region, indicating a type Ia diamond with a high concentration of nitrogen. Also recorded were a moderate platelet peak at 1368 cm⁻¹ (approximately 2.1 cm⁻¹ intensity) and a weak absorption at 1433 cm⁻¹. No hydrogen-related ab-

sorption or H1b/H1c center in the near-infrared region was recorded. Absorption spectrum of this diamond in the ultraviolet/visible/near-infrared (UV-Vis-NIR) region at liquid-nitrogen temperature (figure 8) showed a moderately strong absorption from the N3 (415.2 nm) and H4 (496.0 nm) centers, as well as weak absorptions at 512.8, 594.4, and 741.2 nm (GR1). Absence of the H3 optical center was confirmed by photoluminescence spectroscopy at

Figure 8. After irradiation and annealing treatment, a significant amount of optical center H4 was introduced. This is mainly responsible for the color improvement from Fancy brownish greenish yellow to Fancy Intense green-yellow. N3 absorptions in two spectra in this plot were normalized to the same intensity.

Figure 6. This pavilion view of the 4.76 × 4.30 × 2.75 mm Fancy yellow diamond displays the "fish" inclusion scene. The fish appears to be facing to the right. Magnified 40×.

UV-VIS-NIR SPECTRA

liquid-nitrogen temperature with 488 nm laser excitation. A fluorescence image collected using the Diamond-View showed a gradual change from a predominantly blue table region to a mostly green upper pavilion and girdle area. The spectral features ob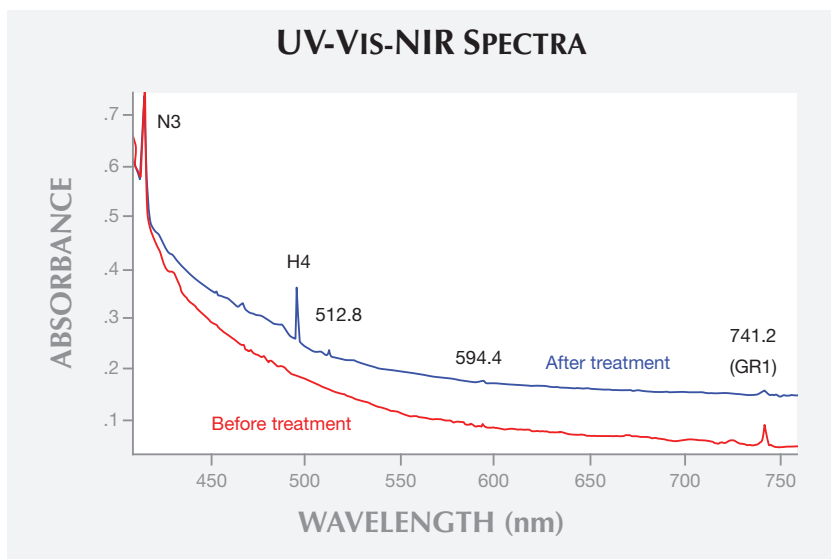served in this large diamond are rarely encountered in natural diamonds, raising the possibility of artificial irradiation treatment.

A search of the GIA database found a very good match between this stone and a previously tested diamond. The two diamonds were identical in measurements and weight, as well as their infrared absorption spectroscopic features, though the previous grade was Fancy brownish greenish yellow. This significant improvement in color appearance is attributed to the relatively high concentration of the H4 center produced by the artificial irradiation/annealing treatment confirmed in this study.

Despite its suspicious spectroscopic features, this irradiated diamond showed some gemological features normally observed in diamonds with similar natural color. This example demonstrates the value of careful spectral and gemological analysis, combined with a review of the GIA database, in gem identification.

Wuyi Wang, Paul Johnson, and Emiko Yazawa

Strong Color Zoning Reflects Complex Growth Environment

A 2.08 ct emerald-cut diamond recently submitted to the Carlsbad laboratory received a color grade of Fancy Dark orangy brown. Its strong color zoning, visible without magnification (figure 9), consisted of a dark orangy brown section with a few near-colorless bands and a near-colorless area. The orangy brown section showed numerous very small oriented reflective inclusions, visible in figure 9 only as dark clouds, that are typically associated with type IaA diamonds colored by 480 nm visible absorption bands. Both the near-colorless side and the colorless bands displayed very few oriented reflective inclusions.

The diamond's unusual fluorescence under both long- and short-wave UV illumination can be seen in figures 10 and 11, respectively. Under long-wave UV (handheld lamp) the near-colorless section showed typical blue fluorescence. The orangy brown section displayed a yellowish fluorescence, which is common in type IaA yellow diamonds. Under the higher-energy, shorter-wavelength UV excitation of the DiamondView, the distinction between the colors became even more pronounced, and the blue fluorescence of the near-colorless bands was clearly visible within the yellowish green fluorescence of the orangy brown section. Yellow phosphorescence, common in type IaA diamonds colored by 480 nm visible absorption bands, was also observed in the orangy brown area.

Infrared spectroscopy revealed a type Ia diamond with both A and B aggregates. When IR spectra were collected separately from the near-colorless and orangy brown sections, distinct differences were noted. The orangy brown section contained ~33 ppm of A-aggregated nitrogen and ~15 ppm of B-aggregated nitrogen, whereas the near-colorless section showed significantly higher concentrations: approximately 139 ppm of A aggregates and 100 ppm of B aggregates. In addition to the higher overall nitrogen content, the near-colorless portion contained a higher proportion

Figure 10. Under long-wave UV illumination at 10× magnification, the diamond's color zones showed blue and yellowish fluorescence.

of B-aggregated nitrogen impurities.

The unique zoning observed in this diamond likely reflects changing conditions during growth. Variations in nitrogen and possibly oxygen content in the earth's interior—480 nm defects are reportedly related to oxygen impurities in diamond—could have produced the noteworthy color and fluorescence zoning that reveal the complex growth history.

Troy Ardon

Very Large Rough Diamond

Throughout history, the discovery of very large diamond rough has been a rare occurrence. Not only is it unlikely to survive the journey from deep in the earth to the surface, but modern extraction methods, including the use of crushers to break large rock, can reduce such specimens to

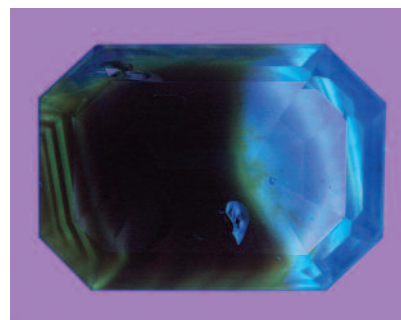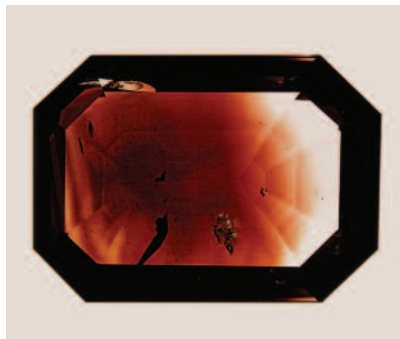*Figure 9. The strong color zoning in this Fancy Dark orangy brown diamond was visible at 10× magnification.*

Figure 11. This DiamondView image of the color-zoned diamond shows an even more pronounced distinction between the colors.
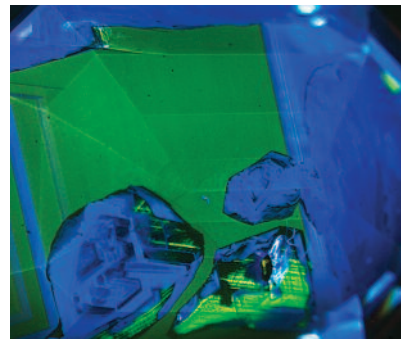
smaller pieces. Therefore, the recent examination of a 1,138 ct rough diamond (62.51 × 47.61 × 45.56 mm; figure 12) provided a unique opportunity to document the largest single-crystal natural diamond ever examined by GIA. While it is possible there have been larger unreported specimens, a search of public sources (e.g., I. Balfour, *Famous Diamonds*, 5th ed., Antique Collectors Club, 2008) suggests this could be the second-largest rough diamond in history—between the 3,106 ct Cullinan and the 995 ct Excelsior, both of gem quality.

Known to be from the Democratic Republic of the Congo, this stone displayed Raman spectroscopic features characteristic of diamond. The sheer size presented a challenge with IR absorption spectroscopy analysis, as it was too large for the regular sample chamber, beam condenser, or DRIFT units. Instead, we used an infrared microscope with reflective mode and obtained a high-quality absorption spectrum. The rough was identified as a natural type IaA diamond with very high nitrogen concentration. We also detected a weak hydrogen-related absorption peak at 3107 cm^{-1}, a common feature in natural diamond. Also recorded were strong absorption bands at approximately 3300, 2920, 1700, and 1550 cm^{-1}, attributed to micron and sub-micron inclusions. Photoluminescence spectra were recorded at liquid-nitrogen temperature with various laser excitations. The main emission features were broad bands at 700 and 787 nm. The crystal also displayed a very weak blue fluorescence under long- and short-wave ultraviolet radiation, another typical feature.

The irregular morphology of the 1,138 ct rough was quite interesting, as diamond usually occurs in octahedral or dodecahedral forms. But such a morphology is less likely to be maintained as a large crystal forms. Numerous randomly shaped and distributed inclusions may have contributed to the irregular crystal growth. These inclusions also caused the gray color appearance.

The specimen's strong surface dissolution provided a visual document of its journey from deep in the earth. At the high temperatures in the earth's interior, diamond can remain stable only under very high pressure. As the diamond was transported to the surface, the decrease in pressure would have dissolved the stone unless it made the journey rapidly. The surface of the 1,138 ct crystal speaks to the change that took place during its journey and represents the fine line between our experiencing this rare item and never having known it at all.

John M. King and Wuyi Wang

Unusual Curved Color Zoning In EMERALD

While curved color zoning is typically associated with melt-grown synthetics, particularly flame-fusion products such as synthetic corundum and synthetic spinel, an unusual natural emerald with this feature was recently examined in the Carlsbad and Bangkok laboratories. This 1.17 ct emerald was obtained for GIA's permanent reference collection (sample number 100305160993) at a street market in Kabul, Afghanistan, for its very unusual inclusion scene. The stone was represented as being of Afghan (Panjsher) origin, but the internal inclusions seemed to resemble those of emeralds collected from the Swat Valley of Pakistan. Careful chemical analysis by laser ablation–inductively coupled plasma–mass spectrometry (LA-ICP-MS) was performed at the GIA lab in Bangkok. The chemical data showed a fairly even composition within the sample except for chromium, which varied proportionately with the green color zoning (from approximately 300 to 9000 ppmw Cr). The chemical data of the unusual emerald were compared to those of reference standards from known deposits, particularly Panjsher and the Swat Valley, to investigate its probable origin. The data showed a close match only with the reference emeralds from the Swat Valley, making that the most likely origin.

The gemological properties showed an RI of 1.589–1.597 and a visible spectrum consistent with emerald. The stone showed no reaction to a standard 4-watt gemological UV light source. Microscopic examination revealed numerous inclusions of pyrite, carbonates, and reflective thin films oriented perpendicular to the optic axis (parallel to the length of the stone), a typical assemblage of a natural emerald. The most unusual observation about this stone was a prominent green "S" shape color zone that ran down its length (figure 13). Emerald's hexagonal structure would ordinarily lead one to expect planar or angular color zoning related to the crystal morphology. The presence of curving zones in a faceted emerald was an anomaly that needed further examination.

One possible explanation for the

Figure 12. This 1,138 ct single-crystal natural diamond (62.51 × 47.61 × 45.56 mm) is the largest ever examined by GIA.

Figure 13. This 1.17 ct emerald, which hosted pyrite and carbonate crystals, displayed unusual curved zoning.

unusual zoning is that compressional geological forces caused shearing along the emerald crystal's basal plane. This was supported by the appearance of pyrite grains, which looked as if single, brittle pyrite crystals had been sheared and slightly displaced parallel to the basal plane of the beryl host (figure 14). This apparent lateral shearing movement throughout the emerald crystal could have caused the pyrite grains to separate into aligned tabular fragments offset from each other and the beryl host. Also observed between the pyrite grains were planar optical irregularities. These planes suggested localized shear zones that would have significantly higher defect concentration, giving rise to the optical nonconformity consistent with their location between the tabular pyrite inclusions. Under cross-polarized illumination, we observed dense clusters of birefringent crystals that were essentially invisible under non-polarized lighting. The low relief of these dense inclusions suggested they were beryl inclusions within the beryl host, possibly a result of partial recrystallization caused by dynamic environmental conditions.

Gemology is generally a non-destructive, observational science, which can be limiting at times. Destructive techniques could have revealed the crystallographic orientation of the pyrite grains with respect to each other and explained the stone's unusual structure. Because this was a unique sample, destructive testing
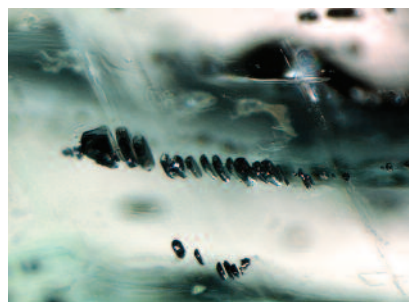
was not a practical approach. While the exact cause of this unusual zoning remains unknown, it is certainly interesting and thought provoking. The discovery of such gems demonstrates that there are complex geological conditions we do not yet understand which, when observed, invite further gemological exploration.

Nathan Renfro, Vincent Pardieu, and Supharart Sangsawong

Rare Faceted NEPTUNITE

An 11.78 ct faceted "black" octagonal modified step-cut stone was recently presented to the Carlsbad laboratory for identification (figure 15). Standard gemological testing revealed an RI of 1.69–1.73 and a hydrostatic SG of 3.19. Microscopic examination with a fiber-optic light source showed the stone was actually a very dark orange red. It was heavily included with fractures and platelets, as well as randomly oriented unidentified thin needles evenly distributed throughout the gem (figure 16). These tests suggested neptunite, an identity confirmed using Raman spectroscopy.

Neptunite commonly occurs in association with, and as a guest inclusion in, the rare blue mineral benitoite (E.J. Gübelin and J.I. Koivula, *Photoatlas of Inclusions in*

Figure 15. This unusual 11.78 ct faceted neptunite appeared to be black but was actually a dark orange red.
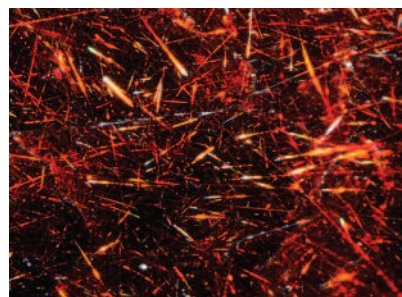
Figure 16. The orangy red neptunite contained dense needles of unknown composition. Field of view: 1.72 mm.

Gemstones, Vol. 1, ABC Edition, Zurich, 1986). Both minerals are Ti-bearing silicates. Benitoite may contain whitish inclusions of crossite (an amphibole) or natrolite (a zeolite), so it is possible that the thin needles in this neptunite are composed of one of these metamorphic minerals. The main source of neptunite is San Benito, California, where it is found along the walls of natrolite veins in blueschist (B. Laurs et al., "Benitoite from the New Idria District, San Benito County, California," Fall 1997 *G&G*, pp. 166–187). The type locality for this material is the Narsarsuk pegmatite in Greenland (O.V. Petersen and O. Johnsen, "Mineral species first described from Greenland," *Canadian Mineralogist* Special Publication No. 8, 2005, pp. 76–77). Neptunite crystals have been found in sizes up to a few inches, but they are rarely faceted because of their brittle nature and relative softness (5–6 on the Mohs scale). The few crystals that are faceted usually weigh less than 1 ct, making this large specimen of particular interest. To the best of our knowledge, this is the first faceted neptunite identified by GIA.

Amy Cooper and Tara Allen

Figure 14. Arrays of tabular offset pyrite fragments were seen throughout this unusual emerald. Field of view: 0.86 mm.

COLORED STONES AND ORGANIC MATERIALS

Ancient tourmaline and beryl from Afghanistan. A large private collection of beads and carvings from antique excavations, assembled in the 1970s by a collector in Afghanistan, was recently examined. The pieces were claimed to be found near the ancient city of Bactra (modern-day Balkh), 300 km northwest of Kabul near the border with Uzbekistan. Bactra was a center of the Bactrian civilization, which flourished from 2500 to 1500 BC. The collection contains several thousand drilled beads, mostly agate, carnelian, and rare blue chalcedony. The next most abundant materials are turquoise—some as small as 1 mm in diameter—and lapis lazuli. Less common are garnet (two types of almandine), rock crystal, amethyst, serpentinite, and steatite, as well as organic materials identified as amber, pearl, and mother-of-pearl. Other very interesting finds are treated rock crystal and milky quartz, both containing blue glass spots on their surfaces, similar to medieval sapphire imitations (Fall 2001 GNI, pp. 243–245).

The two most interesting pieces, a pink bird (figure 1) and a very pale blue bead (figure 2), were studied in detail. The bird had a light green bottom section, measured 13.9 × 13.6 × 7.6 mm, and weighed 9.52 ct, with a refractive index close to 1.63. It was strongly pleochroic (pink and colorless), and it was uniaxial negative in a conoscope. In both short- and long-wave UV light the center was inert, but a thin triangular zone of light blue fluorescence was visible near the surface. These tests confirmed the stone's identification as tourmaline. It was originally a "watermelon" tourmaline, pink with a green rim, but only a small part of the green rim had been preserved.

The pale blue bead was set in a heavily corroded metal, probably bronze. The entire piece measured 20.7 × 12.3 × 6.7 mm and weighed 20.28 ct, with an RI close to 1.59. The

Figure 1: This 9.52 ct pink tourmaline is part of an extensive private collection of ornaments claimed to be from ancient Afghanistan. Photo by Jaroslav Hyršl.

stone was weakly pleochroic (very light blue and colorless), inert in UV light, and uniaxial negative in a conoscope. These results indicated a very pale aquamarine. The identification of both beads was confirmed by their Raman patterns, collected by A. Gilg (Technical University of Munich).

Both beads are possibly among the oldest of their kind. Large and historically significant rubellites have been reported from the 14th and 16th centuries, and a single beryl bead from Nubia has been dated back to Predynastic time (before 3200 BC), but few details are known. The first beryl locality of significance was reportedly the Egyptian emerald deposit exploited as early as the Ptolemaic era (after 332 BC).

Both tourmaline and aquamarine are typical pegmatite minerals. Gem-bearing pegmatites have been mined since the 1970s in the Nuristan province of eastern Afghanistan and northern Pakistan—the possible origin of both beads.

Jaroslav Hyršl (hyrsl@hotmail.com)
Prague, Czech Republic

Figure 2: This aquamarine bead, reported to be from Afghanistan, weighs 20.28 ct and is likely one of the oldest of its kind. Photo by Jaroslav Hyršl.

Orangy pink coated "soft coral." Dyeing white coral to imitate popular colors such as red, orange, and pink is a widely known practice. But a bead strand examined at the Gem Testing Laboratory in Jaipur, India, revealed a coloring method unfamiliar to gemologists (figure 3).

The strand weighed approximately 380 ct and contained spherical beads ranging from 6 to 15 mm in diameter. These were identified as coral belonging to the species *Melithaea ocracea* of the order Alcyonacea (e.g., M.C. Pederson, *Gem and Ornamental Materials of Organic Origin*, Elsevier Butterworth-Heinemann, Oxford, 2004, pp. 192–218). Their surface showed deep pores and dull luster. The presence of pores was sufficient to identify the beads as soft coral, which is also characterized by a spongy, brittle, rough appearance.

Although their identification was straightforward, the beads' appearance caused doubt regarding their color origin. When viewed under magnification (figure 4), distinct color concentrations were visible within the surface pores and cavities. The coloring agent was restricted to the surface,

Figure 3. This string of orangy pink "soft coral" beads (6–15 mm in diameter) displayed a rough surface and large pores. Photo by Gagan Choudhary.
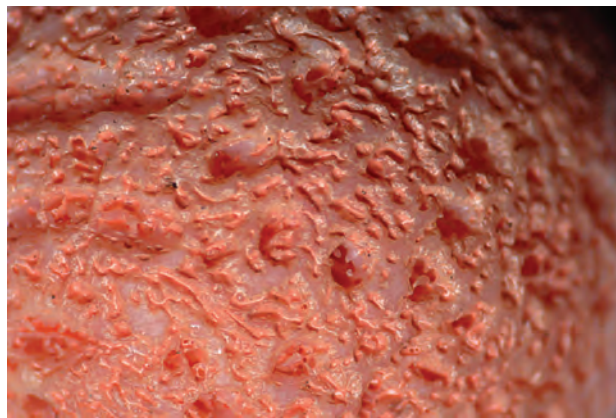
Figure 4. Under magnification, distinct color concentrations are visible within the pores and cavities of this "soft coral." The apparent use of a coloring agent only on the surface, evidenced by the enamel-like appearance within the trenches and the whiteness of the ridges, suggests these beads were coated, not dyed. Photomicrograph by Gagan Choudhary; magnified 48×.

producing an enamel-like appearance in the trenches while the ridges appeared white. This evidence suggested that the beads were coated with paint rather than dyed.

Although the microscopic features were sufficient for identification, further tests confirmed those findings. Under UV light, the beads displayed bright orange fluorescence (more strongly under short-wave), a feature commonly associated with pink-orange dyes. No typical absorption spectra were visible under a desk-model spectroscope or recorded with a UV-Vis-NIR spectrometer. This is because the beads' dull luster, opacity, and rough, uneven surfaces neither reflect light (in diffused reflectance mode) nor absorb it (in transmission mode). Weak and broad absorption bands were displayed at approximately 540 and 680 nm, and the presence of calcium carbonate (aragonite) was confirmed by Raman spectroscopy.

Such "soft coral" is commonly dyed red and the pores are filled with a polymer to enhance polish and luster. But this specimen's color and luster were unusual. The lab also received similar coral strands in pink and black, suggesting this dye method can produce a variety of colors.

Gagan Choudhary (gagan@gjepcindia.com)
Gem Testing Laboratory, Jaipur, India

Strands of tiny akoya keshi pearls. How small can a pearl be? At the American Gem Trade Association show in Tucson, the Japanese Pearl Exporting Co. presented some akoya keshi pearls only 0.7–0.9 mm in diameter (figure 5). At this size, it is difficult to distinguish individual pearls when looking at a strand. According to the seller, the single strand shown in figure 5 contains more than 300,000 keshi pearls, which would take one person four years to drill and assemble.

Traditional tools are used to drill these tiny pearls. A thick wooden board is soaked overnight to soften it, and each pearl is embedded in the board to keep it stable. A

Figure 5. This strand contains more than 300,000 akoya keshi pearls, each one only 0.7–0.9 mm in diameter. Photo by Eric Welch.

very sharp, thin drill is used to bore a hole in each pearl. By pulling a thread attached to the drill, the worker can keep rotating the drill until it reaches the desired depth.

"Keshi," the Japanese word for poppy seeds, form as by-products of the akoya culturing process. They account for less than 0.5% of all annual akoya production, which has diminished in recent years. Akoya keshi pearls come in various sizes, shapes, colors, and lusters. Strands are often paired with colored stones such as ruby and sapphire (figure 6).

Tao Hsu
GIA, Carlsbad

Green kyanite. At the Riverpark Inn show in Tucson, gem dealer Tom Schneider (San Diego, California) exhibited a parcel of kyanite displaying an unusual saturated yellowish green color (figure 7). Mr. Schneider said he purchased several kilograms of the material in Arusha, Tanzania, its stated country of origin. While greenish blue, blue, and orange kyanite from Tanzania have been previously documented (Winter 2004 GNI, pp. 341–342; Summer 2009 GNI, pp. 146–147), this would be the first vibrantly colored yellowish green material from there. Yellowish green kyanite from Brazil has been previously reported (Winter 2001 GNI, pp. 337–338), but it had a light color and lacked the strong saturation of the material from Tanzania.

A cushion cabochon fashioned from one of the rough crystals was examined in the Carlsbad laboratory and

Figure 6. These tiny akoya keshi pearl strands are paired with ruby and sapphire. Photo by Eric Welch.

Figure 7. These yellowish green kyanite rough crystals range from 1.4 to 5.1 grams, while the cushion cabochon weighs 4.84 ct. Photo by Don Mengason.

exhibited the following properties: an RI of 1.719–1.731, a hydrostatic SG of 3.70, and no reaction to short- or long-wave UV radiation. These physical properties were consistent with those published for kyanite. This identification was confirmed by Raman spectroscopy.

Microscopic examination revealed several transparent crystals, fine particles, numerous fractures, and cleavages. Trapped in several cracks was an epigenetic reddish brown mineral residue. It is also notable that a small percentage of the rough crystals examined showed narrow blue color zones.

To determine the cause of the yellowish green color, we collected a visible spectrum using a UV-Vis-NIR scanning spectrophotometer (figure 8). This revealed prominent features located in the visible region at 432 and 445 nm. These features have been attributed to Fe^{3+} in kyanite (R.G. Burns, *Mineralogical Applications of Crystal Field Theory*, 2nd ed., 1993, Cambridge University Press). LA-ICP-MS measurements collected on the cushion cabochon confirmed a high concentration of iron—more than 20,400 ppmw, consistent

Figure 8. Visible spectroscopy revealed dominant absorption features at 432 and 445 nm, attributed to Fe^{3+} and consistent with the very high levels of iron measured in this yellowish green kyanite.
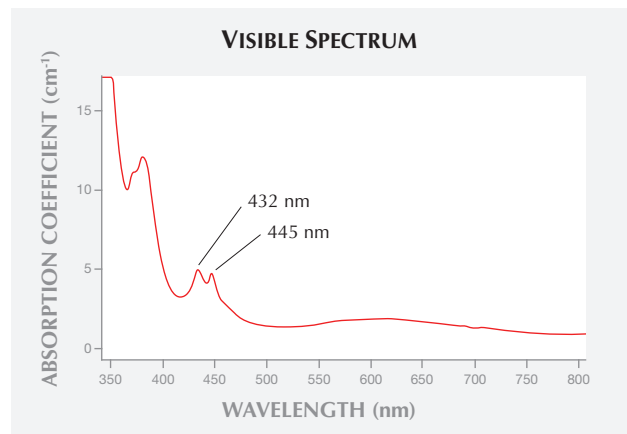
with the saturated yellowish green color.

This new supply of vibrant yellowish green material from Tanzania presents an inexpensive option for unusual ornamental gem materials.

Nathan Renfro and Andy Shen
GIA, Carlsbad

Banded mimetite. Mimetite is a member of the apatite group and a lead chloro-arsenate, known to collectors as one of the rarest faceted stones. Some yellow transparent specimens weighing up to 1 ct are known from old finds in Tsumeb, Namibia. Small orange translucent stones under 0.5 ct have been faceted from Chinese mimetite, and a new type of lapidary mimetite (figure 9), likely from Bolivia but purchased in Tucson without a reported locality, was identified recently.

The cabochon measured 40.5 × 31.7 × 7.2 mm and weighed 177.75 ct, with a very high luster. Its lapidary work was of low quality, but the stone had a very nice agate-like structure, with alternating yellow-brown and dark brown layers. It closely resembled two unusual ornamental stones: the colloidal variety of sphalerite (figure 10) known by the German name *schalenblende*, and the colloidal cassiterite variety called "wood tin." Schalenblende is known from many localities worldwide, mainly Poland but also Bolivia, where it is very difficult to visually distinguish from mimetite. Wood tin is known to be from Bolivia and Mexico.

The RI of all three minerals is very high, over the refractometer limit. Loose stones can be easily distinguished by their hardness and specific gravity, and the hardness of mimetite and schalenblende is the same, about 3.5 on the Mohs scale. Wood tin is much harder, about 6.5. The SG of the mimetite was 6.31, considerably higher than the 3.8–4.2 of a typical schalenblende. The SG of wood tin can vary from 5.2 to 6.6, likely depending on the presence of thin chalcedony layers. Mimetite and wood tin are also inert in UV light, while schalenblende is usually yellow in long-wave
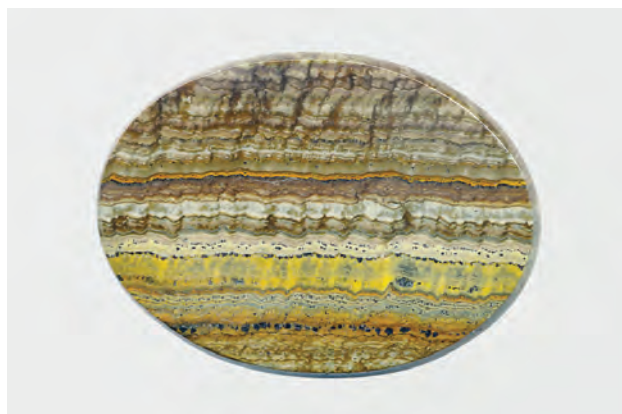
Figure 10. The sphalerite variety schalenblende *has characteristics similar to those of banded mimetite. This specimen weighs 106.20 ct. Photo by Jaroslav Hyršl.*

UV. The mimetite was identified by powder X-ray diffraction by John Attard of San Diego, but its exact origin could not be determined. Thin veins of mimetite deposited from hot springs are known to have been mined from a deposit in Lomitas, located in La Paz Department, Bolivia.

Jaroslav Hyršl

Turquoise-rock crystal composite. Recently examined was a faceted rock crystal backed by a slice of turquoise—an obvious but unusual combination of gem materials. The 21.58 ct oval measured 20.02 × 15.03 × 9.05 mm and was easily identified as a composite due to its color and appearance. From the top, it appeared light greenish blue (figure 11, left); from the sides, it exhibited a colorless top and bluish green slice at the base (figure 11, right).

Further tests confirmed the specimen was made of rock crystal and turquoise, based on its colorless and greenish blue components. The colorless portion displayed an RI of 1.543–1.552, with birefringence of 0.009, while the greenish blue layer displayed a vague shadow edge at around 1.61. Under magnification, the colorless portion was clean and free of inclusions, while the greenish blue base showed some whitish cloudy patches, consistent with those in turquoise and similar materials. As expected, the junction plane contained numerous trapped, flattened gas bubbles without color. Under long- and short-wave UV light, a white to light yellowish glow was visible only along the junction plane, indicative of glue. Under a desk-model spectroscope, the specimen showed a weak absorption at about 430 nm.

FTIR spectra taken by orienting the colorless portion displayed peaks at approximately 3595, 3480, 3380, 3305, and 3198 cm^{-1}—a pattern typically associated with natural rock crystal (e.g., Summer 2011 GNI, pp. 146–147). Raman analysis of the greenish blue base using a 532 nm laser in the 200–2000 cm^{-1} region revealed a strong peak at about 1040 cm^{-1}, with a number of weaker peaks at approximately 238, 334, 427, 482, 554, 596, 645, and 810 cm^{-1}. These peaks are consistent with those of turquoise in both the lab's database and the RRUFF database of Raman spectra. No polymer-related

Figure 9. This mimetite cabochon, likely from Bolivia, weighs 177.75 ct and has an agate-like structure of yellow-brown and dark brown layers. Photo by Jaroslav Hyršl.
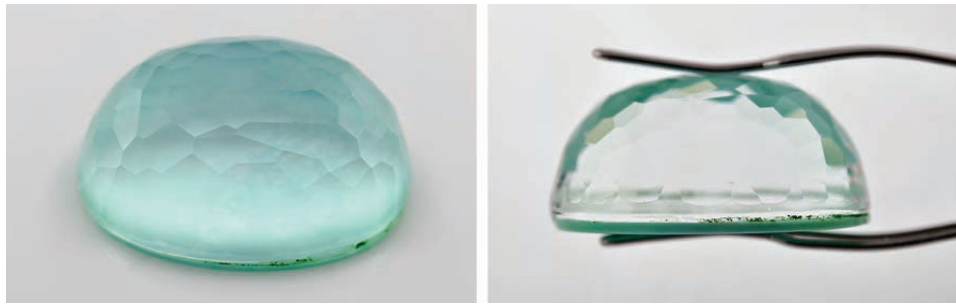
Figure 11. This 21.58 ct composite was found to have a top section of natural rock crystal and a base of natural turquoise. Photos by Gagan Choudhary.

peaks were present. In addition, qualitative energy-dispersive X-ray fluorescence (EDXRF) analysis revealed the presence of Al, P, Fe, and Cu, consistent with turquoise. As mentioned, a desk-model spectroscope revealed a weak absorption at around 430 nm, and the same was confirmed using UV-Vis spectroscopy, which displayed a sharp peak at approximately 429 nm (Fe^{3+}) and a broad absorption at about 680 nm (Cu^{2+}), suggesting natural rather than dyed color.

While analysis using both classical and spectroscopic techniques identified this as a composite of natural rock crystal and turquoise, the reason for its creation is still unclear.

Gagan Choudhary

SYNTHETICS AND SIMULANTS

Imitation Larimar. Pectolite is a mineral of the wollastonite group with the chemical formula $NaCa_2Si_3O_8(OH)$. It has an RI of 1.599–1.628, with a typical spot RI reading of about 1.60 and a specific gravity of 2.81. The light blue variety of this mineral, known by the trade name "Larimar," has only been reported from the Dominican Republic (R.E. Woodruff and E. Fritsch, "Blue pectolite from the Dominican Republic," Winter 1989 *G&G*, pp. 216–225; figure 1).

We recently acquired a 3.91 ct drop-shaped cabochon, purchased in India as a Larimar imitation, that consisted of a ceramic material (figure 12, left). According to the vendor, the material was manufactured in China. Close microscopic examination showed white gas bubbles and blue color concentration (figure 13).

The cabochon's spot RI reading of 1.53 and SG of 1.87

were distinctly lower than the values for Larimar. Semi-quantitative EDXRF chemical analysis gave a composition of 95% Al_2O_3 and 4% SiO_2, with traces of SO_3, K_2O, CaO, Sc_2O_3, Cr_2O_3, Fe_2O_3, and Ga_2O_3. In contrast, the average composition of pectolite consists of 54.23% SiO_2, 33.74% CaO, 9.32% Na_2O, and 2.71% H_2O.

Although the imitation material does indeed resemble Larimar, standard gemological tests such as microscopy, RI, and SG should be sufficient to distinguish it.

Lore Kiefert
Gübelin Gem Lab Ltd.
Lucerne, Switzerland

Peter Groenenboom
AEL Arnhem
Arnhem, Netherlands

ERRATA

1. The Spring 2013 "About the Cover" on the masthead page should have listed the photographer as Jian Xin (Jae) Liao.

2. The Lab Notes figure 7 photo was by Paul Johnson.

3. In the GNI entry on dumortierite-quartz rock, two lines were omitted from the bottom left column on p. 60. The complete version is available in the Spring 2013 issue at www.gia.edu/gems-gemology.

Figure 13. Microscopic observation reveals dark blue color concentrations and whitish gas bubbles. Photomicrograph by Lore Kiefert; magnified 40×.

Figure 12. This 3.91 ct ceramic imitation of Larimar (left) is shown with Larimar from the Dominican Republic. Photo by Lore Kiefert.

The Young Generation—Tom + Jutta Munsteiner

By Wilhem Lindemann, 225 pp., illus., publ. by Arnoldsche Art Publishers, Stuttgart, Germany, 2012. US$85.00

With this remarkable bilingual volume, Wilhem Lindemann presents the works of husband and wife Tom and Jutta Munsteiner, master gem cutters and jewelers. Second-generation gem cutter Tom Munsteiner followed in his father's footsteps. Beginning in the 1960s and continuing through the mid-1990s, Bernd Munsteiner reinvented gemstone cutting with his unique edged, multi-faceted gem carvings. Working near Idar-Oberstein, the mecca of the German lapidary and colored stone trades, he cut an abundance of "rediscovered" gemstones from Brazil's pegmatites, particularly tourmalines, aquamarines, amethysts, quartzes, and topazes.

Tom and Jutta Munsteiner were classically trained as apprentices after showing early artistic promise. Today, they exhibit at venues such as the Tucson, Las Vegas, and Basel shows. Visiting the couple's booth, one can only be struck by the strength and originality of their creations. Whether gem carving or sculpture, each work exhibits a fine combination of jewelry and art.

In the first part of the book, Lindemann retraces the evolution of lapidary art, from late third millennium BC cylinder seals to contemporary art movements such as Bauhaus. Tom Munsteiner's influences, dating as far back as the Romantic era, have inspired him to envision the entire crystal as a landscape, with its inclusions and flaws.

He rejects traditional gem cuts such as the round brilliant, which focuses on the reflecting quality of a diamond and is far too complex for human sight. For this reason he adopted a cutting style that is asymmetrical, inviting the viewer's attention inside the crystal rather than on its reflective qualities.

The next section takes the reader on an inspirational journey through the work of Tom Munsteiner, whose most memorable creations include "Magic Eye," "Ritmo," and "Spirit of Nature." The "Magic Eye" pieces have a sphere carved into the back of the gems at the interface of their axes to produce reflections on the face. "Ritmo" features geometric notches on the reverse side that re-create random asymmetrical imaginary structures. Of particular interest to gemologists is the "Spirit of Nature" series of gem carvings, which accentuates the inclusions in a wide range of materials. Some of the most striking pieces are an oligoclase with red hematite platelets, an elongated aquamarine prism with a helicoidal inclusion running through the length of the gemstone, and rock crystal carvings displaying phantom crystals. This section is one of the book's strongest.

The third part focuses on Jutta's jewelry designs, which feature her husband's gem carvings. Her inspiration features sinuous curves, as evidenced by the "Personalities" neckpiece series. The imposing "Jeanne d'Arc" necklace shows a ridged, elongated rutilated quartz mounted on a custom-made snake chain.

The fourth part illustrates Tom and Jutta's collaboration through images of their classic jewelry, such as the "Twins" series of rings, each featuring an original gemstone carving paired with a diamond. They incorporated a proprietary round cut called "Spirit," as well as the square "Context," which resembles a modern French cut.

The photos exhibit a precision that complements the Munsteiners' cutting style. The rendering of color has not been artificially enhanced, which is often a treacherous temptation. Captions generally mention the carat weight of the gemstones, which is important since neither scale nor dimension are indicated. Given the impressive size of certain objects, this information helps the reader appreciate the quality and craftsmanship involved. Numerous illustrations show the variation of cutting, within each series and from one series to another. The many photos serve to distinguish the couple's respective pieces: Tom's unique gem carvings and Jutta's minimalist jewelry designed with a sharp, powerful style.

The text speaks to the Munsteiners' inspiration, but also describes how the gems were cut—a helpful feature since some of the gems were cut from the back to create a sense of volume and depth. Without those details, such techniques would be difficult to comprehend.

This magnificent opus would have benefited from the Munsteiners' original sketches, which would have made the volume livelier and more personal. Some basic technical explanation of cut and lapidary work, being the couple's craft and expertise, would have also provided some foundation. But these criticisms are minor considering the quality of gemstones and illustrations presented.

The illuminating text and the striking originality and craftsmanship of the Munsteiners' work make this volume a real treat for students, gemologists, gem cutters, and jewelry enthusiasts. It offers an incomparable insight into Europe's contemporary and cutting-edge creations

DELPHINE A. LEBLANC
Hoboken, New Jersey

Dictionary of Gemstones & Jewelry

By Akira Chikayama, 652 pp., illus., publ. by IMACBC Co., Tokyo, 2013, US$100.00

The late Akira Chikayama was a noted gemologist who considered the *Dictionary of Gemstones & Jewelry* his personal "world heritage." Indeed, the very scope of this dictionary is impressive. Entries include gems, minerals, sources, synthetics, treatments, jewelry findings, tools used in gem cutting and jewelry making, famous gemologists, scientists, mineralogists, and artists—the list goes on.

A massive undertaking to begin with, the book was translated from Japanese to English. But it did contain some minor errors. In the listing for the Searcy diamond, for example, there appears a photo of the Sancy. In the entry for "abraded culet," the author likened it to an open culet, which I do not agree with. And seeing entries on Gübelin, Kunz, and Shipley made me wonder why Dana, Liddicoat, and Sinkankas were not included.

But as a general reference, the book serves its purpose well. The appendices alone are useful, covering a wide range of subjects and provid-

ing charts on birthstones, ring sizes, hallmarks, and more. Overall, this volume would make a nice addition to any gemological library if cost is not an issue.

JANA MIYAHIRA-SMITH
Gemological Institute of America
Carlsbad, California

Splendour and Science of Pearls

By Dona Mary Dirlam and Robert Weldon, Eds., 139 pp., publ. by the Gemological Institute of America, Carlsbad, California, 2013, US$89.00

The book delivers a broad overview of the world of natural and cultured pearls. The well-researched and lavishly illustrated presentation covers the history of pearls, world localities, classification, treatments, identification, fashion, and the future of the industry. One chapter focuses on the story of pearls in India, while another includes results from a GIA research study on natural pearls from the Arabian Gulf.

GIA LIBRARY STAFF
Gemological Institute of America
Carlsbad, California

Jewels from Imperial St. Petersburg

By Ulla Tillander-Godenhielm, 295 pp., illus. publ. by Unicorn Press, London, 2012. US$80.00

Geared toward the jewelry historian, this thoroughly researched work is a window into the world of the Russian imperial Romanovs, starting with the reign of Empress Elizabeth (1741–1762), and ending with

Nicholas II in 1917. The author details in chronological order the jewelry and *objects d'art* manufactured in St. Petersburg during this period. The book contains numerous photos of the jewels and family portraits from that era

GIA LIBRARY STAFF

Diamond Street: The Hidden World of Hatton Garden

By Rachel Lichtenstein, 364 pp., publ. by Hamish Hamilton, London, 2012. £20.00

Hatton Garden is a famous area in London where jewelry has been manufactured since medieval times, and it continues to be known as a fine jewelry and diamond center. The author reveals the history of the jewelry trade there and offers stories about the people, culture, and lore of this fascinating district.

GIA LIBRARY STAFF

DIAMONDS

Abenteuer Jakutien: Auf den Spuren der Diamanten [Adventures in Yakutia: On the track of the diamonds]. K. Erler and H. Vollstädt, *Lapis*, Vol. 38, No. 4, 2013, pp. 18–25, 54 [in German].

This article starts with a brief history of Yakutian diamond production, from Mikhail V. Lomonosov's theory of diamond deposits in 1761 to the discovery of the first kimberlites in 1954 to present-day operations. The bulk of the article then presents information the authors gathered during two visits to Yakutia, focusing on Mirny.

The report contains a map and a list of data on the most important mines. It is lavishly illustrated with images of Mirny—the mine, the town, the museum—and impressive diamond specimens.

RT

China market: The new frontier. *Diamond World*, Vol. 40, No. 2, Jan-Feb. 2013, p. 126-132

China, the world's second-largest jewelry consumer after the United States, is also the second-largest jewelry manufacturing center after India. There is enormous potential for diamond jewelry in China, where the government has supported the industry through major policy decisions: reducing the VAT (value-added tax) on diamonds, abolishing import duties, and setting up the Shanghai Diamonds Exchange for trading in rough and polished diamonds. The government has signed multibillion dollar resources-for-infrastructure deals with various African governments, securing its supply of rough diamonds. These efforts have drawn a huge flow of capital investment from diamond companies in Tel Aviv and Antwerp. Skilled diamond craftspeople have been brought in from Surat, India, to train Chinese workers.

Overall, China has cheaper labor costs than India, and its workforce provides better finishing of jewelry. Much of the work in Chinese jewelry factories is automated, and the level of technology and infrastructure is higher than in India. India produces every size and type of rough, while China mostly manufactures sawables. While India holds the advantage in manufacturing, China is a major consumer of polished diamonds. China is also better at jewelry manufacturing. But there is no original Chinese brand of international jewelry, and country needs better communication with the outside world.

GL

The Ellendale diamond field: Exploration history, discovery, geology, and mining. A. L. Ahmat, The *Australian Gemmologist*, Vol. 24, No. 12, 2012, pp. 280–288

The Ellendale diamond field in West Kimberley is one of only three hard-rock diamond mine locations in Australia. Though not the first Australian diamond mine, Ellendale was the country's first hard-rock deposit. It holds a special place in world diamond history as it led in November 1976 to the recognition of a new host-rock for diamond, olivine lamproite. Up until that time, commercial-sized diamonds were considered to be sourced only from kimberlite. The Ellendale lamproites are geologically very young, only 22 Ma (million of years) old. Within several years of the initial discovery, some 46 lamproite pipes were found at Ellendale. By 1980, 38 of these pipes had been assessed for their diamond content.

More than two decades later, geologists from the Kimberley Diamond Company (KDC) recognized eluvial diamond enrichment over these pipes. After a lengthy legal battle, they wrested the Ellendale mining lease from the Ashton Joint Venture and commenced mining there in May 2002. Ellendale is recognized as a source of high-value fancy yellow diamonds. These high priced stones have been marketed through a special deal with Tiffany & Co since 2009. But the future of mining there is tenuous. Ellendale 4 was closed in 2009, and the high Australian dollar, combined with dwindling reserves, may jeopardize the survival of Ellendale 9.

GL

EOSFancy: Automatic bruting of fancy shapes. T. Gevers and J. Vandeloo, *De Belgische Diamantnijverheid*, Jan/Feb/Mar 2013 Vol. 83, No. 1, pp. 14–16.

More than eight years ago, Belgium's Scientific Research Centre for Diamonds (WTCOD) developed an automatic bruter for round diamonds. The bruting machine was based on a new principle: the application of a grinding wheel, rotating in a cooling liquid, to a rotating diamond. WTCOD has now expanded the scope of the EOS bruting machine to fancy shapes by linking the feed movement of the disc to the rotating position of the diamond. With EOSFancy, one can brute any convex shape

with high accuracy and symmetry. The new software requires a recent PC with a specific graphics card. EOSFancy can be used manually or via a transfer from a rough scanner. The system can be used for both prebruting and finishing, and it is the ideal complement to laser prebruting. With EOSFancy, a lasered girdle can be finished perpendicular to the table with a result closer to the end dimensions, with a shorter processing time. The development is now in testing phase at a limited number of Antwerp-based diamond companies. A commercial version is expected to be released by HRD during 2013.

GL

Infrared microspectroscopy of natural Argyle pink diamond. K. S. Byrne, J. D. Anstie, J. Chapman, and A.N. Luiten, *Diamond and Related Materials*, Vol. 23, 2012, pp. 125–129, http://dx.doi.org/10.1016/j.diamond.2012.01.032

One of the most distinctive characteristics of natural pink diamond is the lamellae, or "graining," in which the color resides. These features are believed to have formed under plastic deformation. A great deal of research has focused on color centers in diamond, particularly the N-V center. This article investigates the crystalline defect responsible for pink coloration in natural diamond. Infrared microspectroscopic images were obtained to estimate the spatial distribution of B-centers in natural pink Argyle diamonds. The spatial distribution of the nitrogen B-center $(N–V–N_3)$ was anti-correlated with the intensity of pink coloration. The authors believe this is the first such observation. IR spectral features were not influenced by exposure to UV illumination, in contrast to the visible change in coloration under the influence of UV radiation.

GL

Internal texture and syngenetic inclusions in carbonado. F. V. Kaminsky, R. Wirth, and L. Morales, *The Canadian Mineralogist*, Vol. 51, No. 1, pp. 39–55, http://dx.doi.org/10.3749/canmin.51.1.39

Carbonado is a black or dark brown cryptocrystalline aggregate of diamond. Its age ranges from 2.6 to 3.8 Ga (billions of years), according to lead isotopic composition. Carbonados have been found only in alluvial placer deposits, such as those in Brazil and Central Africa, and never in kimberlite. Many hypotheses, including non-kimberlitic, crustal origin of carbonado were proposed by previous researchers. Analysis of internal texture and syngenetic inclusions is important to understanding the genesis.

Carbonado samples were collected from alluvial placer deposits of the Macaubas River basin in the Brazilian state of Minas Gerais and the Ubangi River basin in the Central African Republic. They were dark or nearly black, with a smooth and shiny surface. The

samples contained pores ranging from a few hundred nanometers to a few micrometers. Secondary electron images revealed a typical polycrystalline structure, which showed fine-grained texture with irregularly shaped diamond grains averaging 5 to 15 μm. Grain boundaries were in irregular, zigzag patterns. Numerous pores, up to 20 μm, were found inside grain boundaries. They were usually filled with postgenetic minerals such as kaolinite, flurencite, and quartz. Dislocation lines were also observed within some diamond grains. The pole figures suggested that crystallographic orientations of these grains were quasi-random.

Syngenetic inclusions ranging from 10 to 50 nm were identified using the combined FIB/TEM technique: garnet, apatite (including fluorapatite), phlogopite, silica, Ca-Mg-Sr- and Ca-Ba-carbonates, halides (sylvite, KCl, and bismocolite, BiOCl), native nickel and metal alloys (Fe-Ni, Cr-Fe-Mn, and Pb-As-Mo), oxides (FeO, Fe-Sn-O, TiO_2, SnO_2, and PbO_2), Fe-sulfides, and fluid inclusions. An intergrowth of fluorapatite, phlogopite, and silica was also observed. Almandine-pyrope garnet inclusions with silica-enriched amorphous rims were confirmed. Fluid inclusions contained Si, Al, Fe, O, Ti, Ca, S, Cl, K, and carbonate. These fluid inclusions suggested the carbonados were formed in a chloride-rich environment. Crystal inclusions were not pressure-indicator minerals. Instead, they were stable in a wide range, from crust to lower mantle, except bismocolite, which could only be formed in the crust. Although this whole inclusion assemblage was possibly of crustal origin, conclusive research is still needed. The authors propose that these samples were crystallized and grown in one stage, which was followed by sintering. This hypothesis could be confirmed by comparison with one-stage growth process of a polycrystalline diamondite.

KSM

GEM LOCALITIES

Achate von der Teufelskanzel bei Oberthal im Saarland [Agates of the Teufelskanzel near Oberthal, Saarland, Germany]. K Schäfer, *Lapis*, Vol. 38, No. 5, 2013, pp. 14–21, 54 [in German].

The "Teufelskanzel" (Devil's Pulpit), a rhyolitic promontory at Oberthal about 30 km (20 miles) southwest of Idar-Oberstein, is one of the many small agate deposits of the Nahe-Saar Basin. A failed first attempt to mine the agates in 1882 was followed by rather chaotic rockhound activities and the equally unsuccessful decision by the community of Oberthal to take over all mining activities. Finally, digging for agates was generally prohibited, a ban that is still in force.

The agates generally formed as thunder eggs. They show a very beautiful coloration and often bizarre, picturesque forms that inspire the imagination of the behold-

er. Many also display a strong green long-wave UV fluorescence, supposedly due to uranyl ions.

The beauty of the agates and their fluorescence are illustrated by a range of color photos.

RT

Montana moss agate: Collectible chalcedony from the Yellowstone River. B. Britt, *Rock & Gem*, April, 2013, Vol. 43, No. 4, pp. 34–37.

The expansion of various mining projects in Canada's North (Northwest Territories, Yukon, and Nunavut) is set to lead the country in economic growth over the next two years. Spinoff activity that accompanies mine-related prosperity is also expected to increase based on pending mines in the assessment phases or preproduction stages, thus further boosting employment and local economic development. Production in these areas is expected to last well into the coming decades. Environmental groups and local residents are also interested in the impact on the Canadian North ecosystem as well as the long-term effects on the towns and industry when the boom is over.

ERB

Neufund: Blaue "Wolkenachate" von Weierbach bei Idar-Oberstein, Rheinland-Pfalz [New find: Blue "cloud agates" from Weierbach near Idar-Oberstein, Rhineland-Palatinate]. K. Schäfer, *Lapis*, Vol. 37, No. 6, 2012, pp. 25–29 [in German].

The agate deposits that formed the basis of the lapidary and cutting industry at Idar-Oberstein until the 19th century are mostly depleted. What reaches the market today is the result of rockhound activities. This article reports on a remarkable find from 2012 along a road construction site at Weierbach, near Idar-Oberstein. Found in a small outcrop of volcanic rocks, the nodules showed diameters of 2–12 cm (0.8–4.8 in.). While agates from Idar-Oberstein generally have a fine banding and pastel tones, most of these agates were not banded but showed cloud-like structures and striking sky blue and red colors. The article contains numerous images of the splendid agates and the deposit.

RT

Wittichenite from the Cattle Grid Pit, Mount Gunson Mine, South Australia. R. Noble [noblemin@aussiebb.com.au], *The Mineralogical Record*, March-April, 2013, Vol. 44, pp. 133–143.

In 1981, large, attractive wittichenite crystals found at the Cattle Grid Pit in South Australia were mistaken for chalcocite. Then in 2008, they were correctly identified by the Smithsonian Institution. Electron microprobe analysis of this species shows Cu, Bi, and S (weight percentages of 38.67%, 41.70%, and 19.90%, respectively).

The Cattle Grid wittichenite is brittle, with strongly conchoidal fractures and a relatively low hardness. The colors vary from highly lustrous silvery white to bronze to

a deep purple-black. The crystals are predominantly tabular-prismatic in habit, but some show myriad crystal faces and deeply striated prisms. The Miller indices for these crystal forms, and their intricate and complicated crystal morphology, are discussed in depth.

The article contains 16 large photos of wittichenite, some crystals weighing more than 75 grams, as well as the mine site and the copper localization stratigraphy. The number of wittichenite crystals larger than 2 cm in maximum dimension is estimated to be about 30, and these are held in only three collections (two institutional and one private). Unfortunately, the entire production of copper sulfide concentrate from the Cattle Grid Pit is now owned by a private smelter, where the bismuth-containing wittichenite is considered an undesirable impurity.

ERB

INSTRUMENTS AND TECHNIQUES

Determining the geographical origins of natural emeralds through nondestructive chemical fingerprinting. D. P. Cronin and A. M. Rendle. *The Journal of Gemmology*, Vol. 33, No. 1-4, 2012, pp. 1–13.

The technology to identify a gemstone's geologic and geographic origins has improved in the last decade to the point where accurately pinpointing the locality has become a reality. Using emeralds from different mines in the Cordillera Oriental region of Colombia, some of them only a few miles apart, scientists can now discern minute differences in chemical composition and determine each sample's point of origin by studying the chemical "fingerprints" in their chromophores. The chromophores are trace elements of vanadium, nickel, or magnesium and vary geographically as a result of interstitial fluid migration prior to precipitation.

After recognizing that within-site chemical homogeneity and cross-site chemical heterogeneity depended on the amount of chromophores in the crystal structure, the authors sought to find out if chemical heterogeneity between emerald mining localities was chemically unique and statistically provable based on chromophore components alone. Included in the study were emerald samples from the Muzo, Cosquez, and Guali mines of Colombia, plus the Campo Verdes and Carnaíba mines in Brazil, and the Chantete mine in Zambia. Consideration for sample inclusion in this study involved the history of the host rock chemistry on the skeletal crystal structure, the occurrence of trace elements that link emeralds to their point of origin, the subsurface geology, fluid-rock interactions and the geochemical processes leading to emerald formation.

The study concluded that element-based heterogeneity exists between the six emerald mining sites. Through the use of an Amray scanning electron microscope (SEM) coupled to an EDAX energy-dispersive X-ray spectrometer (EDX), statistically significant chemical heterogeneity between mine sites was revealed by a non-destructive test that preserved the integrity of the sample.

JEC

The yellow color center and trapped electrons in beryl. L. Andersson, [loandersson@bluewin.ch], *The Canadian Mineralogist*, 2013, Vol. 51, No. 1, pp. 15–25, http://dx.doi.org/10.3749/canmin.51.1.15

Investigations continue into the cause of yellow color in beryl. The generally accepted explanation is that it is related to the charge-transfer between Fe^{3+} ions substituting for octahedral Al^{3+} ions in the crystal and the surrounding oxygen ions.

Using electron paramagnetic resonance (EPR), an absorption technique that uses magnetic fields to measure transition energies in atomic defect centers, this study contradicts the accepted interpretation, proposing an alternate model.

Although a strong EPR signal from octahedral Fe^{3+} ions can be found in beryl of all colors, including colorless, the study determined that Fe^{3+} ions substituting for Al^{3+} at the octahedral position cannot be the cause of the yellow color. There is, however, a signal unique to yellow beryl that comes from Fe^{3+} ions at a *tetrahedral* site.

The author proposes a simple model describing the oxidation and reduction processes involving iron electrons trapped in the crystal structure to explain the creation and decay of the yellow color. This study discusses reinterpretations of other experimental findings that lead to different explanations for beryl's colors

ERB

SYNTHETICS AND SIMULANTS

Blue spinel crystals in the $MgAl_2O_4$-$CoAl_2O_4$ series: Part I. Flux growth and chemical characterization. V. d'Ippolito, G. B. Andreozzi (gianni.andreozzi@uniroma1.it), F. Bosi, and U. Hålenius, *American Mineralogist*, Vol. 97, No. 11-12, 2012, pp. 1828–1833, http://dx.doi.org/10.2138/am.2012.4138

Synthetic $CoAl_2O_4$ spinel, a high-temperature oxide (melting point of 1955°C), is the most stable compound of a family of spinel-structured oxides obtained from CO_3O_4 at progressive increase of Al contents. High-quality spinel single crystals with compositions closely corresponding to the solid-solution series spinel *sensu stricto* ($MgAl_2O_4$)-cobalt spinel ($CoAl_2O_4$) were produced by flux growth method, with $Na_2B_4O_7$ as the flux. Low cooling rates and linear temperature profiles were applied in the thermal interval 1200–800°C, followed by rapid cooling. Thermal runs were performed in a reducing atmosphere. Selected crystals were investigated by SEM/EDS X-ray mapping to check for compositional homogeneity and by electron-microprobe analysis to obtain the chemical formula.

Crystals were found to be chemically homogeneous

and entirely representing the $MgAl_2O_4$-$CoAl_2O_4$ solid-solution series, with the latter component ranging from 7% to 100%. The saturation of the vivid blue color increased with total cobalt content, but no shift in color hue was observed along the series. The unit-cell parameter a increased from 8.084 to 8.105 Å along the solid-solution series. The observed linear increase of the a parameter was seemingly due to the higher $CoAl_2O_4$ component. This was a premature and misleading conclusion, however, because structural changes in spinel may depend on both chemical composition and inversion parameter, which in turn is a function of thermal history. The composition of crystal products does not correspond to the composition of the starting oxide mixture: cobalt enriched in the crystals. A tentative explanation of this behavior is suggested by considering possible ionic potential as well crystal field stabilization effects.

GL

Growth strategy for controlling dislocation densities and crystal morphologies of single crystal diamond by using pyramidal-shape substrates. A. Tallaire, J. Achard, O. Brinza, V Mille, M Naamoun, F Silva, and A. Gicquel, *Diamond and Related Materials*, Vol. 33, pp. 71–77, http://dx.doi.org/10.1016/j.diamond.2013.01.006

A single synthetic diamond crystal can be used as an electronic device because of its properties, such as a high breakdown field and thermal conductivity. However, defects, such as dislocation bundles, which were formed during growth process, can cause current leakage, higher bandgap, and birefringence. Defect-free single diamond crystal that is large enough to be used as an electronic device is difficult to grow using current methods. For example, the "threading dislocations" can be formed in a CVD diamond using (001)-oriented substrate. The authors demonstrated that these defects could be reduced by modifying substrate's shape and orientations.

Two type Ib HPHT-grown, pyramidal substrates, type A and type B, were used to grow single CVD crystals in this research. The {100} directions in type A substrate and {110} directions in type B were polished into inclined faces with 20°, 30°, and 40° angles. Both possessed a square top measuring 200 x 200 μm^2. Crystals were grown on these substrates using plasma-assisted CVD technique with power density of 100 W/cm^3 and methane concentration of 5% at 850°C, achieving a growth rate of 13 microns per hour.

After removal of the substrate, the fully grown CVD crystals showed high transparency. Nitrogen-related defects were not detected. The inclined faces in type A substrate helped prevent twin sectors from reaching the top face. The growth rates of the lateral and top faces were 32.5 and 13.5 μm per hour, respectively. When thickness reached about 490 microns, the inclined faces started to disappear. The dislocations, originating from

the square top of a pyramidal substrate, were observed in a crystal grown on type A substrate with 20° dislocations. However, these dislocations were diverted toward the edges rather than the top. Photoluminescence image showed that the inclined faces effectively diverted the direction of threading dislocations from {100} to {110} direction. Absence of sharp edges in these pyramidal substrates also helped in reducing dislocations. The lateral surfaces had the highest growth rate and possessed "fish scale" morphology in type A grown crystals, a morphology not observed in type B crystals. A maximum thickness of 2.2 mm could be achieved with a dislocation of 40° on type B substrate. A crystal 1.70 mm thick containing very low defects was achieved using type B substrate with 20° or 30° dislocations.

KSM

Zircon et geikielite artificiellement étoilés du Sri Lanka [Zircon and geikielite from Sri Lanka with artificial stars]. J.-P. Gauthier, B. Rondeau, and T. Prada, *Revue de l'Association Française de Gemmologie*, No. 180, 2012, pp. 5–11 [in French].

Two asteriated cabochons acquired in Sri Lanka were identified as natural zircon and geikielite. But the six-rayed star had not been observed in natural star zircons, and the eleven-rayed star of the geikielite was crystallographically "impossible." Microscopic observation clearly showed both had been created by a fine scratching of the cabochon domes.

In both cases, the surfaces appeared to have been produced by short parallel scratches. The center of each star was a white spot, and their branches were short, sometimes missing or undulating and hatched. The effect is formed mainly by diffraction at the scratches rather than reflection from needles or hollow tubes, like in natural stones. When the focus of the microscope is lowered some millimeters from above the cabochon surface through below the surface, the star gets finer and is sharpest *below* the surface, in contrast to natural stars, where the sharpest star seems to hover *above* the surface.

The features described above, along with some other characteristics mentioned by Steinbach (2011), allow a safe distinction of scratched star stones from their natural counterparts mostly by simple observation with the naked eye.

RT